A Study of Optical and Electronic Properties of a Semiconducting Polymer, Poly(*o*-methoxyaniline)

Roshan Prasad Shrestha

A dissertation submitted to the faculty of the University of North Carolina at Chapel Hill in partial fulfillment of the requirements for the degree of Doctor of Philosophy in the Department of Chemistry.

Chapel Hill
2006

Approved by:

Advisor: Professor Eugene Irene

Reader: Professor Nalin Parikh

Reader: Professor Edward Samulski

Professor Sergei Sheiko

Professor John Papanikolas

ABSTRACT

Roshan Prasad Shrestha

A Study of Optical and Electronic Properties of a Semiconducting Polymer, Poly(*o*-methoxyaniline)

(Under the direction of Professor Eugene A. Irene)

The optical properties of spin coated thin films of poly(o-methoxyaniline) (POMA) were investigated using spectroscopic ellipsometry (SE) complimented by optical absorption spectroscopy in the visible–near UV optical range and atomic force microscopy (AFM) for surface roughness. For these studies a custom built ellipsometer was constructed and interfaced with a computer and software was written in LABVIEW™ for automation.

A Gaussian oscillator optical model was used to fit the data obtained from SE. roughness results were also evaluated in an optical model. The effect of different spin deposit conditions including spin rate, and concentration of solution and deposition ambient on the POMA film thickness, surface roughness, optical properties and optical anisotropy have been investigated. Small uniaxial anisotropy has been measured and annealing leads to some densification and surface smoothing.

Organic thin film transistors (OTFT) were fabricated with POMA as the active semiconductor layer, silicon dioxide (SiO_2) as the gate dielectric, heavily doped silicon as the substrate, and vacuum evaporated gold lines as the source and drain contacts. The electronic

properties were characterized using a custom built probe station. The custom probe station was also automated with software program written in LabVIEW™.

POMA yielded a P-channel device, and from transfer characteristic and turn-on plot, the charge mobility was calculated which was in the range of about 10^{-3} cm^2 V^{-1} s^{-1}. Various post fabrication processes were carried out to optimize the device performance. Controlled doping and moderate annealing have shown improvement in the device mobility by 10 folds and 2 folds respectively, yielding evidence for a hopping mechanism for charge transport in POMA. Two alternate gate dielectric layers for the OTFT were also considered; while a non-polar low-K dielectric, polyethylene improved mobility; polar high-K dielectric, copolymer of vinylidene fluoride with trifluoroethylene had an adverse effect on mobility.

ACKNOWLEDGEMENTS

I am eternally grateful to Dr. Eugene Irene for his support, patience, encouragement and insight, which has helped shape the research and my research skills. His valuable feedback contributed greatly to this dissertation. Without him, this dissertation would not have been possible.

I would also like to thank my Student Advisory Committee members, Professor Edward Samulski, Professor Nalin Parikh, Dr. Sergei Sheyko, Dr. Mark Schoenfisch and Dr. John Papanikolas who deserve credit or their support and their valuable feedback helped me to improve my dissertation in many different ways.

Professor Sean Washburn, Professor James Jorgenson, and Professor Gary Glish have helped me in various aspects during my years in Graduate School.

Past members our research lab, Dr. Ciro Lopez, Dr. Natalya Suvorova, Dr. Alex Mueller, Dr. Jason Brewer, and present members, Dr. Li Yan, Mrs. Yuxiang Li, and Dongxing Yang have been helpful and knowledgeable mentors, colleagues, and friends. I am also thankful to them.

Collin J McKinney, John Peterson, and the Electronics Support staff in Chemistry Department deserve due credit for assistance with the circuit boards and electronics.

Faculty members at Grinnell College, Grinnell, IA, Budhanilkantha High School, Nepal and St. Xavier's School also deserve due credit.

My host family in Grinnell, Iowa has have given me a home away from home. I am thankful to the Hoskins.

Archana Goyal for her love, support, and patience.

My family has made great sacrifices for my education. I am grateful to my parents Dr. Ravi Prasad Shrestha, Sangeeta Shrestha and my beloved sister Rashmi Shrestha for their blessings and love.

TABLE OF CONTENTS

LIST OF TABLES

LIST OF FIGURES

LIST OF ABBREVIATIONS AND SYMBOLS

#	number
%	percent
<ε>	pseudo dielectric constant
°	degree
A	analyzer
•	angstrom
A/D	analog to digital
AFM	atomic force microscopy
A_{off}	analyzer offset
B	Magnetic field vector
C	capacitance
c	velocity of light in vacuum
cm	centimeter
Δ	Delta (ellipsometric measureable)
D	coefficient of parabolic equation
DC	direct current
ε	epsilon dielectric function
E	electric field vector
Em	electromagnetic wave

E_p,	electric field vector in parallel direction
E_s	electric field perpendicular (s from German word, *senkrecht*, meaning normal to POI)
EtOH	ethanol
eV	electron volt
ϕ	angle of incidence
g	gram
η	phase constant (correction) during alignment
hr	hour
IR	infrared
K	dielectric constant, Kelvin
k	extinction coefficient
$k_{\perp}$	extinction coefficient perpendicular
$k_{\parallel}$	extinction coefficient parallel
k_b	boltzmann's constant
Kg	kilogram
λ	wavelength
L	film thickness
LED	light emitting diode
m	Meter
M	molar
MEK	methyl ethyl ketone
MeOH	methanol

min	minute
mL	milliliter
mm	millimeter
mol	mole
MSE	mean squared error
MW	molecular weight
n	refractive index
N	Negative nitrogen
$\tilde{N}$	complex refractive coefficient
$n_{\perp}$,	refractive index perpendicular
$n_{\parallel}$,	refractive index parallel
n_e	refractive index extraordinary ray
nm	nanometer
n_o	refractive index ordinary ray
^oC	degrees Celsius
P	polarizer, positive
PMT	photomultiplier tube
P_{off}	Polarizer offset
POI	plane of incidence
R	Resistance, Fresnel coefficient
R.T.	room temperature
s	second

SE	spectroscopic ellipsometry
T	temperature
TTL	Transistor-Transistor Logic
aUV	ultraviolet
v	velocity
W	watts
wt	weight
wt%	weight percent
Ψ	psi (ellipsometric measureable)
•	Alpha (Fourier Coefficient)
•	Beta (Fourier Coefficient)
•	mobility
• m	micrometer
•	arbitrary phase constant
•	ohm

CHAPTER 1 - INTRODUCTION

1.1. Overview

In the last 5 decades inorganic silicon based semiconductors have been the backbone of the electronic industry.[1-3] However there has been growing interest in improving the semiconducting and light emitting properties of organic materials through various syntheses of polymers and hybrids (organic-inorganic). The ease of fabrication of organic devices bypassing multimillion-dollar clean rooms, and the ability to process large active areas at low temperatures, and over larger areas has been the driving force for research in organic materials.[4, 5] In addition the mechanical flexibility of organic semiconductors makes them more compatible for use with plastic substrates for lightweight and foldable applications.[6, 7]

Organic semiconductor based devices such as organic thin film transistors (OTFT) will not be suitable for use in applications requiring high switching speeds as in logic processing because of their relatively low charge mobility and therefore the limit to upper-end switching speeds.[2, 4] As a reference, the current thin film transistors based on crystalline Si (MOSFET) has 3 orders of magnitude higher carrier mobilities than OTFT. However, the OTFT has niches in novel thin film transistor applications requiring structural flexibility, low temperature processing, large area coverage, and lower cost e.g. sensors, low-end smart

cards, and radio-frequency identification tags (RFIDs). Since the report of the first OTFT fabrication in 1986, there has been significant improvement in the material performance as well as fabricating designs and technologies.[4] Many of the applications of OTFT are already in the market, and the global market for organic electronics is set to expand from $650 million in 2005 to $30 billion by 2015, according to a recent report from IDTechEx.

1.2. Thin Film Transistors

Before the introduction of the OTFT, an introduction of an inorganic FET is presented for comparison. The MOSFET—metal oxide semiconductor field effect transistor—is the building block of microelectronics where the source to drain conduction is controlled by the gate potential. After it was initially fabricated in 1950's, research has led to significant decrease in MOSFET size and increase in its performance and complexity. An N-channel MOSFET is shown in Figure 1.1.

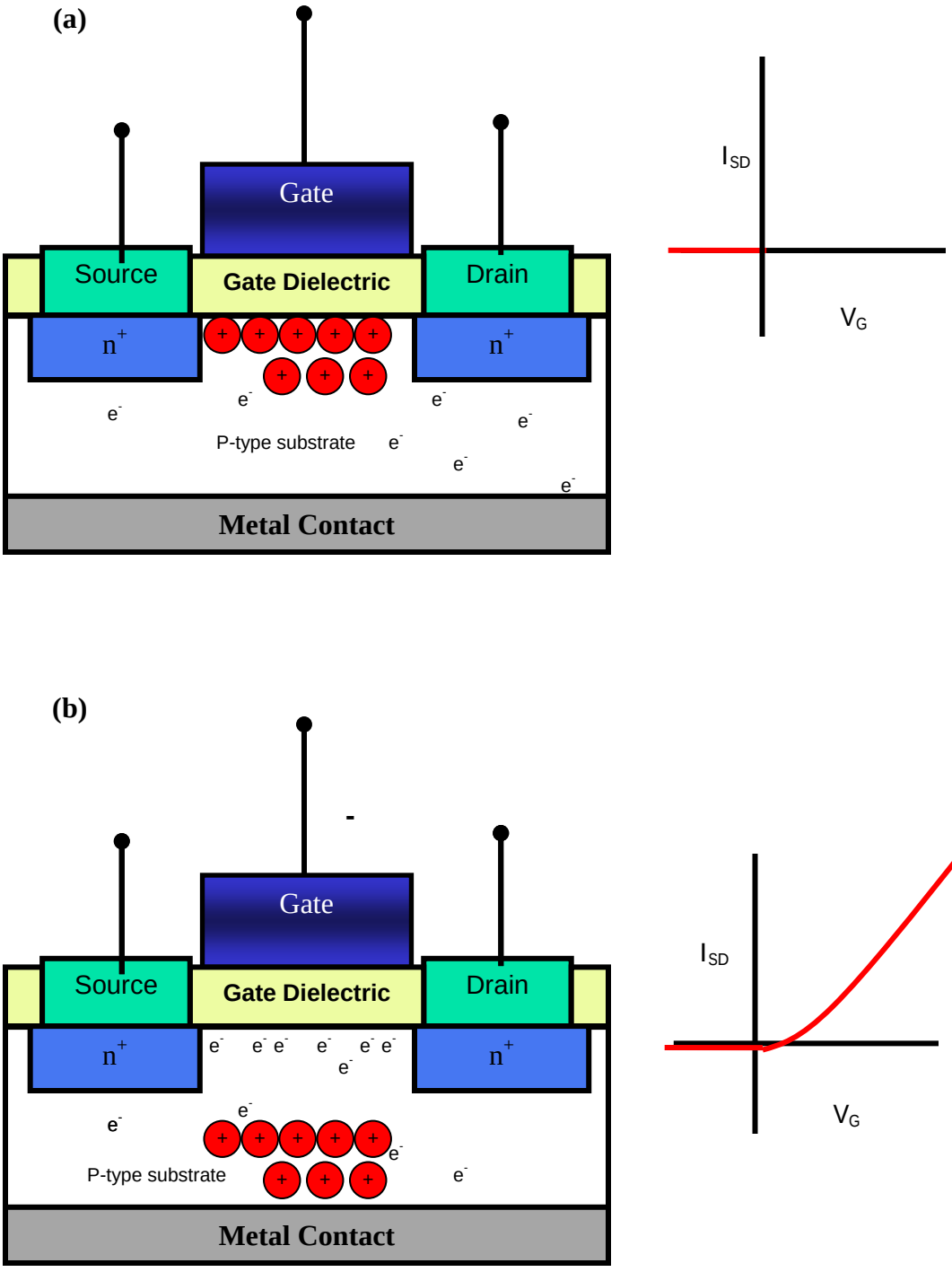

Figure 1.1 (a) N-Channel MOSFET in Accumulation mode. (b) Inversion mode.

The source and the drain are two highly conducting N-type semiconducting regions in a P-type Si substrate. The voltage applied to the gate controls the flow of electrons from the source to the drain. When a negative voltage is applied to the gate, the electric field attracts the majority holes to the interface of the substrate and the gate oxide. During this accumulation of the majority carriers (holes) at the interface, the current does not flow between N-type source and drain as the positive and negative charges neutralize each other to form an insulating depletion layer around the doped regions. The I_{SD} curve in the adjacent turn on characteristic plot remains flat.

As the gate voltage is changed from negative to positive, the holes are repelled from the interface, and the minority carriers, electrons are drawn to the interface of the substrate and the gate oxide as shown in Figure 1.1b. These electrons form a conducting N-channel between the source and drain called an inversion layer, which facilitates conduction. The I_{SD} in the turn-on characteristics plot increases sharply after the threshold voltage. When the channel is conducting it is called the 'on' state and when the channel is depleted, it is called the 'off' state. Thus a transistor can be used for logic processing. Each transistor in a microprocessor can be referred to as a bit. A set of 4 transistors can form a byte and used for memory storage or logic processing. These 'on' and 'off' states can form the binary 0 and 1 code structures.

OTFT's are only similar to a MOSFET in basic design as it is also composed of three terminals—a gate, a source, and a drain. Figure 1.2 shows a typical OTFT. Here the heavily doped silicon wafer is only used as a convenient conductive substrate and is not part of the active layer. In addition, the gate oxide lies below the semiconductor layer in the OTFT.

This structure is appropriately called the “inverted gate” structure. Another difference between an OTFT and a MOSFET is that the majority carriers facilitate conduction in an OTFT i.e. it operates in the accumulation mode instead, and the inversion mode does not exist. Therefore, for a P-channel OTFT, a negative voltage bias is required at the gate to accumulate majority carriers at the interface of the SiO_2 dielectric layer and the semiconductor layer.

In order to fabricate an OTFT, highly doped Si used as the gate contact is thermally oxidized to prepare the SiO_2 gate dielectric layer. Au is deposited in either an interdigited Au array or in parallel lines using a shadow mask. The organic film is then deposited by spin casting from solution.

For an OTFT to function properly, a conducting molecule in the active layer must have delocalized charge within the molecule. Delocalization of charge is possible in molecules with conjugated double bonds where the molecular backbone of the polymer has the carbon atoms with alternating single and double bonds. Each bond contains a localized sigma bond, and the double bonds consist of a pi and a sigma bonds. Intermolecular alignment facilitates delocalization of charge between the molecules via π–π bonds overlap. Several mechanisms of charge transfer are reported in the literature, such as hopping and band transport, which will be discussed in Chapter 2.

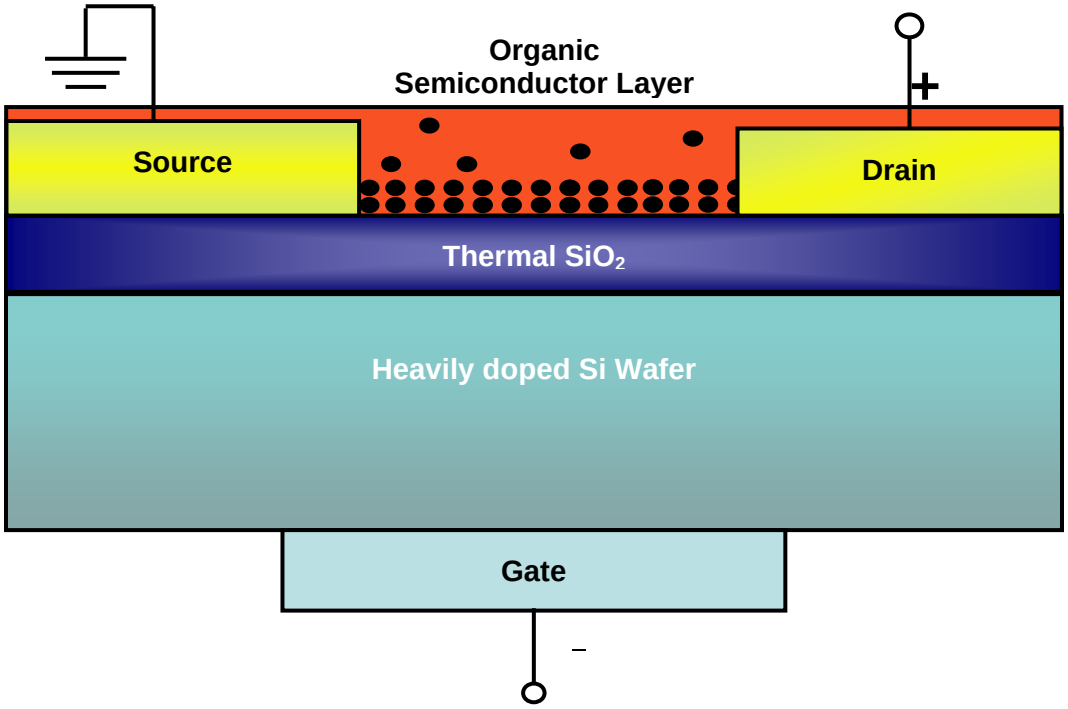

Figure 1.2. Organic thin film transistor in an inverted gate structure.

1.3. Motivation

A strong polymer candidate for use in OTFT is poly(*o*-methoxyaniline) (POMA) shown in Figure 1.3. It has sparked research curiosity because of its environmental stability, and the ease with which its electrical properties can be controlled.[8-10] Doping the polymer can change its conductivity from a poor semiconductor ($\sigma \sim 10^{-10}$ S cm^{-1}) to a metal (σ 10^{-1} to 10^{-2} S cm^{-1}) and it is stable in both doped and undoped forms.[11] Additionally, POMA demonstrates higher solubility in various solvents than its parent, polyaniline and it is easily polymerized from a low cost monomer, as well as purified. These properties enable POMA to be a suitable candidate for the fabrication of an OTFT.

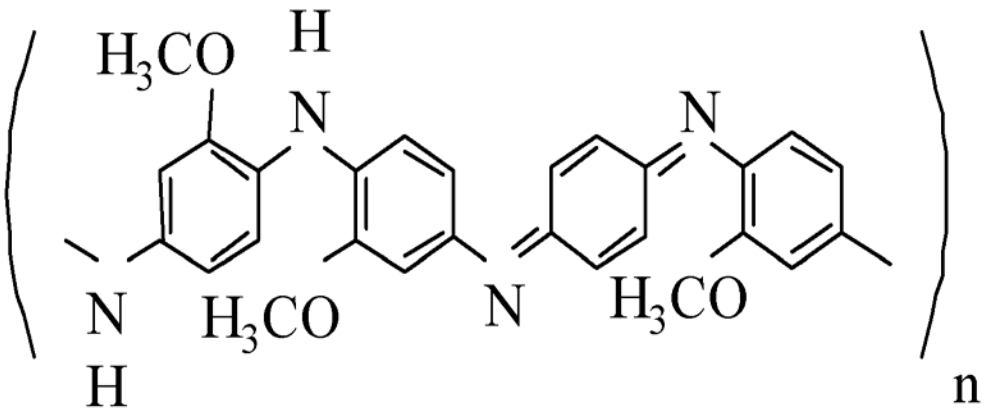

Figure 1.3. The molecular structure of POMA.

From the descriptions of OTFT and the MOSFET in Section 1.2, it is clear that both devices operate based on controlled conduction of charge carriers at an interface of the active and the dielectric layers. Thus the interface is a vital region since it determines the performance of the device. It is important to understand the optical film properties of POMA and POMA film-substrate interface properties. Once the optical properties are obtained, film thickness can be extracted using non-destructive techniques which will also aid fabrication process. Understanding the electronic properties is will provide necessary information relative to the use of POMA in an OTFT.

1.4. Research Objectives and Strategy

There have only been a handful of fundamental research studies that have started with a film preparation study and a determination of the optical properties of the thin organic films and then proceeded to electronic and devices properties and properties optimization. In this kind of study a more complete understanding of the relationships between materials and electronic properties can be obtained. Therefore, the main objective of this research is to establish and understand the optical and electronic properties of the POMA film for use in OTFT. In order to achieve this objective, thin films of POMA were prepared from solution using the spin casting technique. The solubility of POMA in various solvents (polar, non-polar, and protic-polar), and the resulting nature of POMA films was also examined.

Once the optical properties of POMA, its morphology along with the chemical and physical information about the polymer film were determined, in the second stage, OTFT's based on POMA were fabricated to test the electronic properties. The performance of an OTFT is gauged by several measures—mainly the electronic mobility and turn-on/turn-off

ratio. The electronic mobility, μ describes how easily charge carriers can move within the active layer under the influence of the electric field, and turn-on/turn-off ratio is indicative of the switching performance of OTFT. The performance of the fabricated OTFT will be assed with these gauges.

In the final phase of this research, once an understanding between the interface and the opto-electronic properties is developed, improvements or modification of OTFT devices was investigated in order to optimize device performance. When exploring an organic substitute for SiO_2 gate dielectric, high capacitance dielectric is normally desirable, as it reduces the operating voltage required to turn the device on.[3, 12] However, it has also been reported that the polarity of the dielectric interface can affect the local morphology of the POMA film and the distribution of electronic states in it. Veres *et al.* have reported improvement in device performance with the use of non-polar low-K gate.[13] In order to resolve this controversy about the choice of low-K or high-K dielectric for use as gate material in OTFT, polyethylene (K = 2.3), and a copolymer of polyvinyledene fluoride copolymer (PVDF-TrFE) (K = 2.3) will be investigated. These measures will be described in detail in the following chapters.

1.5. Dissertation Overview

This dissertation consists of three main sections. Section 1 deals with the principles and techniques used, and is described in Chapters 2 and 3. Chapter 2 describes the mechanism of charge transport in a polymer film and the measures used to gauge the electrical properties of OTFT mentioned above. During this study, a probe station was also

assembled and automated for efficient electronic measurements. The probe manipulators were bought from Signatone and the vacuum enabled chuck which act as the base and the wafer holder as well as the gate voltage supply node was designed and fabricated in our research laboratory. The software program to automate and streamline the measurement process was complied in LabVIEW™. The strategy used for electronic measurements is discussed in also presented in Chapter 2.

Chapter 3 introduces ellipsometry, the technique used extensively during the study. An *in-situ* rotating analyzer ellipsometer was constructed and interfaced with a computer for automation. Ellipsometry theory and instrumentation, and the application of the commercial computer program LabVIEW™ are discussed in Chapter 3.

In the second section of this dissertation, which comprises Chapters 4 and 5, the main results and discussions generated from this research are presented. The contents of these chapters have been submitted for publication in peer reviewed journals. In Chapter 4, the process used to extract the optical properties of spin-cast POMA films is discussed in detail. A model WS-400B-6NPP-LITE instrument from Laurell Technologies Corporation was used to spin coat various thicknesses of POMA films on Si and SiO_2 substrates by varying spin speeds and solvent viscosity. The custom ellipsometer was the primary instrument used in this study. Complimentary information necessary to build a more comprehensive optical model were also obtained from UV-Vis Spectroscopy, and Atomic Force Microscopy (AFM).

The OTFT's were fabricated using Si wafers as the substrate, SiO_2 gate dielectric, gold evaporated lines for source and drain contacts, and POMA films for active

semiconductor layer. The electronic properties mainly the transfer and turn on characteristics were obtained using the custom built probe station. The POMA TFT demonstrated characteristics of a P-channel device, and its positive charge carrier (hole) mobility was calculated in the order of 10^{-3} $cm^2V^{-1}s^{-1}$. In order to optimize the device performance, doping and annealing experiments were carried out. An additional buffer layer made from a low-K non-polar polyethylene films and polar high-K polyvinyledene fluoride copolymer (PVDF-TrFE) were also investigated. These electrical characteristics and improved mobility are discussed in Chapter 5.

Chapter 6, "Summary and Future Directions," makes up the final section of the dissertation.

1.6. References

1. Kumar, D.; Sharma, R. C., Advances in conductive polymers. *European Polymer Journal* 1998, 34, (8), 1053-1060.

2. Horowitz, G., Organic field-effect transistors. *Advanced Materials* 1998, 10, (5), 365-377.

3. Dimitrakopoulos, C. D.; Malenfant, P. R. L., Organic thin film transistors for large area electronics. *Advanced Materials* 2002, 14, (2), 99-+.

4. Dimitrakopoulos, C. D.; Mascaro, D. J., Organic thin-film transistors: A review of recent advances. *Ibm Journal Of Research And Development* 2001, 45, (1), 11-27.

5. Sweatman, D., Organic Device: A Review. *MICROELECTRONIC ENGINEERING RESEARCH CONFERENCE 2001* 2001.

6. Pettersson, L. A. A.; Ghosh, S.; Inganas, O., Optical anisotropy in thin films of poly(3,4-ethylenedioxythiophene)-poly(4-styrenesulfonate). *Organic Electronics* 2002, 3, (3-4), 143-148.

7. Mushrush, M. A. P-type and N-type oligothiophene-based semiconductors as active layers in organic field-effect transistors. Ph.D., Northwestern University, United States -- Illinois, 2003.

8. Viva, F. A.; Andrade, E. M.; Molina, F. V.; Florit, M. I., Electropolymerization of 2-methoxy aniline. Electrochemical and spectroscopical product characterization. *Journal of Electroanalytical Chemistry* 1999, 471, (2), 180-189.

9. Bianchi, R. F.; Onmori, R. K.; Goncalves, D.; de Andrade, A. M.; Faria, R. M.; Irene, E. A., An electrical study of a thin film poly(o-methoxyaniline) field effect transitor. *Synthetic Metals* 2001, 121, (1-3), 1687-1688.

10. Bianchi, R. F.; Ferreira, G. F. L.; Lepienski, C. M.; Faria, R. M., Alternating electrical conductivity of polyaniline. *Journal Of Chemical Physics* 1999, 110, (9), 4602-4607.

11. Onmori, R. K.; Olivati, C. A.; Bianchi, R. F.; Faria, R. M.; de Andrade, A. M., Study of a POMA based solar cell. *Synthetic Metals* 2001, 121, (1-3), 1577-1578.

12. Chua, L. L.; Zaumseil, J.; Chang, J. F.; Ou, E. C. W.; Ho, P. K. H.; Sirringhaus, H.; Friend, R. H., General observation of n-type field-effect behaviour in organic semiconductors. *Nature* 2005, 434, (7030), 194-199.

13. J. Veres; Ogier, S. D.; Leeming, S. W.; Cupertino, D. C.; Khaffaf, S. M., Low-k Insulators as the Choice of Dielectrics in Organic Field-Effect Transistors. *Advanced Functional Materials* 2003, 13, (3), 199-204.

CHAPTER 2 – ORGANIC SEMICONDUCTORS and ELECTRONIC MEASUREMENTS

2.1. Overview

The active component in the OTFT is the organic semiconductor layer as shown in Figure 1.2. Organic semiconductors are typically materials consisting of primarily carbon and hydrogen. They can be small monomeric molecules such as pentacene and anthracene, or large macromolecules such as polyacetylene or poly(o-methoxyanline). Likewise, organic semiconductors can be categorized into classes of amorphous, crystalline, or a combination of both depending on their molecular structure, electronic structure, and the conditions under which the films are prepared. Schematic diagrams for different classes of organic semiconductors are depicted in Figure 2.1. As briefly mentioned in Chapter 1, OTFT's cannot replace Si based FET's due to their lower switching speeds, but they have the advantages over inorganic FET's of low cost processing, large surface area, and flexibility.

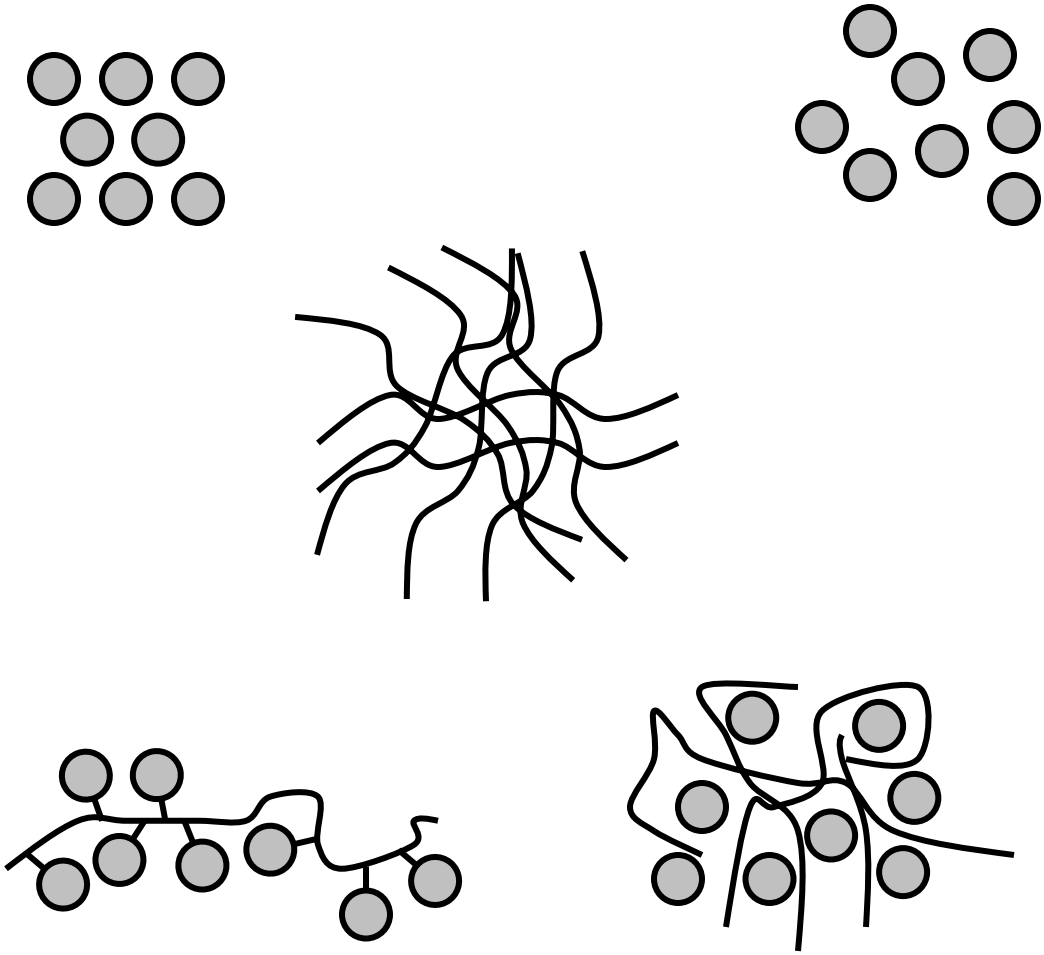

Figure 2.1. Schematic diagram depicting different classes of organic semiconducting materials. (a) molecular crystalline e.g. pentacene at low temperature (b) molecular amorphous (e.g. NDA-N2) [2] (c) p conjugated polymer chain e.g POMA (d) polymer with pendant active group PVK polyvinyl carbazole (e) molecularly doped polymer (POMA doped with cresol of HCl).

In this Chapter, the molecular structure and formation of electronic states in the carbon based semiconductor will be discussed. The concepts of resonance and conjugation in delocalization of charge and charge transport will be highlighted. Measuring the performance of OTFT's is crucial to understand the feasibility for the use of a particular organic semiconductor in an OTFT. Therefore, parameters such as mobility, "on/off" ratio, and leakage currents will be presented along with several theories on charge transport in organic semiconductors. A simple OTFT schematic has been introduced in Chapter 1. Here, two different popular OTFT designs—namely the top and bottom contact designs—will be discussed along with their fabrication and performance pros and cons. The electronic measurements were carried out using a custom built probe station. Therefore, the instrumentation will also be briefly introduced.

2.2. Organic Semiconductors

A few of the well known organic semiconductors are polyaniline, pentance, butadiene, polythiophene, and polyacetylene, whose molecular structures are illustrated in Figure 2.2. Examining the structures of these organic semiconductors, it is clear that they have some features in common. One relevant feature is that the carbons are sp^2 hybridized and they have conjugated double bonds. These alternating double bonds involve delocalized π electrons in p-orbitals and therefore permit charge delocalization within the molecule. In organic chemistry the delocalization of charge is indicated by resonance structures.

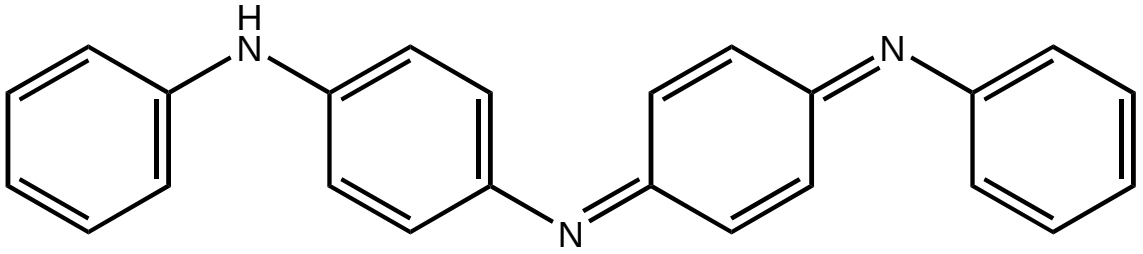

polyaniline

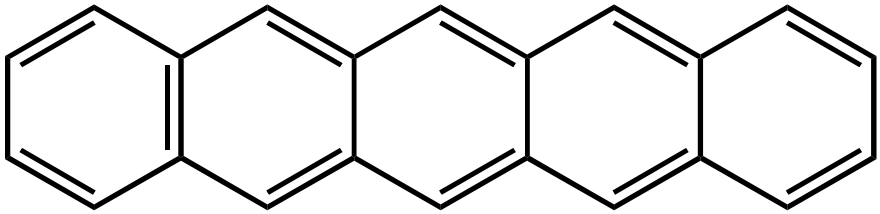

pentacene

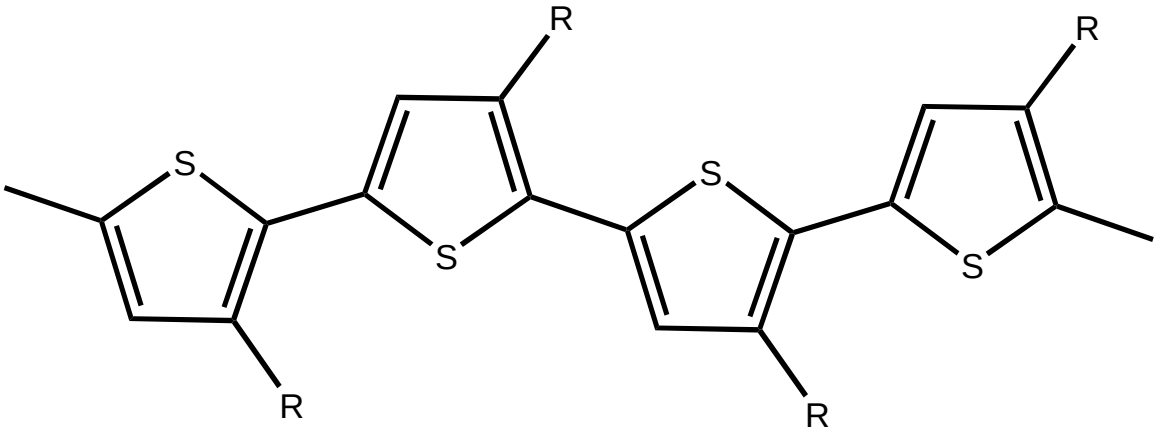

polythiophene

polyacetylene

Figure 2.2. Examples of well-known semi conducting polymers.

The resonance effect results in more stable molecules and is exemplified by comparing the hydrogenation of cyclohexene and benzene to form cyclohexane. Both molecules are cyclic six-membered carbon chains; cyclohexene has one double bond, while benzene has three double bonds. The hydrogenation of a cyclohexene releases 120 KJ/mol of energy. Extrapolating this evidence, benzene, which has 3 double bonds, should release 360 KJ/mol (Fig. 2.3). However, experimental results indicate only 232 KJ/mol of energy being released during the hydrogenation of benzene. These findings indicate benzene is more stable than cyclohexene as depicted in Figure 2.3. In an isolated double bond, as in cyclohexene, any charge formed is concentrated on a single carbon, which makes it unstable and increases its energy level. On the other hand, when the charge is delocalized and several carbon atoms share the discomfort, the total energy required for storing charge in the molecule is reduced. Charge delocalization by resonance in a benzene ring is depicted in Figure 2.4. This phenomenon allows the molecule to remain stable with a charge on it during charge transport from one chain to another.

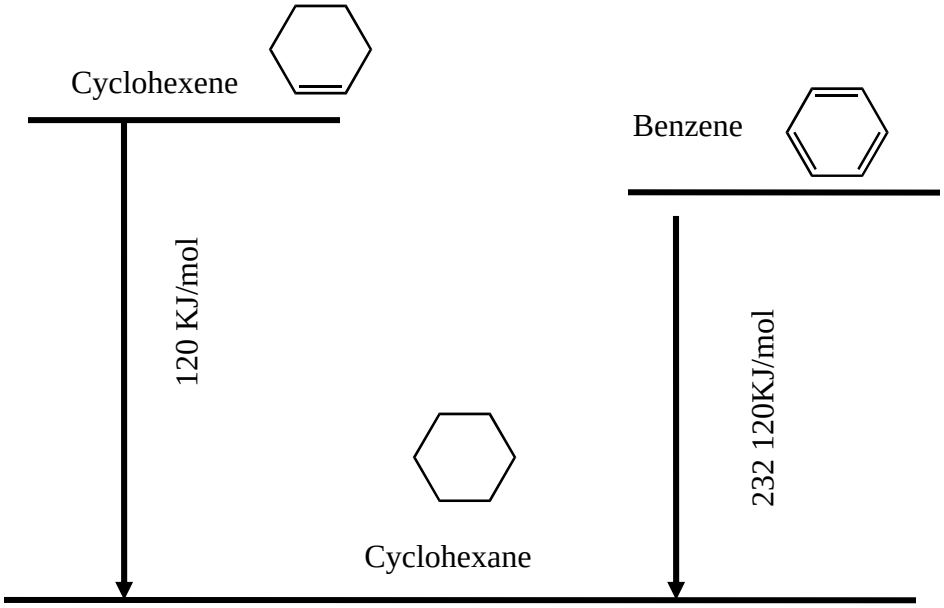

Figure 2.3. Energy release during the hydrogenation of cyclohexene and benzene suggest thermodynamic stability of benzene as a result of resonance.

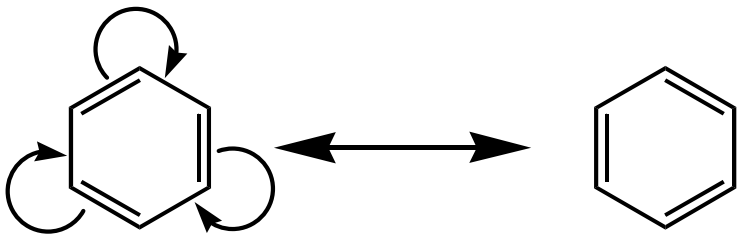

Figure 2.4. Resonance structures of benzene molecule.

2.3. Charge Transport Mechanisms in Organic Semiconductors

The charge-transport in OTFT's depends primarily on the degree of ordering of the polymer or oligomer molecules in the solid state, and the density of defects that are present in the lattice. As a benchmark, the Si lattice is held firmly together with covalent bonds with 320 KJ/mol energy.[3] The charge carriers are reported to move with ease in Bloch waves in its highly delocalized planes and wide bands. Therefore, charge mobilities as high as 10^3 $cm^2 V^{-1} s^{-1}$ is observed for Si.

The charge mobility observed for some organic crystals such as pentacene also relatively close to that of Si in the range of 10 $cm^2 V^{-1}s^{-1}$ but at ~ 17 K or lower. This high mobility suggests that the transport mechanism is similar to that of inorganic semiconductors take place in organic semiconductors takes place at low temperature.[4-6] In organic semiconductors, the highest occupied molecular orbital (HOMO) and the lowest unoccupied molecular orbital (LUMO) split from the interaction of the adjacent semiconductor chains to form bands as shown in Figure 2.5. One of the key parameters for charge transport in organic conjugated materials is the ease with which this inter-chain charge transfer takes place; the ease of which depends upon the band width and shape—with wider bands affording greater charge transport.

With an increase in temperature, the effective band widths are progressively reduced by lattice vibration and strong phonon-charge carrier coupling.[7, 8] The van der Waals force, the most significant intermolecular interaction in organic films at room temperature, only approaches 40 KJ/mol whereas the lattice vibration can be higher than 50 KJ/mol, which prevents molecular chain alignment and prevent long range lattice formation.[3, 9] Therefore,

the band like charge transport becomes progressively uncommon as the temperature rises and the charge delocalization is often restricted to single units.[5, 10]

Unlike the few examples of single crystals at low temperature, most organics are amorphous, at best they are polycrystalline. The impurities and ample grain boundaries present in amorphous solid effectively reduces the charge mobility to 10^{-4} to 10^{-2} range as the charges are trapped and scattered. Therefore, alternative charge transport mechanisms for organic semiconductors are necessary and are presented in the literature. The three most relevant ones are discussed here; they are band transport, hopping mechanism, and multiple trapping sites and release models.

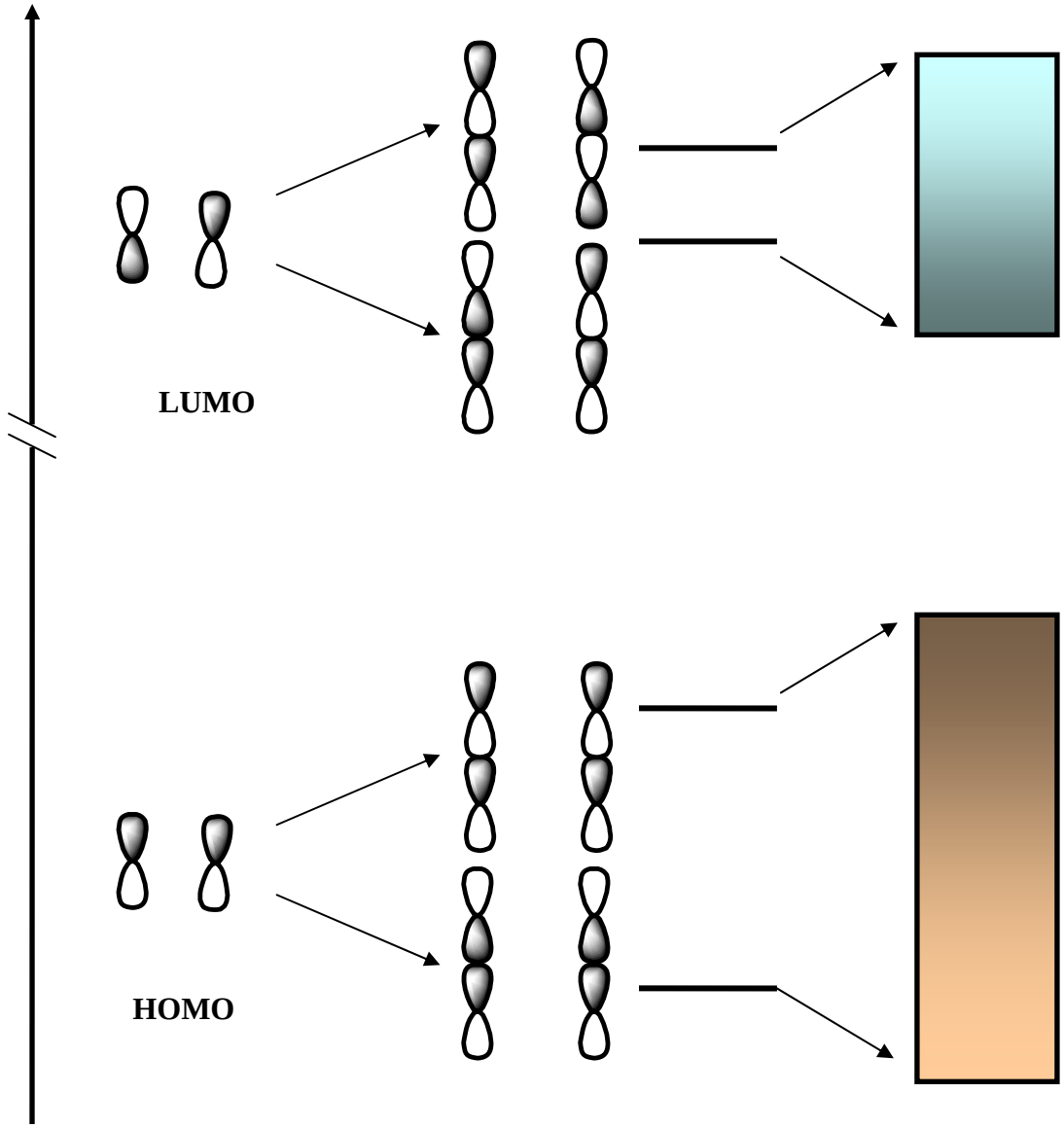

Figure 2.5. Illustration of bonding and anti-bonding orbital interaction of HOMO and LUMO orbitals of a segment of polyethylene molecule; Cumulative interaction of these orbitals form bands at very low temperature analogous to the valence and conduction bands.

2.3.1. Band Transport

The band transport mechanism is a well known charge transport mechanism in inorganic semiconductors. A regularly spaced tightly bound lattice forms a band structure where the charge carriers are delocalized over a large area with little hindrance.[11] Highly ordered structures have been observed in some organic semiconductors, albeit at very low temperatures. Room temperature mobility of ~ 1 $cm^2 V^{-1} s^{-1}$ has been reported for pentacene, which increases considerably to values as high as 10^2 $cm^2 V^{-1} s^{-1}$ at 1.7 K. This power law dependence of mobility on temperature ($\mu \propto T^{-n}$) and the observation of a Quantum Hall Effect presents a good argument that structured organic materials at low temperature can demonstrate band like conduction.[5]

Figure 2.6 shows a schematic diagram of delocalized band transport. When the charge carriers comes in contact with a defect, or a lattice vibration as shown in part b and c, they scatter, thus reducing the charges moving in forward direction. There are less molecular vibrations at lower temperature, and therefore, the scattering of charge carriers are low. Consequently, the carrier mobility, μ shows dependence on temperature ($\mu \propto T^{-n}$). At room temperature, band transport is difficult because of increased molecular lattice vibration which causes the charge carriers to scatter significantly.

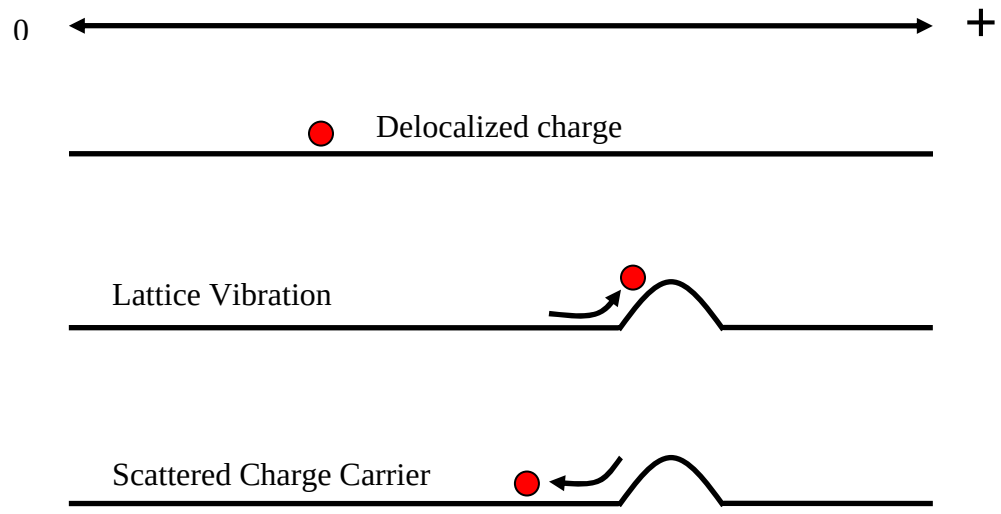

Figure 2.6. Delocalized charge in a crystal lattice, and charge scattering due to lattice vibration.

2.3.2. Hopping Transport

In most amorphous organic films, the charge carriers are strongly localized in "potential wells." In these materials, the "hopping" of charges between these potential wells has been reported as a main mechanism of charge transport.[12-14] In organic semiconductors, the transport mechanism can be described in terms of sequential jumps of the relaxed charges between adjacent chains. The mechanism has also been referred to as the "thermally activated polaronic hopping processes."

The sources of these "traps" can be extrinsic or intrinsic.[15, 16] The grain boundaries, packing imperfections, impurities in lattice and interfacial states are considered extrinsic causes of localization. Intrinsic cause arises from polarons, which are formed when a moving charge polarizes the lattice around it. The resulting lattice polarization acts as a localization site and hinders the movement of the charge, thus decreasing the charge mobility.[7]

Figure 2.7 shows a diagram of various trapping sites in an organic semiconductor. The molecular vibrations in the solid provides energy for the charge carriers indicated by the red dots to hop from one shallow trap site to an adjacent trap site in the direction of the electric field.

Temperature affects the mobility positively by several orders of magnitude because the charge transport is assisted by the lattice vibrations.[6] This process of thermally activated tunneling from an occupied site to an empty was initially described by Mott as phonon assisted hopping.[17]

$$\mu \propto \exp[-(T_0/T)^{1/\alpha}] \tag{2.1}$$

Equation 2.1 was derived by Mott by optimizing the competition between hopping distance and the activation energy required for hopping between the two sites. In Mott's equation α is an integer $1 < \alpha < 4$. When $\alpha = 4$, we observe typical Arrhenius behavior observed in many thermally activated processes suggesting that thermal energy assists the charges to "hop" from between localized sites in the direction of the electric field.

With the increase in temperature, the number of molecules with adequate energy required for activation of the charge carriers to hop increases (the energy distribution curve in the Boltzmann's distribution shifts to the right). Miller and Abraham further developed Mott's ideas, and proposed the following Equation 2.2 with Boltzmann's term for the hopping rate between an occupied site *i* and an adjacent unoccupied site *j*:[18]

$$\nu_{ij} = \nu_0 \exp(-2\gamma R_{ij}) \begin{cases} \exp\left(\dfrac{E_i - E_j}{k_B T}\right) & E_i > E_j \\ 1 & E_i < E_j \end{cases} \tag{2.2}$$

Here υ_0 is the frequency of hopping corrected by the tunneling probability and the probability of absorbing thermal energy. The $E_i - E_j$ is energy difference between the two sites and R_{ij} is the physical separation between the two sites. The wave function overlap between the two sites is γ^{-1} and, and k_B is the Boltzmann's constant. This model addresses hopping mechanism of charge transport between three dimensional shallow impurity states in a compound with weak lattice coupling such as amorphous semiconductors.[19] One of the methods to improve the density of these shallow trap sites is to anneal the organic film which

improves molecular alignment and results in improved mobility. This effect will be presented in Chapter 5 where the optimization of OTFT performance is discussed.

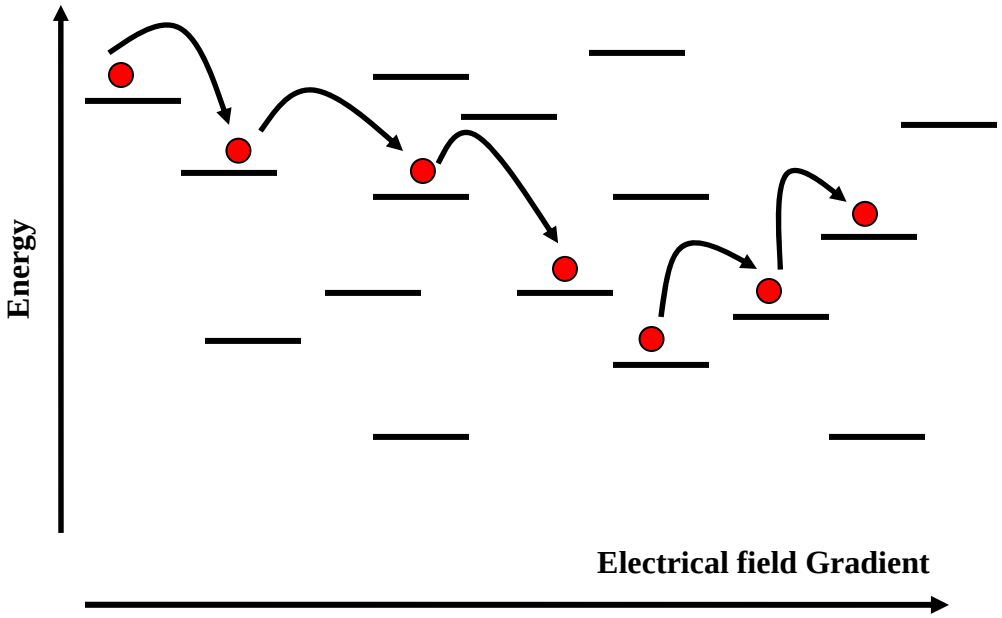

Figure 2.7. Phonon assisted hopping of charges between localized sites.

2.3.3. Multiple Trapping Sites and Release[12]

Multiple Trapping and Release (MTR) model was first described in 1970 by Comber *et at*.[20] It combines elements of the band transport and hopping mechanisms. It also helps to explain the gate voltage dependent effect on mobility. In this model, a narrow delocalized band is available next to a high concentration of reoccurring trap sites as shown in Figure 2.8a. The delocalized bands are formed by the π–π band overlap in the semiconductor.[21] Likewise, the grain boundaries, impurities, and interface states form the traps. As a charge carrier travels, it continuously interacts with these trap sites, and is released to the delocalized band through thermal activation. In this model, the gate voltage dependence mobility arises from direct correlation between mobility and density of occupied localized states in the semiconductor (occupied trapping sites) shown in Equation 2.3.

The schematic diagram in Figure 2.8a illustrates a simple MTR transport mechanism. In this model, when the gate voltage is applied to the OTFT, the charge carriers are accumulated at the interface of the gate dielectric and the semiconductor. As the energy level of the charge carriers are raised, which raises the Fermi level (E_f), the lower energy trap sites of the semiconductor are filled, thereby initially reducing the number of charge carriers. The effective mobility μ_{eff} in the semiconductor is thus related to the ratio of the free carriers to the total charge carrier density and the energy difference between the trap site and the delocalized band edge as described by Equation 2.3.[22]

$$\mu_{eff} = \mu_0 \alpha \exp\left(\frac{-E_a}{kT}\right) \tag{2.3}$$

Here, E_a is the energy difference between the trap level and the delocalized band edge and α is the ratio of the density of charge carriers at the delocalized band to density charge carriers in the trapped states. Two assumptions are made in order to derive Equation 2.3 [22]—the probability of carriers being trapped is close to one, and a temperature provides the energy for the charge release from these sites.

When multiple trapping sites are available as shown in Figure 2.8b, the charge carriers can interact with a wide range of trapping sites. Therefore, the free carrier available then becomes a direct function of V_G, which can also provide the activation energy for the carriers to be released and transported to the delocalized band. With the increase in V_G, as more and more charges start accumulating in the interface, they start occupying trap sites at relatively high energies. These additional charges at higher energy levels will require less activation energy to hop to a neighboring trap sites and into the delocalized area. This mechanism results in a higher mobility with increasing gate voltage and higher temperature.

Comparing the MTR model to the classical model, most of the charge carriers can be viewed as being trapped in the localized states which is equivalent to the valence band. The delocalized state is classically analogous to the conduction band. Therefore, then charge carriers released to the delocalized states would depend upon the temperature, energy of the localized states and the gate voltage.

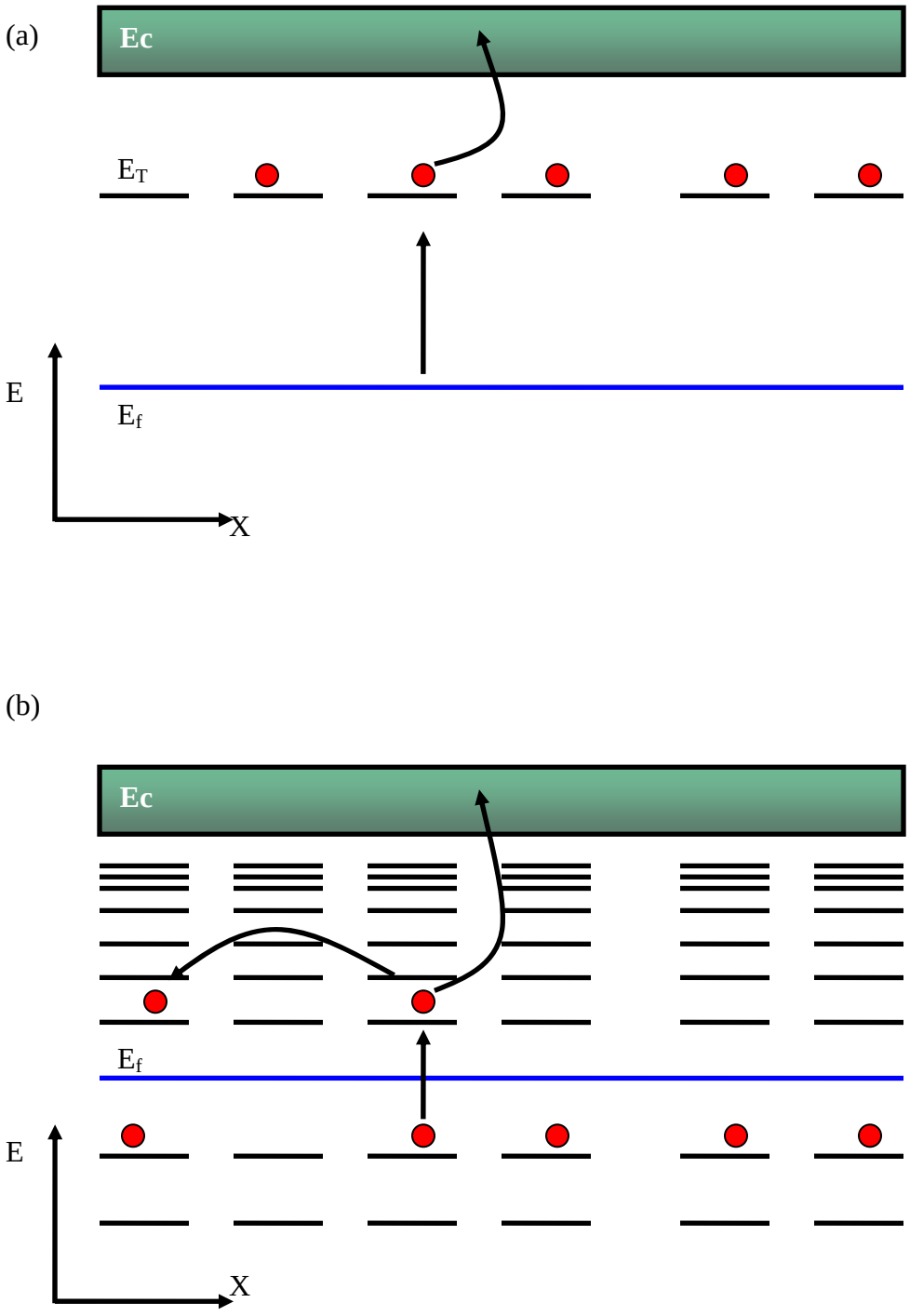

Figure 2.8. (a) Schematic illustration of a single trap level (b) and an availability of multiple traps.

2.4. **OTFT Operation and Effect of Gate Voltage**

The macroscopic view on the operation of a transistor has been discussed in Chapter 1. Here details of observation during the OTFT operation and the molecular contribution in the active layer will be presented. In order to describe some of the concepts of charge movement in OTFT's, it is useful to start by considering a semiconductor stack in a film aligned well with one another. Here the strength of the electronic coupling between the HOMO levels of the adjacent molecules determines the hole mobility in the semiconductor.[23] When gate voltage is applied, electric field alters the Fermi level, E_F of the HOMO, which changes the energy of the charge carriers, and thus affects the inter-chain transfer rate.

Figure 2.9 shows a schematic diagram of how the gate electrode affects the concentration of charge carriers in the semiconductor. When no gate voltage is applied, as in Figure 2.9a, a "flat band" situation is observed where no charges flow between the source and the drain. The E_F is aligned with the source and the drain, but the conducting states between them—HOMO and LUMO—are energetically far from the Fermi level. For a P-channel OTFT, the negative gate voltage increases the HOMO level closer to Fermi level, which forms a channel and permits charge to flow from source to drain as shown in Figure 2.9b. In addition to the gate voltage, the increase in drain voltage, as shown in Figure 2.9c, acts as a driving force for the charges to flow between drain and the source.

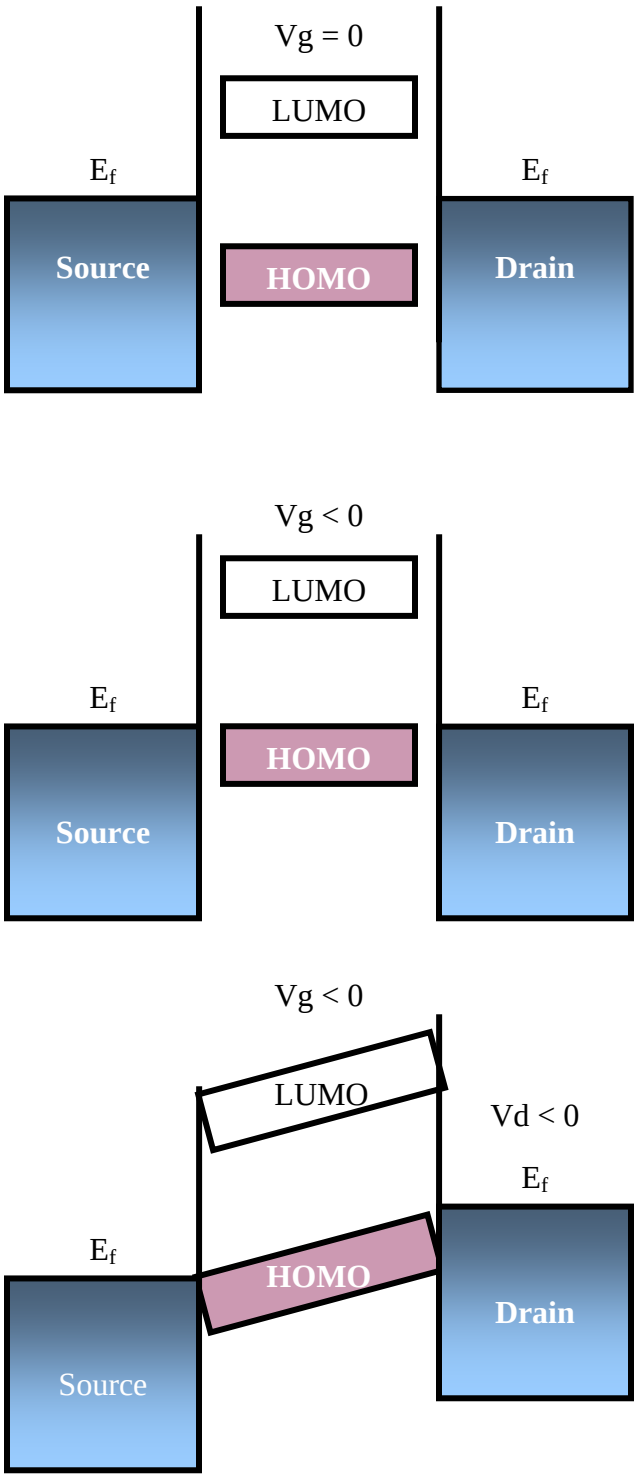

Figure 2.9. Schematic illustration of OTFT operation (a) when no gate voltage is applied, (b) when gate voltage is applied (c) when drain voltage is applied in addition to the gate voltage.

A typical I-V plot obtained during the electronic measurement of a P-channel OTFT is shown in Figure 2.10. As the voltage between the source and the drain increases, the current flowing between them gradually increases linearly according to Ohm's law. As the voltage increases further, a "pinch-off" region is observed followed by a saturation level. Once the saturation region is reached, the increase in drain voltage does not cause increase in current.

When gate voltage is increased, more charges accumulate at the interface of the dielectric and the semiconductor, increasing the width of the channel, and thus greater current flow is observed. In addition, the pinch-off voltage and the saturation current levels are both greater when more negative V_G was applied. Typically, a linear region is experienced in the region where $V_{SD} < V_G$; a pinch off is observed when V_{SD} approaches V_G and a saturation occurs when $V_{SD} > V_G$.

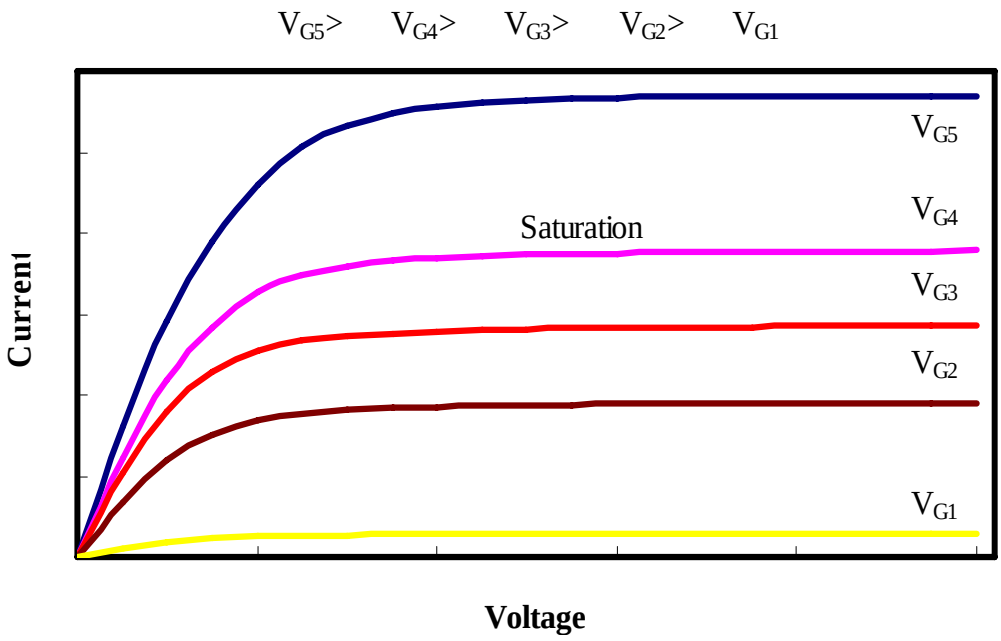

Figure 2.10. I-V characteristics plot for a typical OTFT. When V_D is applied, the charges flow between source and the drain until a saturation level is reached. The increase in Gate voltage V_G increases the current level in the OTFT.

Equation 2.4 describes the linear region of the I-V plot of an OTFT.[24]

$$I_D = \frac{W}{L} C_i \mu \left(V_G - V_T - \frac{V_D}{2} \right) V_D \tag{2.4}$$

Here I_D is the current flowing between source and the drain, W and L are the width and length of the channel, μ is the charge mobility in the semiconductor. V_G is the gate voltage and V_T is the threshold voltage which accounts for the voltage dropped across the dielectric layer due to interface states and impurities and is also the point turn on point of the device.

In the saturation region of the plot, V_{SD} is replaced by V_G-V_T which results in Equation 2.5.

$$I_D = \frac{W}{2L} C_i \mu (V_G - V_T)^2 \tag{2.5}$$

where there is almost no voltage dependence on current in this region.

The concentration of charge carriers during linear, pinch-off, and saturation levels depicted by the I-V plot are illustrated in Figure 2.11a, b, and c respectively. When gate voltage is applied, the electric field across the dielectric draws the majority carriers to the interface of semiconductor and the gate dielectric layer. These charges form a P-channel illustrated by a white band in Figure 2.11a, which permits charge flow between source and the drain. At pinch-off voltage, a depletion region starts to form around the electrode as the charges density approaches zero (Fig. 2.11b), and reaches zero at saturation (Fig. 2.11c).

(a) Linear Region

$V_D < V_G$

(b) Pinch-off Region

$V_D \sim V_G$

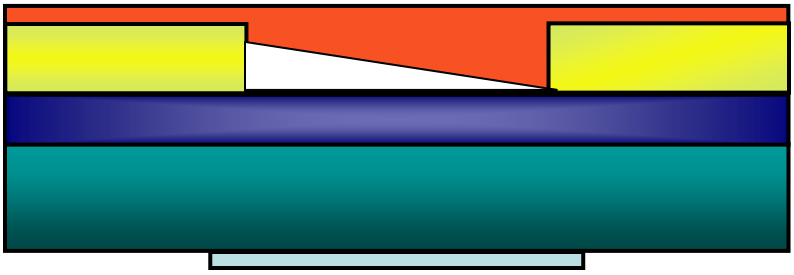

(b) Saturation Region

$V_D > V_G$

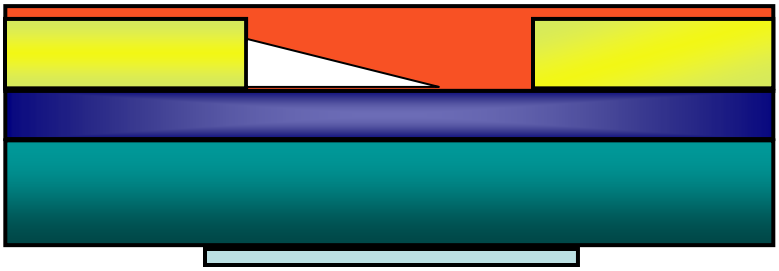

Figure 2.11. Illustration of different regimes during an OTFT operation. (a) linear region, (b) pinch-off region, and (c) saturation. [1]

2.5. OTFT Performance

The utility of an OTFT is gauged by several measures for its performance. The charge mobility, μ, describes how easily charge carriers can move within the active layer under the influence of the electric field. The switching speed of an OTFT is dependent on mobility; therefore high mobility values are ideally desired. The switching speed of an OTFT is dependent on mobility; therefore high mobility values are ideally desired. Because the charges are not delocalized, and transport by hopping mechanism, the OTFTs typically have mobility values of 10^{-5} to 10^{-1} $cm^2 V^{-1} s^{-1}$. The border line between band-transport and a hopping mechanism is usually taken at the mobility between 0.1- 1 $cm^2 V^{-1} s^{-1}$.[12] For comparison, amorphous Si has a mobility of 0.1-1, and poly-crystalline Si has a mobility of upwards of 1000 $cm^2 V^{-1} s^{-1}$.

The field effect mobility in OTFT is calculated from the following equation.

$$\mu = \frac{L}{WC_{ox}V_{SD}}\left(\frac{\partial I_{SD}}{\partial V_G}\right) \tag{2.6}$$

where μ is the field effect mobility, W is the channel width, L is the channel Length (both measured in cm), $\frac{\partial I_{SD}}{\partial V_G}$ is the slope in the turn-on curve, and C_{ox} is capacitance per unit area (F/cm).

A variety of factors affect the mobility of charge carriers and performance of OTFT. We have considered 2 alternate gate dielectric layers for the OTFT the device post, and post fabrication treatments such as annealing and doping to improve the mobility of the OTFT. The gate material which capacitively couples the active semiconductor layer and the contact metal electrodes play a vital role in the performance of OTFT. A dependable gate material

should have low defect densities, a smooth surface with very little roughness and form sharp interface which facilitates good morphology of the subsequent active layer deposition. Doping increases the total number of charge carriers. The dopants can also fill up the trapping sites at the interface[25] and shorten hopping distances between the increased number of hopping centers to facilitate inter-chain charge transfer.[26] Annealing also improves mobility by bringing the hopping sites closer together by densification.[14] The details of this study will be presented in Chapter 5.

The "on/off" ratio is indicative of the switching performance of an OTFT, and is defined as the ratio of current flowing between the source and the drain in the "on" and the "off" states. A low current is desired in the off state to minimize or eliminate leakage current in the inactive state. An on/off ratio as high as 10^6 have been reported for some OTFT's, but a much lower value is usually observed.[12]

2.6. OTFT Design and Geometry

In the final section of this Chapter, two different designs of an OTFT are considered. The working technology of a MOSFET and OTFT has been discussed in Chapter 1. When gate voltage is applied in an OTFT, an accumulation layer of charges are formed at the interface of the gate dielectric layer and the organic semiconductor layer (Fig. 1.2).

Typically, an OTFT is constructed using an inverted gate stack, and the two designs of OTFT as shown in Figure 2.12 are easy to fabricate and hence widely used. The bottom contact architecture is shown in Figure 2.12a and the top contact structure is shown in Figure 2.12b. The bottom contact is fabricated by first depositing the source and drain lines on an

oxide substrate, and the semiconductor film is spin coated on this structure. This design is easy to fabricate and the resistance for charge transport between source and the drain is minimized. However, it is difficult to measure the film thickness on the source and drain structures.

In the top contact structure, the substrate oxide is coated with film, and then the metal lines for the source and drain contacts are deposited by vacuum evaporation as quickly as possible to prevent the semiconductors from decomposing at high temperatures. In this design, the spin coated film thickness is easy to measure ellipsometrically. During our experiments, the bottom contact device performed better than the top contact devices, possibly due to increased resistivity in the top contact. The distance between the source and drain is the shortest if the charge carriers are transported at the air-semiconductor interface in Figure 2.12b. However, the charge carriers travel from source to drain by forming a channel at the semiconductor-dielectric interface where the electric field is the greatest. The charges thus have to travel an added distance to and from the contacts to the lower interface as indicated by the trajectory of the black dots shown in Figure 2.12b. This added distance increases the resistance, which results in lower current levels observed for this configuration.

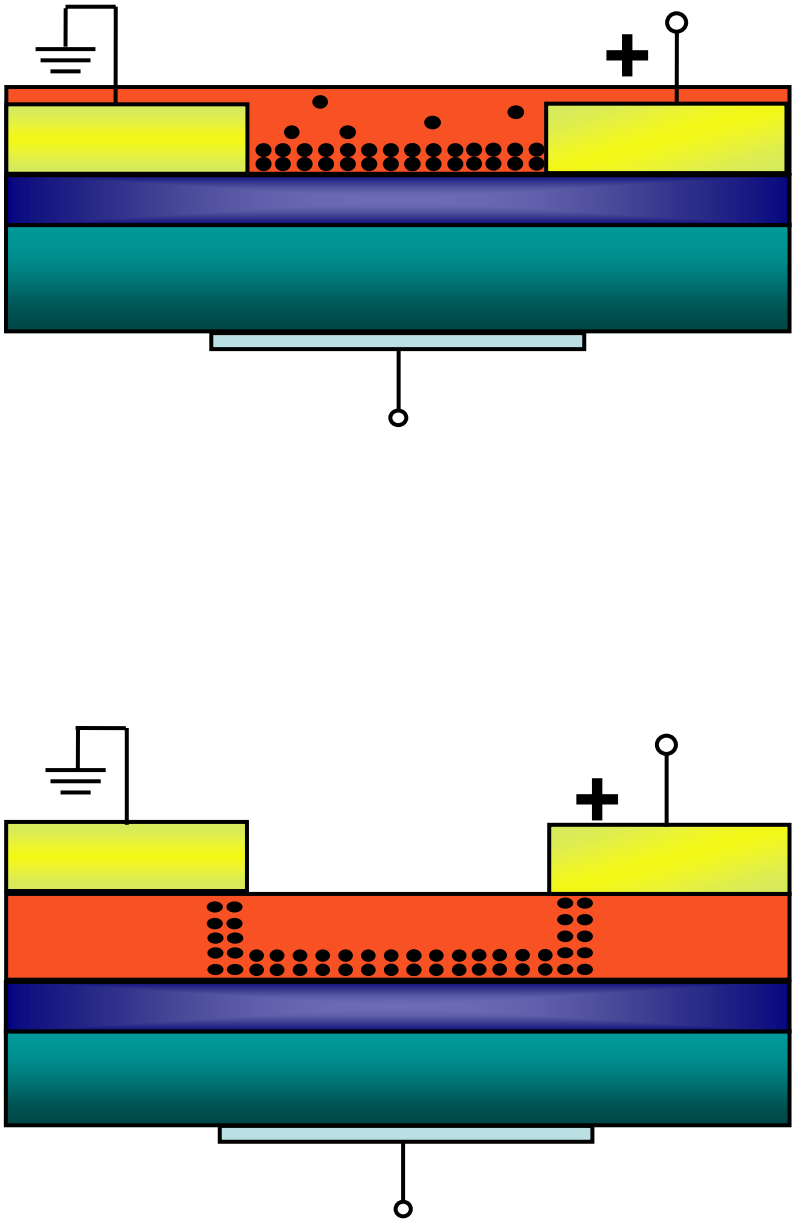

Figure 2.12. Two inverted gate OTFT designs. (a) bottom gate design and (b) top gate.

2.7. Electrical Properties Measurement

The electrical measurements were carried out using a Keithley 236 Source Measure Unit and an additional power supply was used to supply the Gate voltage. The custom probe station was facilitated with two probe manipulators from Signa Corporation connected to the source and drain electrodes. Software to automate the data collection process was complied in LabVIEW™.

The vacuum enabled chuck was used to hold the sample firmly on the station, and to act as the gate electrode during the measurement. A schematic diagram of a custom vacuum chuck is given in Figure 2.13. The reverse side of Si substrate was sanded with a diamond scriber to remove SiO_2 layer and Ga-In eutectic coating was applied with a Q-Tip™ to make an ohmic contact between the device and the gate electrode.

The voltages reported here are source-drain voltage and source-gate voltages, with the source electrode grounded. Software assisted averaging of multiple data sets was carried out.

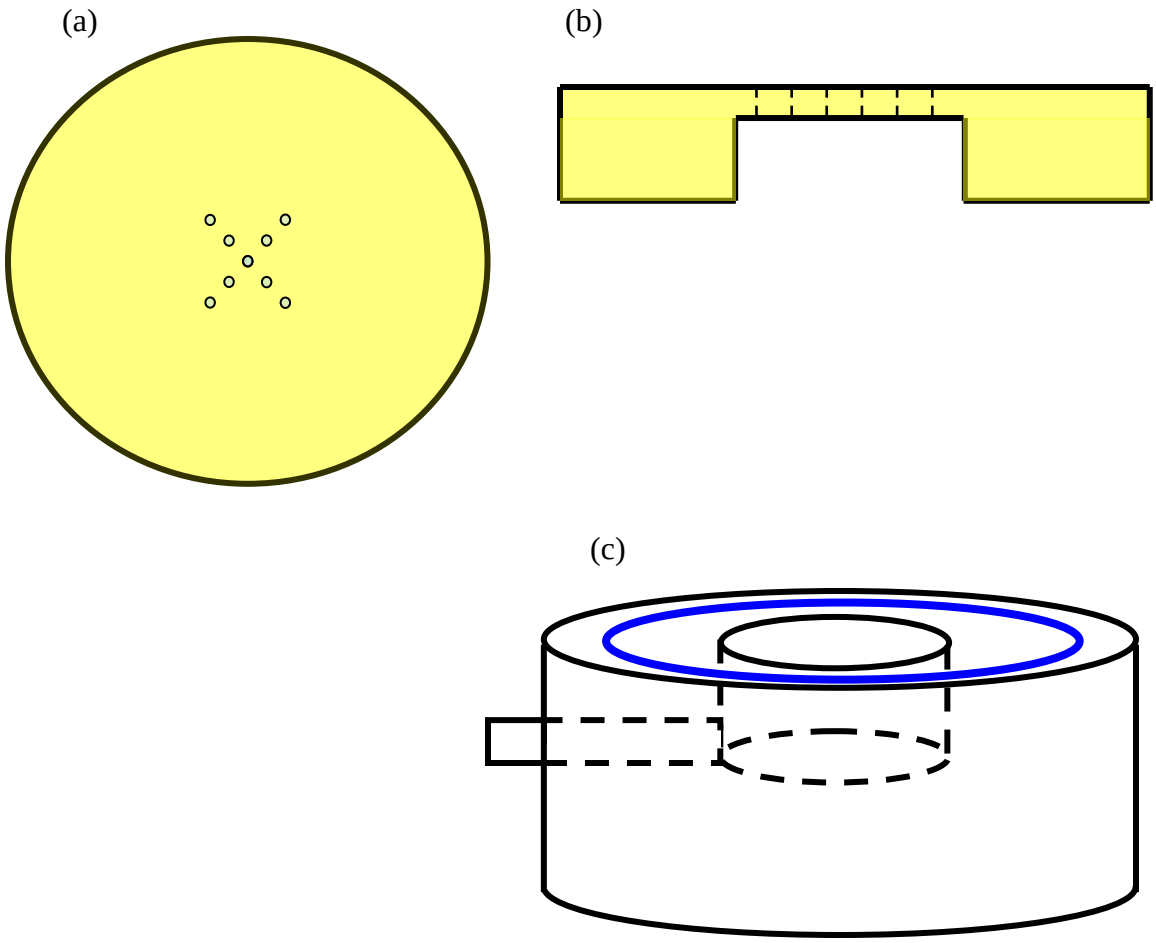

Figure 2.13. Schematic diagram of a vacuum enabled chuck (a) top view of brass plate with 0.5 mm holes drilled. (b) cross section view ofof the brass chuck showing .5 mm hole and a cavity. (c) is the Teflon base bored in the center, an outlet is also drilled to for vacuum tubing. An o-ring helps ensure tight fit between the brass top and Teflon base.

2.8. References

1. Chesterfield, R. J. Newn-channel organic semiconductors for thin film transistors. Ph.D., University of Minnesota, United States -- Minnesota, 2004.

2. Yang, D.; Shrestha, R. P.; Dingemans, T. J.; Samulski, E. T.; Irene, E. A., Optical properties of N,N'-bis(3-phenoxy-3-phenoxy-phenoxy)-1,4,5,8-naphthalene-tetracarboxylic diimide by spectroscopic ellipsometry. *Thin Solid Films* In Press, Corrected Proof.

3. Budavari, S., *The Merck index: an encyclopedia of chemicals, drugs, and biologicals*. 11th, centennial ed.; Merck: Rahway, N.J., U.S.A., 2001; p (various pagings).

4. Dimitrakopoulos, C. D.; Malenfant, P. R. L., Organic thin film transistors for large area electronics. *Advanced Materials* **2002,** 14, (2), 99-+.

5. Schon, J. H., High mobilities in organic semiconductors: basic science and technology. *Synthetic Metals* **2001,** 122, (1), 157-160.

6. Butko, V. Y.; Chi, X.; Lang, D. V.; Ramirez, A. P., Field-effect transistor on pentacene single crystal. *Applied Physics Letters* **2003,** 83, (23), 4773-4775.

7. Cornil, J.; Beljonne, D.; Calbert, J. P.; Bredas, J. L., Interchain interactions in organic pi-conjugated materials: Impact on electronic structure, optical response, and charge transport. *Advanced Materials* **2001,** 13, (14), 1053-1067.

8. Ling, M. M.; Bao, Z. N., Thin film deposition, patterning, and printing in organic thin film transistors. *Chemistry Of Materials* **2004,** 16, (23), 4824-4840.

9. Samuel, I. D. W., Polymer electronics. *Philosophical Transactions of the Royal Society of London Series a-Mathematical Physical and Engineering Sciences* **2000,** 358, (1765), 193-210.

10. Garnier, F., Specificity and limits of organic-based electronic devices. In *Photonic And Optoelectronic Polymers*, 1997; Vol. 672, pp 420-436.

11. J. Veres; Ogier, S. D.; Leeming, S. W.; Cupertino, D. C.; Khaffaf, S. M., Low-<I>k</I> Insulators as the Choice of Dielectrics in Organic Field-Effect Transistors. *Advanced Functional Materials* **2003,** 13, (3), 199-204.

12. Horowitz, G., Organic field-effect transistors. *Advanced Materials* **1998,** 10, (5), 365-377.

13. Granholm, P.; Paloheimo, J.; Stubb, H., Charge transport in thin films of polyaniline: Variable-range hopping in a parabolic quasi-gap. *Physica Status Solidi B-Basic Research* **1998,** 205, (1), 315-318.

14. Kobayashi, A.; Ishikawa, H.; Amano, K.; Satoh, M.; Hasegawa, E., Electrical-Conductivity Of Annealed Polyaniline. *Journal Of Applied Physics* **1993,** 74, (1), 296-299.

15. Godet, C., Variable range hopping revisited: the case of an exponential distribution of localized states. *Journal of Non-Crystalline Solids* **2002,** 299-302, (Part 1), 333.

16. Epstein, A. J.; Lee, W. P.; Prigodin, V. N., Low-dimensional variable range hopping in conducting polymers. *Synthetic Metals* **2001,** 117, (1-3), 9.

17. Mott, N. F., *Canadian Journal of Physics* **1956,** 34, 1356.

18. Miller, A.; Abraham, E., *Physical Review* **1960,** 120, 745.

19. Feast, W. J.; Tsibouklis, J.; Pouwer, K. L.; Groenendaal, L.; Meijer, E. W., Synthesis, processing and material properties of conjugated polymers. *Polymer* **1996,** 37, (22), 5017-5047.

20. Comber, P. G. L.; Spear, W. E., Electronic Transport in Amorphous Silicon Films. *Physical Review Letters* **1970,** 25, (8), 509.

21. Jung, S. Y.; Yao, Z., Organic field-effect transistors with single and double pentacene layers. *Applied Physics Letters* **2005,** 86, (8).

22. Horowitz, G.; Hajlaoui, R.; Bouchriha, H.; Bourguiga, R.; Hajlaoui, M., The concept of "threshold voltage" in organic field-effect transistors. *Advanced Materials* **1998,** 10, (12), 923-+.

23. Li, X.-Y.; Tang, X.-S.; He, F.-C., Electron transfer in poly(p-phenylene) oligomers: effect of external electric field and application of Koopmans theorem. *Chemical Physics* **1999,** 248, (2-3), 137.

24. Schroder, D. K., *Semiconductor material and device characterization*. Wiley: New York, 1990.

25. Kuo, C. T.; Weng, S. Z.; Huang, R. L., Field-effect transistor with polyaniline and poly(2-alkylaniline) thin film as semiconductor. *Synthetic Metals* **1997,** 88, (2), 101-107.

26. Paterno, L. G.; Mattoso, L. H. C., Influence of different dopants on the adsorption, morphology, and properties of self-assembled films of poly(o-ethoxyaniline). *Journal of Applied Polymer Science* **2002,** 83, (6), 1309-1316.

CHAPTER 3 - ELLIPSOMETRY

3.1. Overview

Ellipsometry is a powerful, non-destructive optical technique that permits the study of a layered film system, and has the capability of providing information regarding optical properties, thickness, and morphology of thin films with great accuracy. A custom built *in situ* ellipsometer was constructed and used as the primary technique in this research to characterize the optical properties of poly(*o*-methoxyaniline) (POMA) and other thin films. An in depth description of polarized light and the ellipsometry technique can be obtained elsewhere.[1] In this chapter, a brief consideration will be given to the nature of polarized light, its transmission through isotropic media, and reflection at the interface. A description of the design and fabrication of the *in-situ* ellipsometer will also be presented here. Interfacing software program was written in LabVIEW™ was used to automate the data collection process;the compilation of this program will also be discussed. Several key issues in automated data collection including current to voltage conversion circuitry, general optics alignment, and calibration process will also be presented.

3.2. Introduction to Polarized Light

A light wave is an electromagnetic (EM) transverse wave comprised of an electric field, E, and magnetic field, B. These orthogonal components oscillate perpendicular to the direction of the propagation of the wave as shown in Figure 3.1. Z is the direction of propagation of EM wave and E and B are the two components.

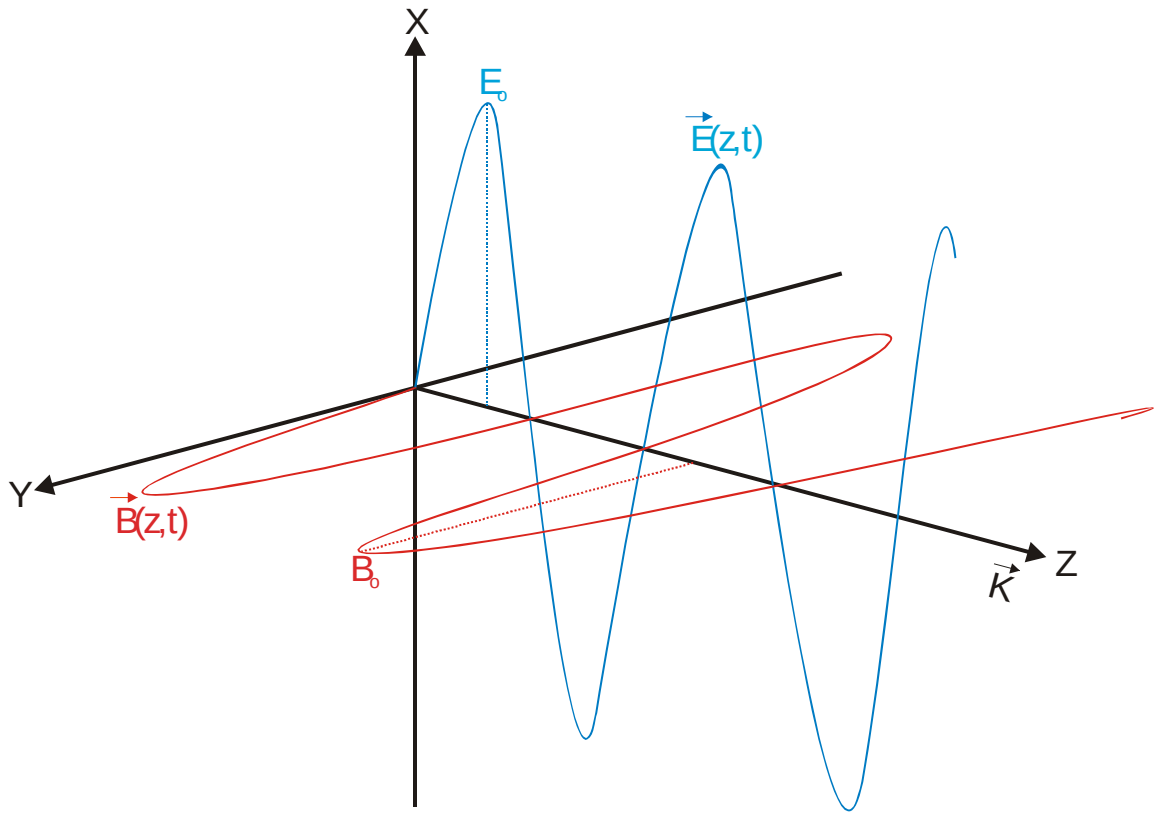

Figure 3.1. Light represented as an electromagnetic transverse plane wave

The EM wave can vibrate in many directions orthogonal to it propagating direction in its unpolarized state. When plane or linearly polarized, the propagating EM wave can only oscillate in a single direction. Figure 3.2a depicts an unpolarized light propagating from the back of the page towards the reader. Figure 3.2b depicts the linearly polarized light propagating in the same direction. Given the appropriate conditions, both the E and B components can be polarized, and can interact with matter at different capacities. However, the ellipsometry technique is based on the interaction of the polarized electric field E with matter. Therefore, only the polarization of the E component of EM wave will be discussed.

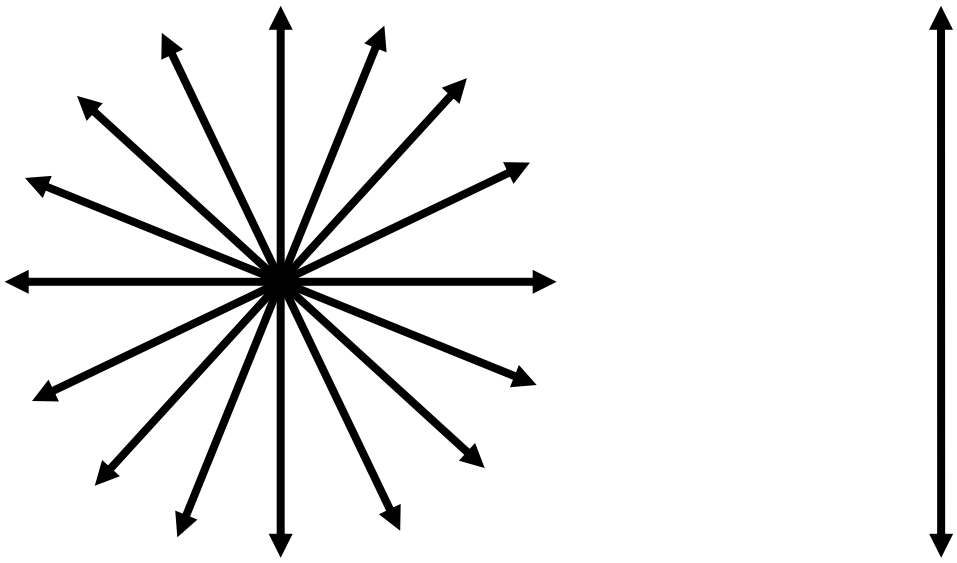

Figure 3.2. A comparison between unpolarized light and linearly polarized light traversing from the back of the page towards the reader.

Figure 3.3a shows in greater detail a linearly polarized E component of EM wave propagating from the top left of the page to the bottom right along the z direction. Wave 1 and Wave 2 represent the orthogonal components of the E vector projected on x and y

directions respectively. Maxwell's relations can be used to describe this plane wave as follows:

$$E(z,t) = E_0 \sin\left(-\frac{2\pi}{\lambda}(z - vt) + \xi\right) \tag{3.1}$$

Where E_0 is the amplitude, λ is the wavelength, z is the direction of propagation, ν is the velocity, t is the time and ξ is an arbitrary phase constant. The orthogonal components of E projected on x and y axes are labeled E_x and E_y and these vectors are related to E by Equation 3.2.

$$E = \left(E_x^2 + E_y^2\right)^{1/2} \tag{3.2}$$

Figure 3.3b demonstrates that when E_x and E_y are in phase and equal in amplitude, their vector addition results in a linearly polarized wave. Similarly, Figure 3.4 and 3.5 illustrate the propagation of elliptically polarized light and circularly polarized light. It should be noted that the linear and circular polarizations are special cases of the more general elliptically polarized light. The circular polarization is obtained when the two orthogonal vectors E_x and E_y are equal in amplitude, but 90° out of phase (one reaches a maximum while the other is at a minimum). The resultant of these two out of phase vectors is illustrated in Figure 3.4b. Any other combination of phase and amplitude results in elliptical polarization as shown in Figure 3.5a and b.

(a)

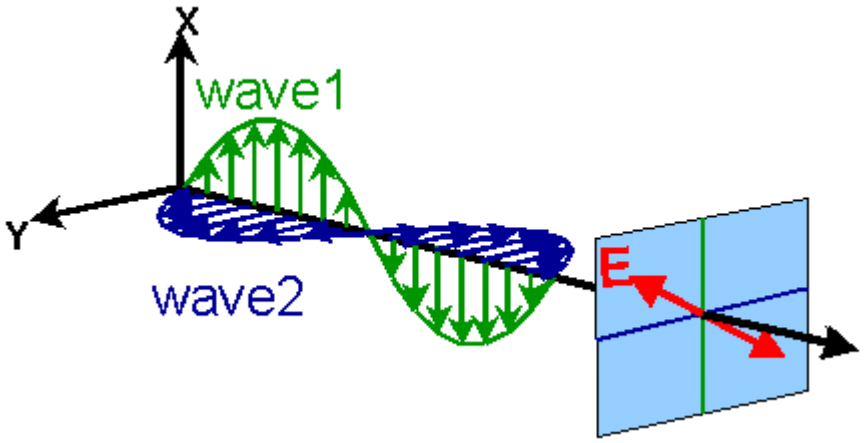

(b)

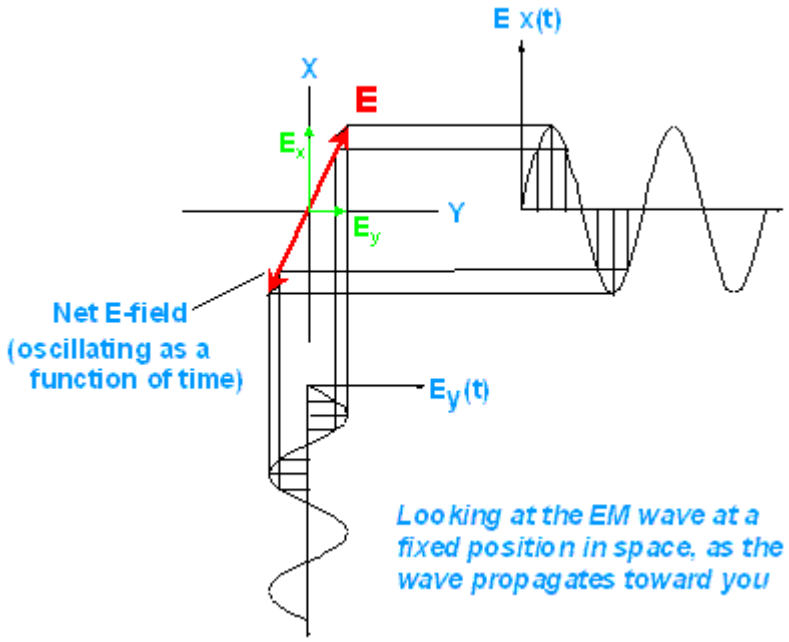

Figure 3.3 Linear polarization expressed with two orthogonal components E_x and E_y. Reproduced with permission from JA Woollam Company.

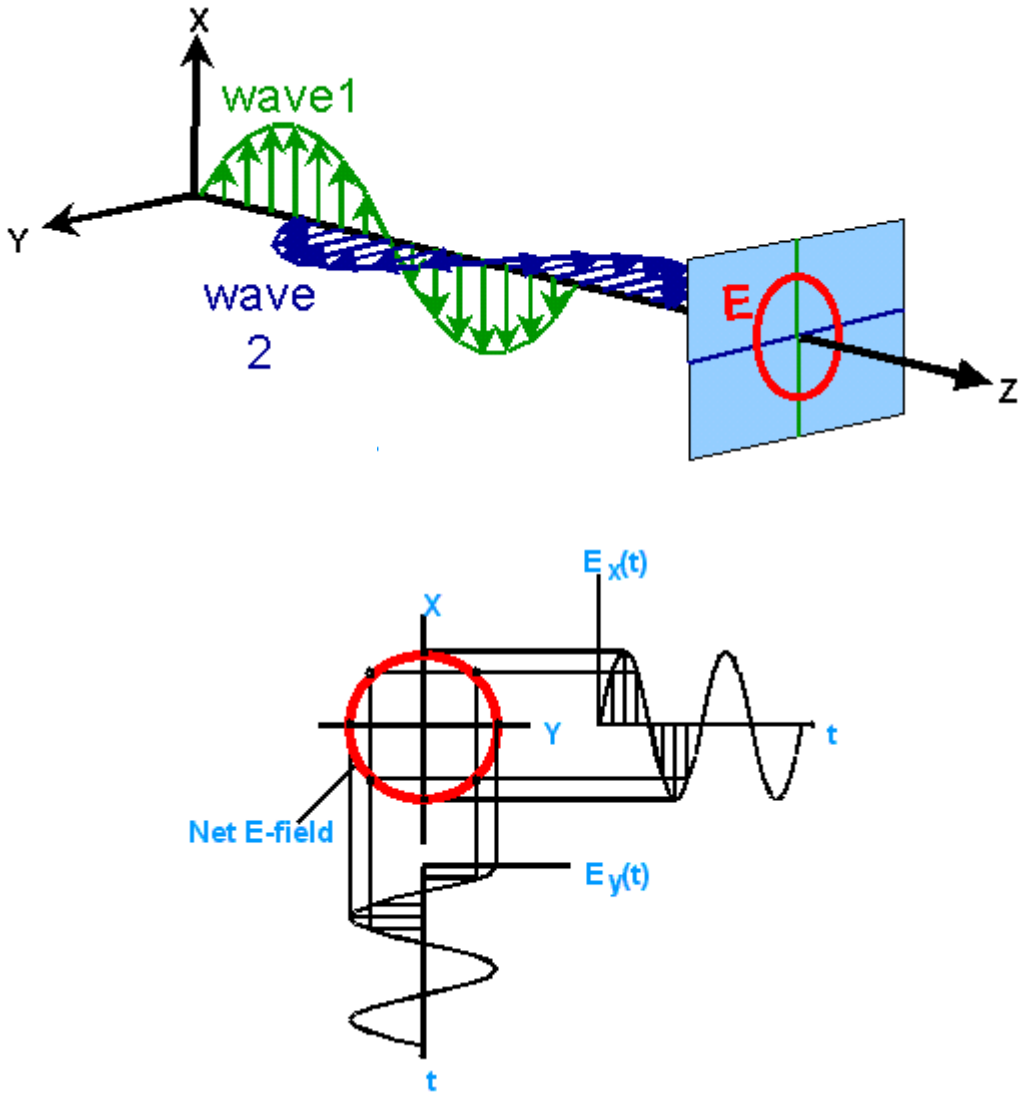

Figure 3.4. Second special case-the circular polarization of elliptical polarization of E wave, where E_x and E_y are equal in amplitude and 90° out of phase. Reproduced with permission from JA Woollam Company.

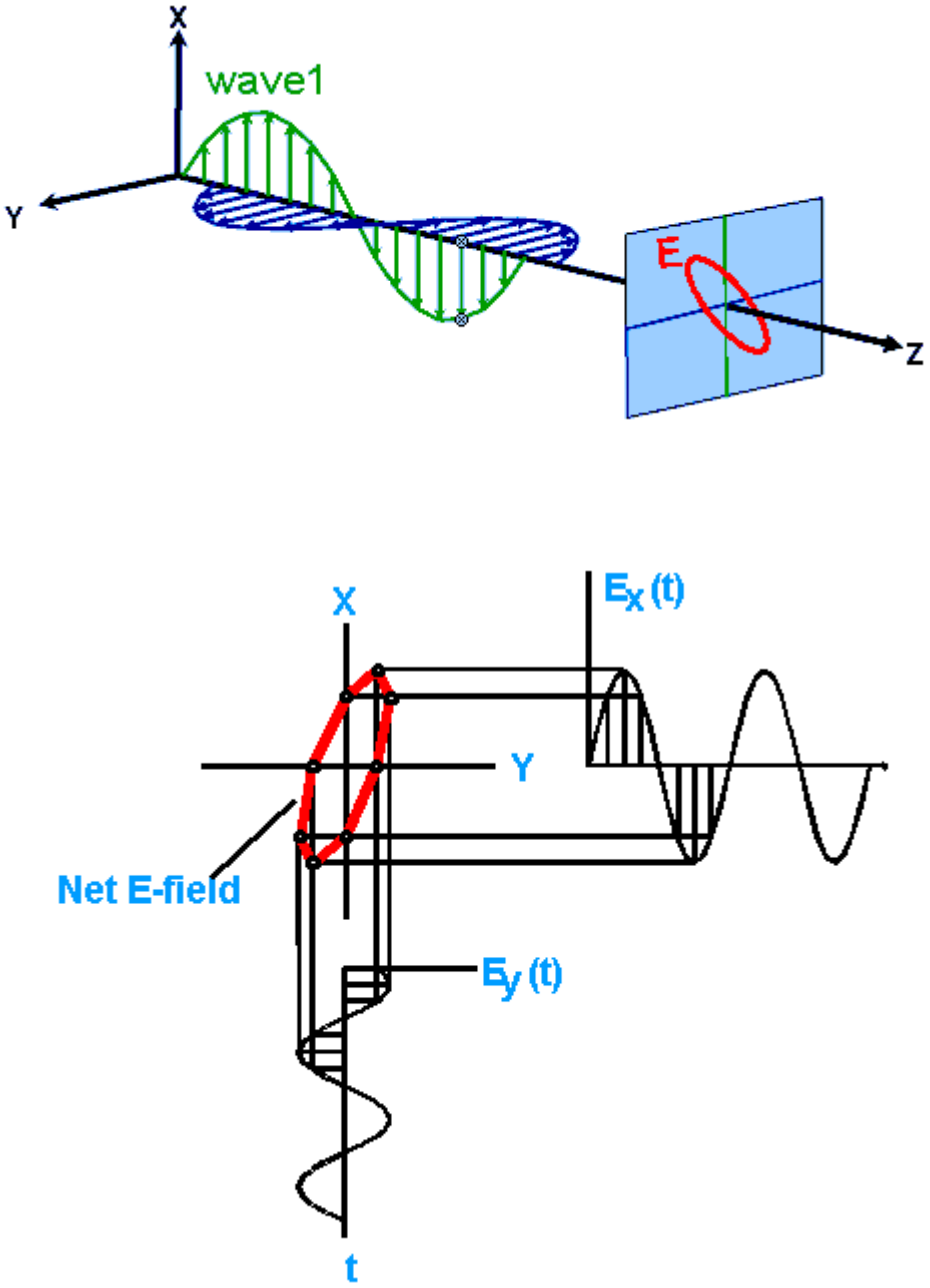

Figure 3.5. Elliptical polarized wave. Arbitrary amplitude and phase in both components.

Ellipsometry uses the ellipticity and orientation of polarized light to describe polarization and the light intensity does not play a role when extracting ellipsometric information. Since a relative measurement instead of an absolute measurement is made (typically in seen in UV-Vis spectrosocopy), ellipsometry is not prone to variation in the source or the detector and monolayer sensitivity can be obtained from this technique.[2] Figure 3.6 illustrates two elliptically polarized wave forms. While the intensity of the second one is larger than the first, the orientation and ellipticity of these two ellipses are the same.

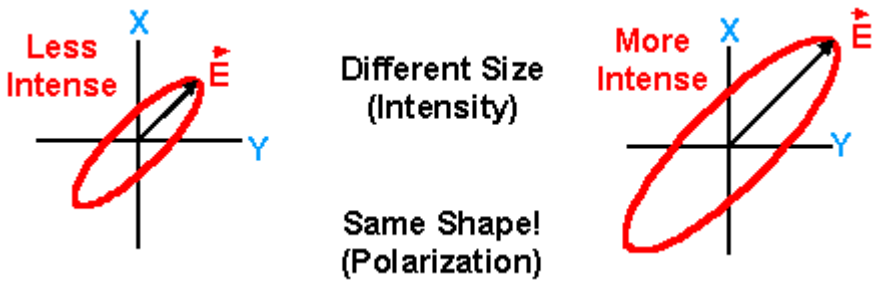

Figure 3.6. Illustration of elliptically polarized waves with two different intensities. The ellipticity of both the light forms is the same.

3.3. Ellipsometry

Knowledge of state of polarized light can now be used in ellipsometry, which is an optical technique to measure the change in the polarization of the reflected E wave after its interaction with matter. Figure 3.7 depicts a polarized EM wave reflecting from a sample. As seen in the figure, the incident beam, the reflected beam, and the surface normal all lie on the plane of incidence (POI shaded) and this is called specular reflection. The POI is defined by the incident ray and the normal to the sample surface.

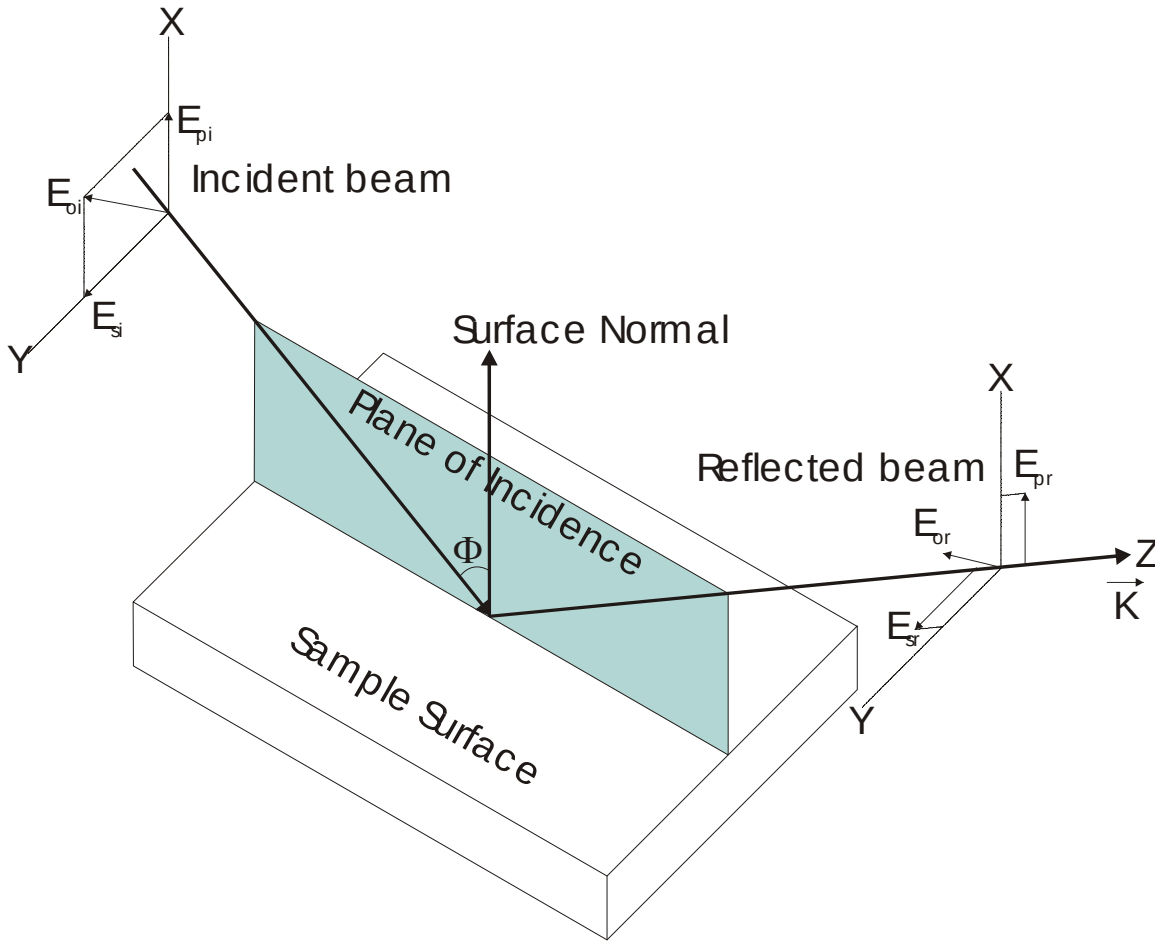

Figure 3.7. Schematic diagram showing the incident components of the polarized light, the plane of incidence, and reflected light during ellipsometry.

The components of E, E_x and E_y illustrated earlier in Figures 3.3-3.5 are designated in reference to the POI in Figure 3.7. The component which is parallel to the POI is called E_p, and E_s (s from German word, *senkrecht*, meaning perpendicular) is normal to the POI. As above from Equation 3.2, E is defined in terms of E_p and E_s as follows:

$$E = \left(E_p^2 + E_s^2 \right)^{1/2} \tag{3.3}$$

Figure 3.7 shows that E_p and E_s are in phase with the incident beam before the interaction with the material. The polarized light can interact with the material causing the polarization of the reflected beam to change. This change in the reflected beam is analyzed and is used to determine the optical properties of the material. The quantification of the change in phase between the E_s and E_p in the reflected beam is called delta, Δ, which can range in value from 0º to 360º, and the change in amplitude is called psi, Ψ which can have range from 0 to 90º.

The discussion can extended further into a film covered substrate as shown in Figure 3.8.

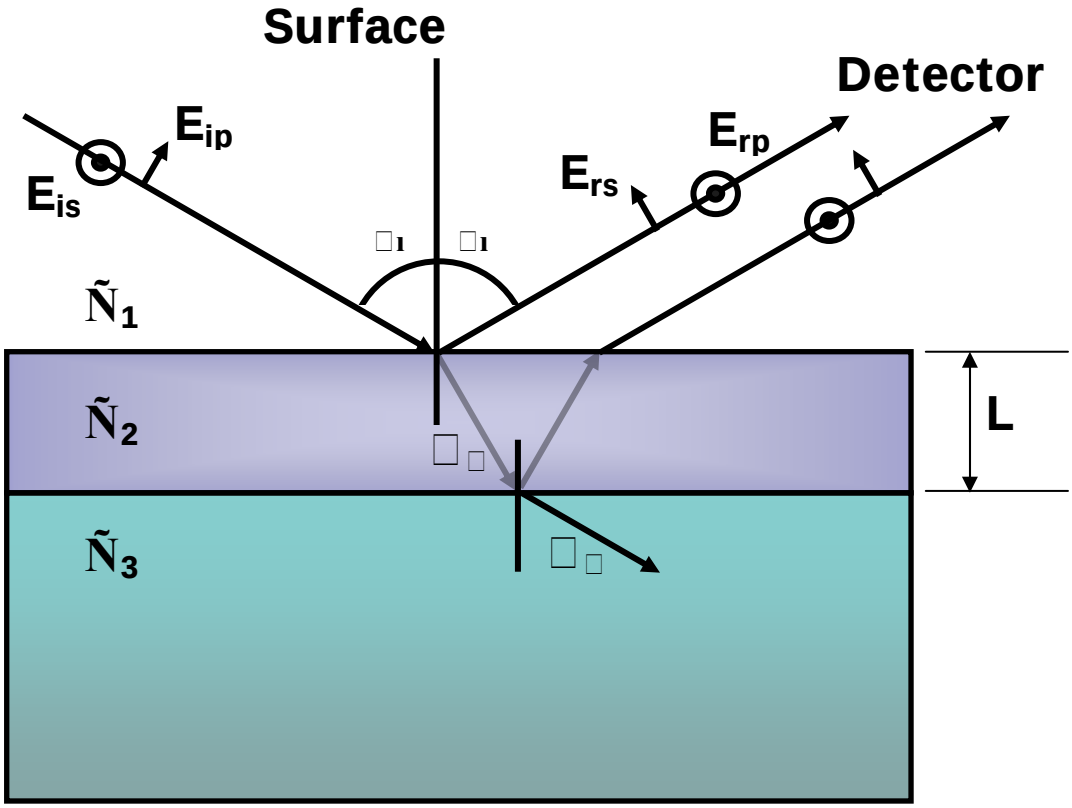

Figure 3.8. The interaction of polarized light with a film-covered substrate.

Figure 3.8 shows a linearly polarized light directed at an incident angle ϕ on a film-covered substrate. The light is reflected and refracted at each interface of different mediums with complex refractive indices $\tilde{N}_1$, $\tilde{N}_2$, and $\tilde{N}_3$. This linearly polarized light undergoes changes in both amplitude and phase after the interaction with the film and the substrate. This change, quantified by Ψ and Δ can be calculated using the relationship in Equation 3.4 that is called the fundamental equation of ellipsometry that relates the measurables Δ and Ψ to the optical properties within the complex Fresnel coefficients R_p and R_s for p- and s-polarized light, respectively.

$$\rho(\phi,\lambda,\tilde{N}_i,L_i) = \frac{R_p}{R_s} = \tan\psi \exp(i\Delta) \tag{3.4}$$

The complex reflection coefficient, ρ, is a function of incident angle, ϕ, the wavelength, λ, the complex refractive index, $\tilde{N}$, and the thickness, L of the film. In most circumstances, many of these variables are fixed or predetermined e.g. ϕ and λ are experimental parameters which can be varied conveniently except during in-situ measurements where ϕ may be fixed. $\tilde{N}$, is a physical property of the material. Therefore using the multivariate analysis or simultaneous equation analysis, the $\tilde{N}$ and or L for thin films can be obtained. Results from ellipsometry can be highly accurate and very reproducible because it measures the ratio of two values and as mentioned earlier the intensity of the light source is absent from Equation 3.4.

The Fresnel reflection coefficients, R_p and R_s are defined in Equation 3.5a and b.

$$\text{(a) } R_p = \frac{r_{12}^p + r_{23}^p \exp(-i2\beta)}{1 + r_{12}^p \times r_{23}^p \exp(-i2\beta)} \qquad \text{(b) } R_s = \frac{r_{12}^s + r_{23}^s \exp(-i2\beta)}{1 + r_{12}^s \times r_{23}^s \exp(-i2\beta)} \tag{3.5}$$

In Equation 3.5, R is the total reflection coefficient, r_{12} and r_{23} are the Fresnel reflection coefficients between medium 1 and 2, and medium 2 and 3 respectively and β is defined in Equation 3.6.

$$\beta = 2\pi\left(\frac{L}{\lambda}\right)\tilde{N}_2 \cos\phi \tag{3.6}$$

Ñ, the complex refractive coefficient is related to the refractive index n and extinction coefficient k with Equation 3.7.

$$\tilde{N} = n + ik \tag{3.7}$$

Refractive index, n is related to the speed of light in vacuum, c and speed of light in the propagating medium, ν by Equation 3.8 and k is the extinction coefficient, which is related to the absorption constant α from Equation 3.9:

$$n = v/c \tag{3.8}$$

$$\alpha = \frac{4\pi k}{\lambda} \tag{3.9}$$

In equation 3.9, λ is the vacuum wavelength. Once n and k are obtained from ellipsometry, other properties that characterize a material can also be extracted. The dielectric response function, ε, which is the measure of the response of the material to the EM wave, and the pseudo dielectric function <ε> which is the cumulative response of the film(s) along with the substrate to EM wave are directly derived by substituting ρ obtained in Equation 3.4 in Equation 3.10.

$$\varepsilon = \varepsilon_1 + i\varepsilon_2 = \sin^2\phi \tan^2\phi\left(\frac{1-\rho}{1+\rho}\right)^2 \tag{3.10}$$

where ε_1 is the real component and ε_2 is the imaginary component of the dielectric function of a material. These are related to n and k from Equations 3.11a and 3.11b.

$$\varepsilon_1 = n_2 - k_2 \tag{3.11a}$$

$$\varepsilon_2 = 2\, n\, k \tag{3.11b}$$

3.4. Instrumentation of Rotating Analyzer Spectroscopic Ellipsometer.

The rotating analyzer spectroscopic ellipsometry (RASE) is a popular automatic ellipsometer configuration suitable for spectroscopic measurement for analysis of the optical properties of thin films, and surface morphology. A general RASE system is illustrated in Figure 3.9. Spectroscopic ellipsometry (SE) only requires a weak continuum light source such as a low powered xenon arc lamp (75 W) because its operation is based on photometric detection, as mentioned earlier, rather than being based on the measurement of absolute light intensity. A RASE system consists of a robust precision optical bench with two arms that house the optical, mechanical, and electrical and computational components. These components will be described separately below.

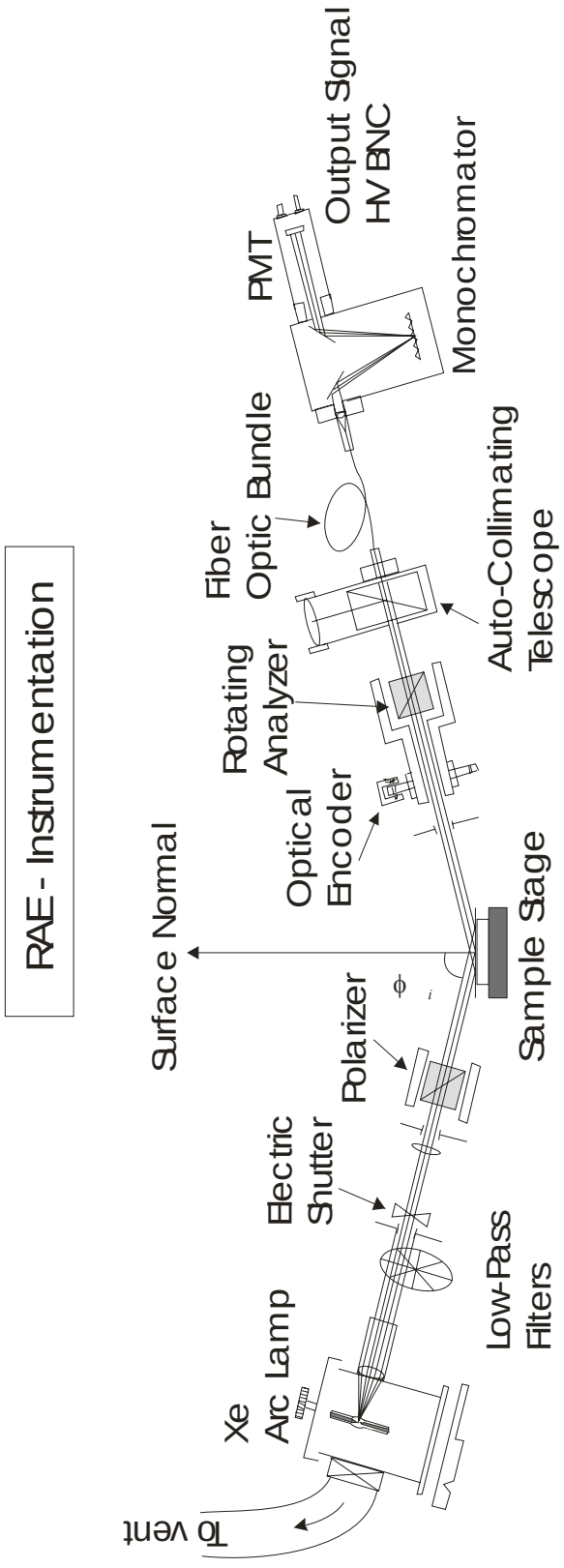

Figure 3.9. Rotating analyzer spectroscopic ellipsometer (RAE) schematic diagram

The optical components of RASE consist of a light source (Xe-arc), polarizer, rotating analyzer, monochoromator and detector PMT as shown in Figure 3.9. The output from an ellipsometer is a periodic waveform, and its Fourier Transform yields Ψ and Δ, which can be used to extract the optical properties of the film under investigation.

The Xe-arc lamp used in this system is a 75 watt lamp made by OSRAM (model # 6251 XBO-75/2, $178). Xenon-arc lamp housing (model # 66002) is used to accommodate the lamp and is powered by Oriel universal power supply (model # 68808). The lamp produces unpolarized, collimated white light in 250-750 nm (5 – 1.66 eV) range.

The collimated light from a Xe-arc lamp is linearly polarized as it passes through a fixed polarizer which is a Glan Taylor prism. The polarizing prism is housed in a rotating mount which can be rotated manually with a precision of 0.01°, and the polarization value is displayed on a rotary readout. An adjustable iris is mounted on the entrance of the polarizer housing to reduce the diameter of the light beam which strikes the sample.

An electronic shutter from Melles Griot is set up between the light source and the polarizer which is used to account for and subtract the effect of stray light and PMT dark current. The shutter control system also from Melles Griot is controlled via a TTL pulse provided from the automation software program LabVIEW™.

The next component in the optical path is the sample stage which is located at the converging point of the two optical "arms" of the ellipsometer provides the ability to control tilts in the x and y axes and z movements. The light reflecting off the sample then propagates along the optical axis of the ellipsometer, and enters a rotating analyzer through a 0.5 mm fixed iris.

This reflected beam passing through the analyzer (another Glan Taylor prism) rotating at a constant speed of (ω = 5 Hz) contains the ellipsometric information about the thin film layers under investigation on the sample stage. The rotating analyzer is mounted on a hollow shaft mounted with ball bearings and a pulley, and a 5-Hz drive motor is used to rotate the analyzer at a constant speed. The shaft containing the analyzer also houses the optoelectroic encoder which enables the digitization of the signal passing through the analyzer, which will be discussed in detail later.

The propagating light is then centered on a high grade fused silica fiber optic bundle with the help of a mounted auto-collimating telescope, and via the bundle the light is transmitted to a Czerny-Turner monochromator. The selected wavelength of light is then received by an end-on photo multiplier tube (PMT) mounted directly at the exit end of the monochromator. The Oriel 77346 PMT has a detection range from 185 to 850 nm. The photons entering the photo cathode in the PMT emit photoelectrons into vacuum. These photoelectrons are then directed by the focusing electrode voltages of the electron multiplier where electrons are multiplied by secondary emission and collected by the anode as a digital output signal.

A programmable power supply is used to control the gain in PMT by controlling the PMT voltage supply through a feedback circuit. Even though the suggested range is up to 1500 V, the ellipsometric measurements are not made above 1200 V on the PMT.

An optical encoder (R5s-360-375-EH from US digital) is mounted on the shaft containing the rotating analyzer. This optical encoder is a mechanical motion sensor which can keep track of the rotation of the axle and allows the optical signal to be digitized for computer analysis. It consists of a transparent disk with 360 uniformly patterned opaque bar

lines as shown in Figure 3.10. The disk is attached to the rotating shaft and it rotates in a slit of the optoelectronic system which consists of a point source LED illuminating system on one side and a phase array monolithic system to detect the pattern on the other side of the disk. The marking on the disc prevents the LED light to be detected by the array periodically creating TTL signal. (opaque -0 V and transparent = 5 V) as shown in Figure 3.11.

Therefore at any given time t, the light exiting from the analyzer can be recorded as a function of the instantaneous orientation of the analyzer compared to the zero azimuth position; the polarizer angle, angle of incidence ϕ are kept constant during each measurement.

Figure 3.10. Patterned line disk which rotate in the shaft between an LED and detector to produce square waves for digitization seen in Figure 3.11.

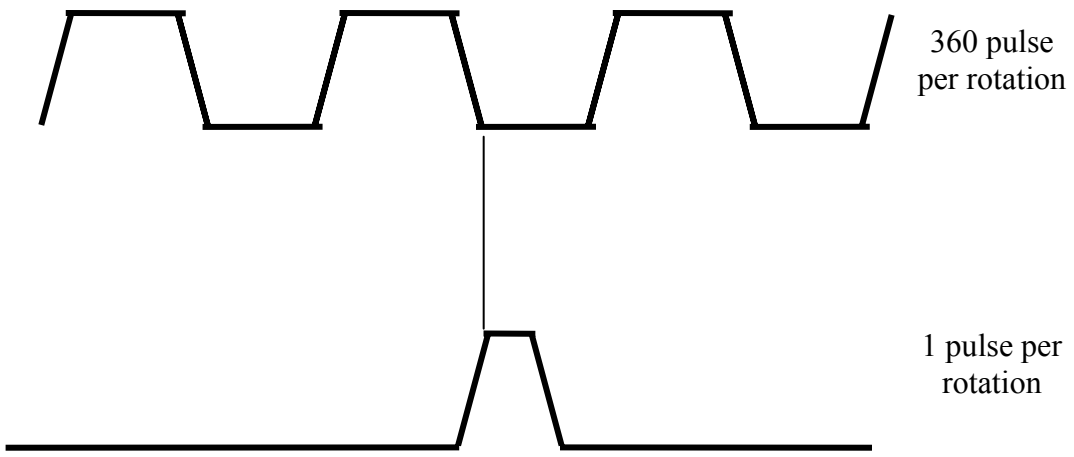

Figure 3.11. Timing diagram of the TTL pulse obtained from the optical encoder.

In addition to the regular coded lines, there is also a second line which tracks the completion of a single rotation of the disk by generating a pulse per rotation, known as the zero pulse. Thus this optical encoder can provide 360 pulses per rotation of the disc, and the onset of the pulse triggers the data collection. Therefore at any given time t, the light (electric field vector) exiting the analyzer and reaching the PMT can be expressed in a Jones Matrix treatment is presented in Equation 3.12. E_{PMT} is a function of the instantaneous orientation of the analyzer at time t compared to the zero azimuth position. The polarizer angle, P and the angle of incidence, ϕ are kept constant during each measurement.

$$E_{PMT} = E_0 \begin{pmatrix} 1 & 0 \\ 0 & 0 \end{pmatrix} \begin{pmatrix} \cos A & \sin A \\ -\sin A & \cos A \end{pmatrix} \begin{pmatrix} R_p & 0 \\ 0 & R_s \end{pmatrix} \begin{pmatrix} \cos P & \text{cin } P \\ -\sin P & \cos P) \end{pmatrix} \begin{pmatrix} 1 \\ 0 \end{pmatrix} \qquad (3.12)$$

E_0 is a constant and A for a rotating analyzer is given by Equation 3.13, where δ is the phase constant offset of the analyzer from the zero azimuth position, ω is the rotating frequency of the analyzer.

$$A = \omega t + \delta \tag{3.13}$$

The intensity of light reaching the PMT is directly related to E_{PMT} as expressed in Equation 3.14. Substituting the expansion value of E_{PMT} in Equation 3.14, Equation 3.15 is obtained.

$$I = |E_{PMT}|^2 \tag{3.14}$$

$$I = I_0\left[1+\left(\frac{\tan^2\Psi-\tan^2 P}{\tan^2\Psi+\tan^2 P}\right)\cos 2A+\left(\frac{2\tan P\cos\Delta\tan\Psi}{\tan^2\Psi+\tan^2 P}\right)\sin 2A\right] \tag{3.15}$$

Or

$$I = I_0\left(1+\alpha\cos 2A+\beta\sin 2A\right) \tag{3.16}$$

Equation 3.16 results in a sinusoidal intensity wave as seen in Figure 3.14 where I_0 is the DC signal component. The second Fourier coefficients α and β can be obtained from a Fourier analysis of the reflected wave and are the normalized to describe the phase and the relative amplitude of the ac component of the varying detected flux. A is the azimuth of the analyzer transmission axis with respect to the plane of incidence. Ψ and Δ, the ellipsometric parameters can now be expressed in terms of the measured and normalized α and β, the Fourier by using Equations 3.17 and 3.18.

$$\alpha = \frac{\tan^2\Psi-\tan^2 P}{\tan^2\Psi+\tan^2 P} = \frac{\cos 2P-\cos 2\Psi}{1-\cos 2P\cos 2\Psi} \tag{3.17}$$

$$\beta = \frac{2\tan P\cos\Delta\tan\Psi}{\tan^2\Psi + \tan^2 P} = \frac{\sin 2P\sin 2\Psi\cos\Delta}{1-\cos 2P\cos 2\Psi} \tag{3.18}$$

By inverting Equations 3.17 and 3.18, the following more familiar expression for Ψ and Δ can be obtained and is expressed in Equations 3.19 and 3.20.

$$\tan\Psi = |\tan P|\sqrt{\frac{1+\alpha}{1-\alpha}} \tag{3.19}$$

$$\cos\Delta = \frac{\beta}{\sqrt{1-\alpha^2}} \tag{3.20}$$

From this discussion, it is clear that the rotation of the analyzer helps to decipher the optical properties of sample under investigation contained in the reflected elliptical polarized light. The knowledge of the DC component, the second Fourier components (α and β) of the detected wave and the polarization state of the incident wave ρ yields the ellipsometric parameters Ψ and Δ as initially presented in Equation 3.4. This set of information can be used to extract the refractive index, extinction coefficient and thickness of the thin film from iterative calculations. Commercial software was used in for this purpose and the details of optical modeling are presented in Section 3.6.

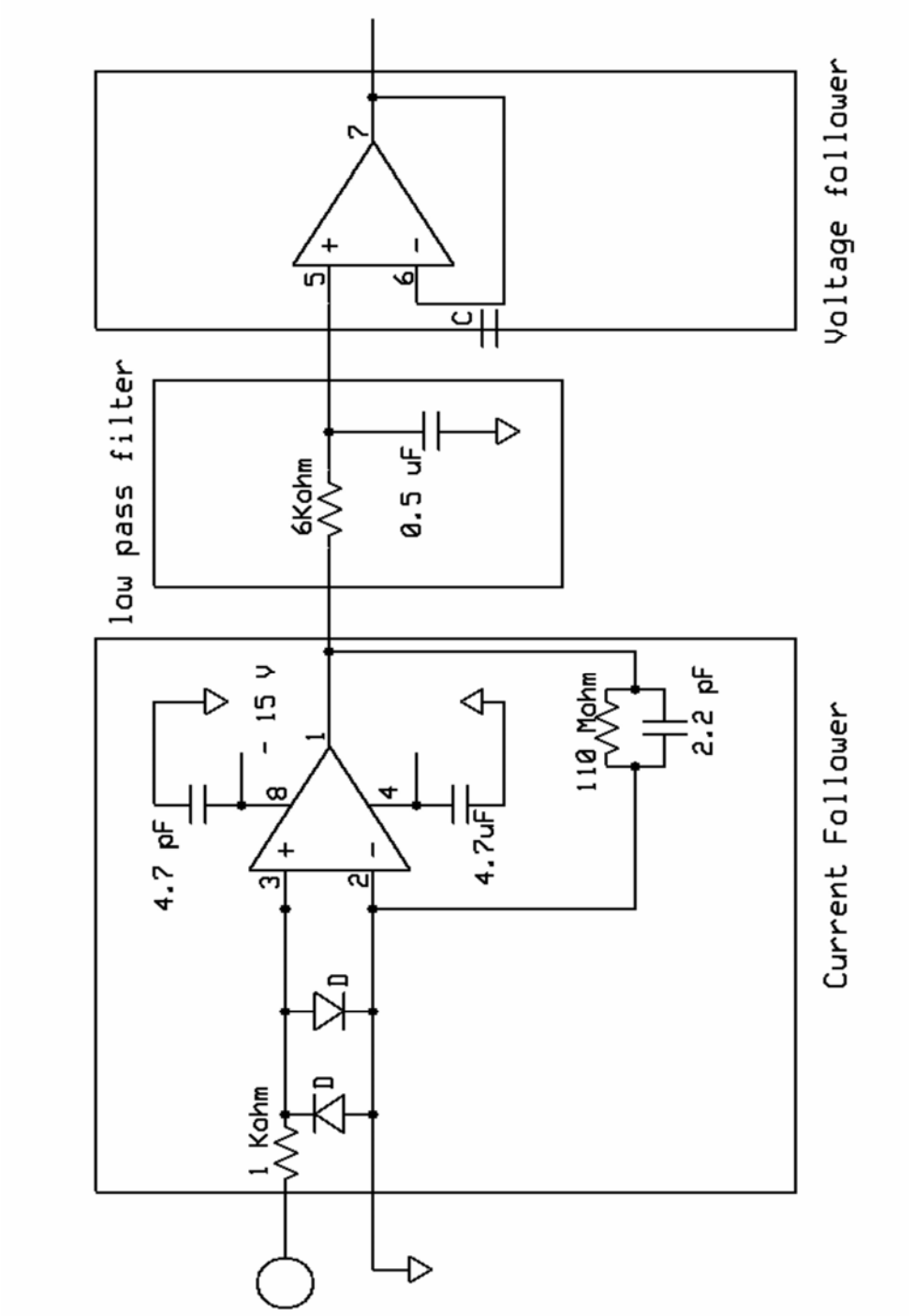

Figure 3.12. Electronic circuit diagram for the current follower, low pass filter and I-V conversion.

The electronic circuit shown in Figure 3.12 is used before the current signal from the PMT is introduced to the data acquisition system. A current follower (section A) first amplifies the signal and converts the negative current output from the PMT to voltage within the operational range of analog digital conversion (A/D) hardware of 10 V. The low pass filter has a cut off frequency of 53 Hz which is used to attenuate the 60 Hz line signal from AC source as well as other high frequency harmonics and noise. The low-pass filter circuit has unwanted side effects of a "zero level" DV voltage level and a small phase shift relative to the input signal. Therefore an appropriate value of resistor and capacitor (here 6 KΩ and # 0.5 μF) are used to minimize the zero level dc voltage without compromising the filtering ability. The phase change is corrected with a phase constant, η factor during the calibration process.

The signal is then channeled through a voltage follower which increases the output impedance and connects to BNC 2090 (National Instruments™) connector board for analog to digital conversion. BNC-2090 is a shielded, rack-mountable adapter with signal-labeled BNC connectors and is used to simplify connection to and from the analog, digital, trigger, and counter/timer signals. It is connected to an E-series DAC board housed inside the computer from NI™ from the rear 68-pin connectors.

The schematic diagram of this interface of the ellipsometer with the computer via the DAC board is illustrated in Figure 3.13.

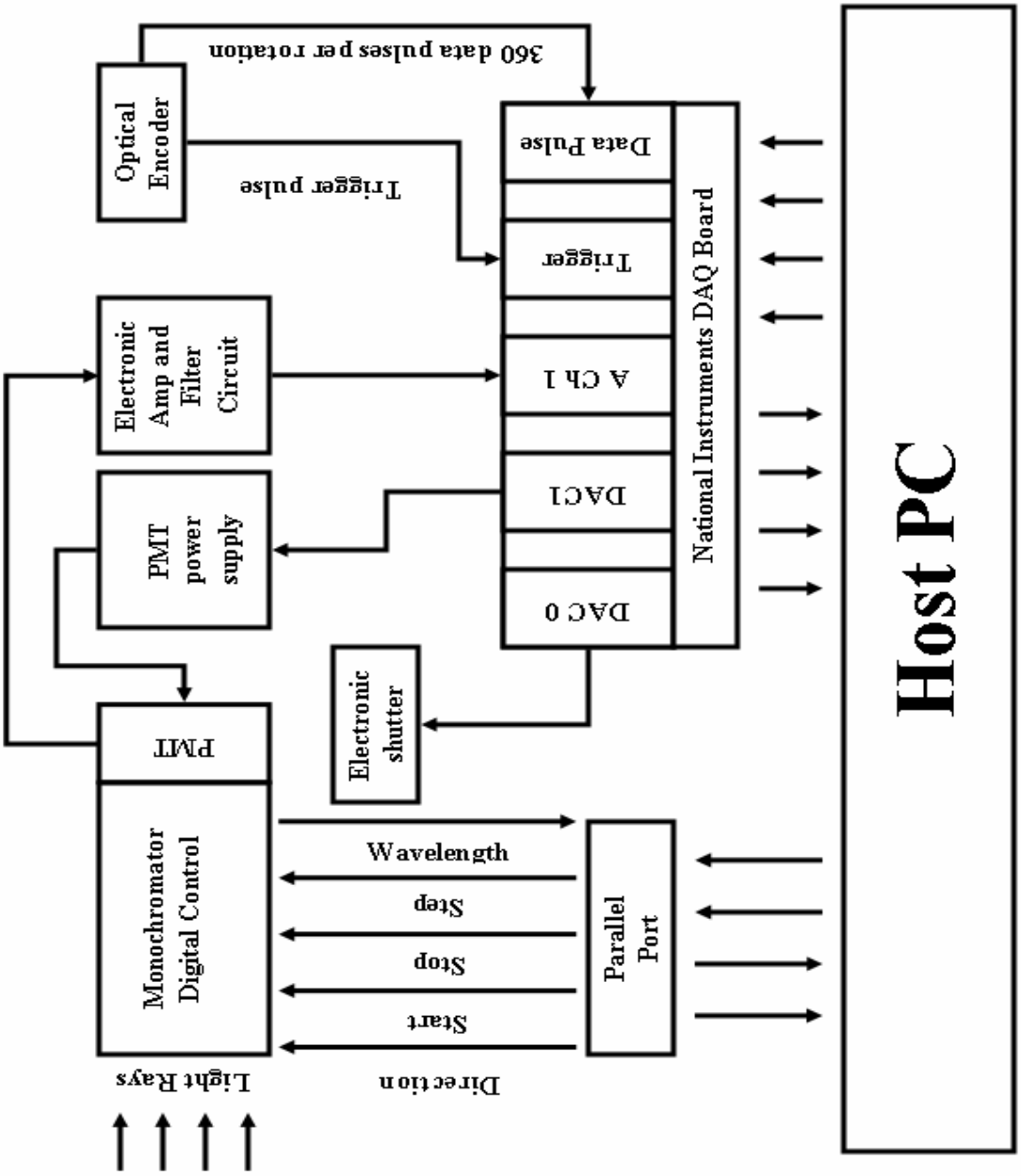

Figure 3.13. Schematic diagram of host PC controlling the data acquisition board and ellipsometer

3.5. Software Control and System Automation

The automation of the ellipsometer is managed by LabVIEW™ from National instruments. It is a graphical programming language written in G (for graphical) unlike the text programming languages of C++, Fortran, Basic, etc. LabVIEW is written in programming language, which is composed of many "nodes" wired together, and has continuous auto-compiling. i.e. checks for errors and notifies in real time.

The program complied for SE has a control panel with 4 tabbed independent operations as follows:

- Alignment
- Fine tune α_1 & β_1 alignment
- Spectroscopic Ellipsometry Data collection
- Calibration.

The programming details including the control panel interface and the programming diagram from labVIEW™ software in Appendix A and a simple description of each tabbed function and the process is described below.

3.5.1. Alignment and Fine Tune α_1 & β_1 Alignment

The alignment process ensures that the optical axis of the ellipsometric system is defined and the optical components are in their proper respective positions. In order to eliminate any systematic errors due optical imperfections in the components and/or beam deviation, a 180 ° alignment is first carried out without any optical components other than the

light source. The collimated ray is centered in a horizontal axis by using an alignment target with concentric rings, which slides on the rails of the ellipsometer bench. This target is gradually moved from the light source end of the ellipsometer in the light source arm and moved over to the detection arm keeping the collimated ray centered on the target. Once the optical axis is defined, the iris diaphragms are placed in the source and the detection arms, and the aperture is gradually reduced until 0.5 mm opening is set. An auto collimating alignment telescope mounted at the right end of the detection arm (Figure 3.9) is then used as a guide, which replaces the target with concentric rings.

The optic fiber bundle is then centered at the right end of the detection arm and fed to a monochromator set at 400 nm and a photomultiplier tube PMT. A digital spectrum is acquired using an oscilloscope and the optic fiber bundle is considered centered along the optical axis, when the highest intensity (voltage) is achieved. The fiber bundle has to be aligned at the ellipsometer end as well as the monochromator end to achieve the highest intensity.

In the remaining steps of the alignment, the optical components are placed in their respective positions in the ellipsometer bench one at a time and mechanically fine tuning its position to maintain the optical axis defined earlier.

It is recommended that the 180 ° alignment be carried out only once every few months. However, a basic sample stage alignment must be carried out every time the ellipsometer is used. During the sample alignment, the ellipsometer arms are set to 70 ° azimuth angle and a SiO_2 sample of known optical properties and thickness is placed on in

the sample stage. A quick alignment is carried out using the autocollimating telescope before further calibration is carried out digitally.

The control panel of the alignment tab program permits the user to choose the wavelength and the number of rotations to data to collect and average before display. While smaller average improves the speed of data acquisition, a larger variance is found in the spectrum. However, during this process of "course alignment," typically 1-5 rotations is considered an appropriate range for averaging the acquired data. The wavelength choice in the monochromater is typically set at 400 nm (3.12 eV) as it is midpoint of the data spectrum.

When the program starts, it adjusts the monochromator to the desired wavelength setting, minimizes the voltage applied to the PMT, and opens the shutter. The shutter is opened with a 5.0 V TTL signal coming from the NI™ DAC board at DAC1 as shown in Figure 3.9 and 3.13. The programmable power supply is also TTL signal controlled and the 0-5 V applied to the power supply is converted to voltage between 0-1200 V to be applied to the PMT. The photo multiplier tube, as it name suggests, amplifies the photons into electrical signal (current). The voltage applied to PMT is adjusted by a feedback mechanism so that the voltage received at DAC input from the photons entering the PMT is ~ 2.0 V. The voltage received from the PMT has to be constant throughout the spectroscopic range because PMT responds differently the different wavelengths and can vary by upto an order of magnitude in the UV range. Keeping the PMT voltage constant at 2 V insures a uniform electrical signal which can be digitized by the A/D conversion easily. The real time voltage obtained as the feedback mechanism is in progress is displayed in the front panel. This program is also given in Appendix 2.

In the second phase of this program the number of rotation input in the front panel is multiplied by 360 (the number of data points per rotation) to obtain the total number of data points that need to be collected. Upon the trigger of the zero pulse, the data acquisition process is started. The obtained data is re-sorted and averaged into an array and displayed as the spectrum. The sinusoidal waveform obtained from this program is displayed as shown in Figure 3.14a. The symmetry of this displayed wave form is used to align the instrument by manipulating X, Y, and Z controls of the sample stage.

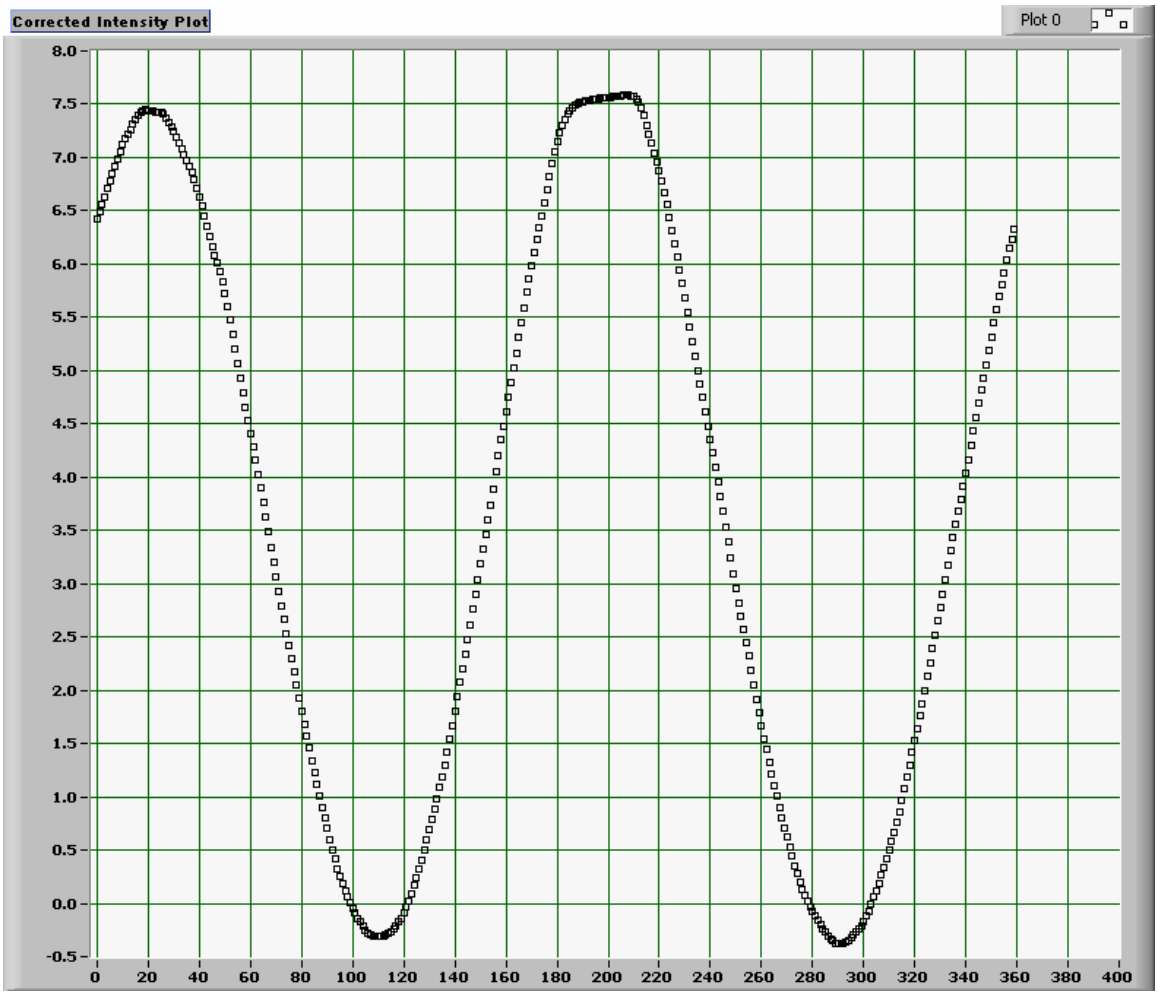

Figure 3.14 (a) Sinusoidal signal obtained from the ellipsometer. The symmetry of this waveform and the intensity of the light is used to align the ellipsometer.

(a)

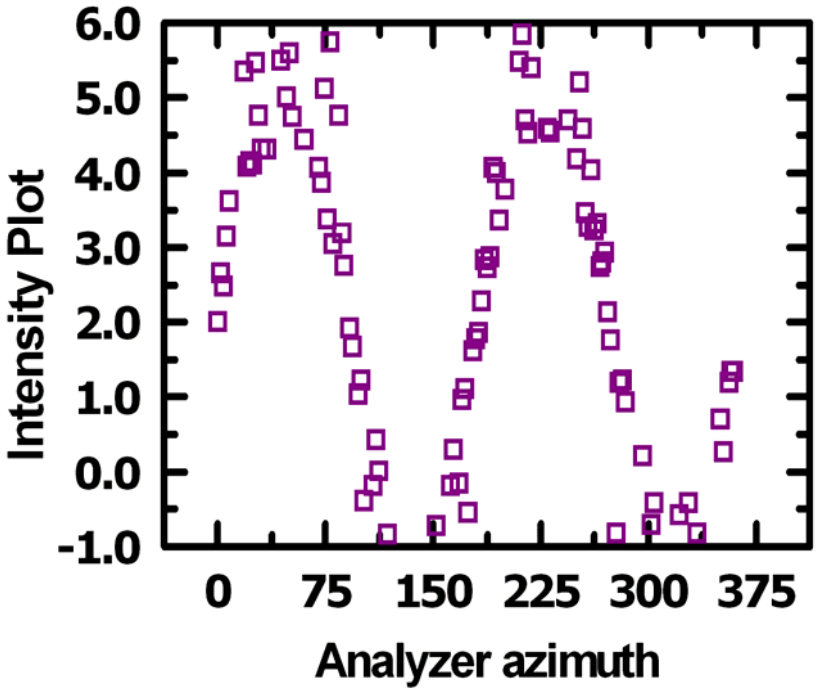

(b)

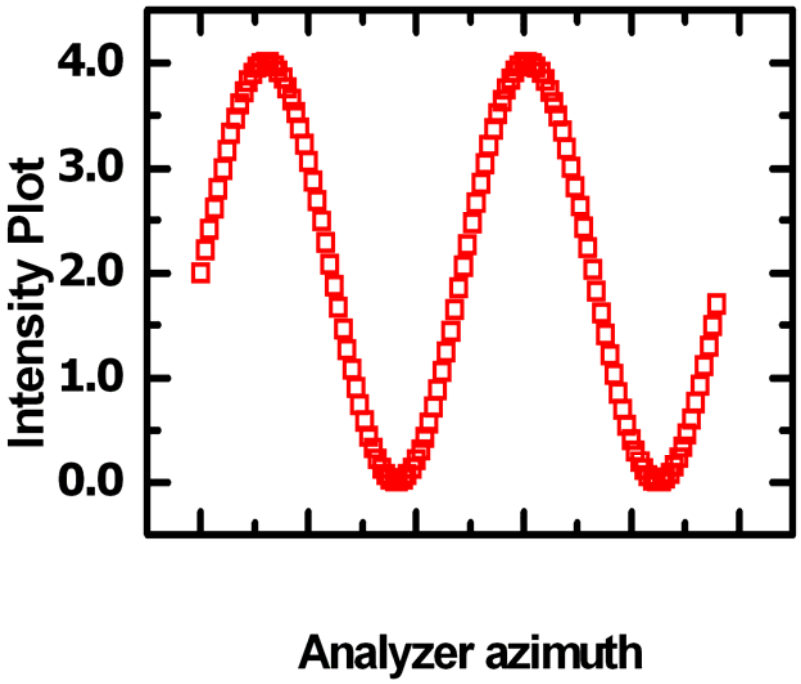

Figure 3.14 (b) a Sinusoidal signal obtained from a poorly aligned ellipsometer (c) the signal improved in symmetry and intensity with better alignment.

Once a coarse alignment is completed, alignment is fine-tuned by minimizing—α_1 & β_1—the first harmonics of the 4 sets of coefficients obtained from Fourier transform of the detected averaged intensity also automated No input parameters are necessary for this step, as the program efficiently extracts the voltage applied to the PMT from alignment, and other offset values are extracted from the alignment and calibration programs directly.

The first set of data is ignored as they have repeatedly turned out to be outliers. Twenty data sets are obtained (20 x 360 = 7200 data points) are collected and averaged. The Fourier transform of this averaged data set yields the four sets of Fourier coefficients of which the first set (α_1 and β_1) are plotted against time axis. While a minimum values for these coefficients are desirable, any value below 0.01 is considered a respectable alignment and the instrument is ready for use.

Figure 3.15 shows the plot of α_1 & β_1 obtained during fine alignment where $|\alpha_1|$ and $|\beta_1| < 0.01$. It is important to calibrate the instrument before first use. The calibration process corrects any offsets in polarizer value P_{off}, analyzer azimuth value A_{off}, and phase change during the filtering process η. In addition, an SiO_2 calibration wafer with a known SiO_2 thickness is used to verify the calibration process by acquiring and analyzing its SE data. The η factor has been discussed briefly in this section but will be discussed further in the calibration section.

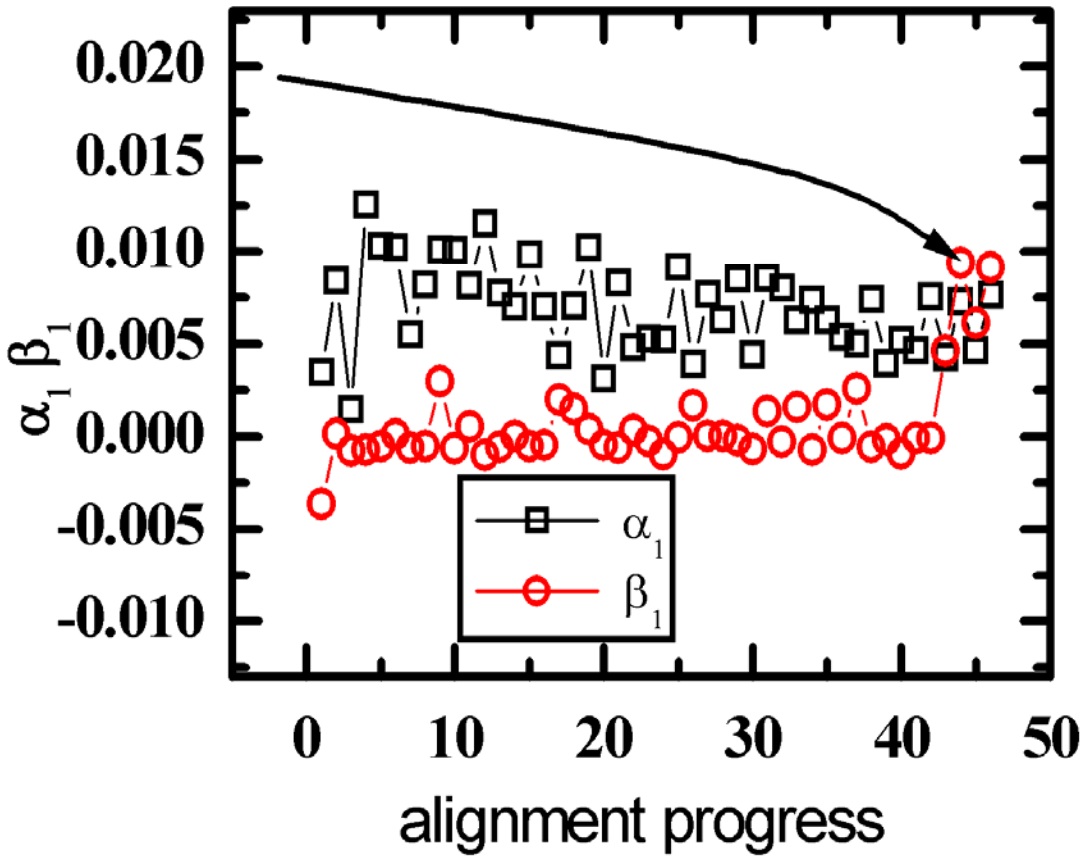

Figure 3.15. α1 and β1 obtained during the alignment process. A system is aligned when the Fourier Coefficients are minimized within the range of +/- 0.01.

3.5.2. Spectroscopic Ellipsometry

The spectroscopic ellipsometry control panel is shown in Appendix A. The input parameters are divided between two parts—primary and secondary. The primary parameters are revised more frequently and are tailored to individual spectra analysis. The starting wavelength, ending wavelength, wavelength step, ellipsometry azimuth angle, and experimental comments are input by the user. The secondary parameters consist of P_{off}, A_{off}, η, and polarizer angle. The polarizer angle is set to 20° for most of the experiments and the

calculations of the other parameters obtained during calibration will be discussed in Section 3.5.3.

When the SE program starts, for every wavelength in the desired range, one set of data is taken with the shutter open and a second set is taken with the shutter closed to subtract the intensity effect from stray and ambient light sources. The second harmonics of the Fourier transform obtained from the corrected signal is then used in Equations 3.19 and 3.20 to extract the ellipsometric parameters Ψ and Δ. The program loops until the final wavelength reaches. The Ψ and Δ extracted during each loop is arranged in an array and saved in a file specified by the user.

3.5.2.1. Importance of Shutter Control

As introduced in Section 3.5, the shutter subtracts light intensity and dark current due to stray light. Dark current shifts the background level and alters the actual signal associated to the light reflected from the sample carries the optical information about the sample. The dark current is a bi-product of voltage applied to PMT, which has be adjusted to maintain constant average current measurement throughout the spectrum. The magnitude of this change in background voltage can be as high as 2 orders of magnitude in the operation range of 600 V to 1200 V. Since the measurement is made in the total average intensity detected by the PMT, the background reduces the actual signal significantly. Therefore, the intensity of the detected signal is measured at each wavelength once with the shutter open and the second time with the shutter closed to subtract out the parasitic effect of stray light and dark current in PMT from the total intensity coming out of PMT.

The five blade shutter, which as mentioned earlier is controlled by a TTL signal, has its aperture size set to 1.6 mm. Due to its 10 ms mechanical delay, the SE program has a built in delay of 100 ms after any shutter operation. This procedure ensures the proper status of the shutter at any given time.

3.5.3. Calibration

The calibration process is required for all instruments to eliminate any inaccuracy of the scale readings of the optical components placed in the ellipsometer. The calibration process has also been automated and can be performed with relative ease by extracting ($\alpha 2$ and $\beta 2$) between -7 ° to +7 ° (polarizer angle) around the P = 0°. The equations mentioned in this section are incorporated in the calibration LabVIEW™ program thus the P_{off}, A_{off}, and η can be extracted as described below.

All optical components must be referenced in the plane of incidence (POI) defined as the 0° for the system. POI is defined as the plane containing the incident ray, the reflected ray, and the optical axis normal to the sample. The calibration process determines the offset in the polarizer and the analyzer, and adjusts the reading in order to produce the correct azimuth orientation with respect to the POI.

$$\begin{aligned} P' &= P - P_{off} \\ A' &= A - A_{off} \end{aligned} \tag{3.21}$$

In Equation 3.21, P' is the new corrected polarizer angle, P_{off} is the offset and P is the reading on the rotator mount. In addition to the offsets in the polarizer and the analyzer, when the intensity of photons received by the PMT is converted and filtered through the

electronic circuit, a frequency dependent gain and a phase shift occurs which is corrected by a correction factor, eta, η.

While a variety of calibration procedures is reported in the literature, the small angle method and more specifically the residual function calibration is used and described here.[1] In this method, specific functions of measured Fourier coefficients (α_2 and β_2) at a given wavelength (typically 400 nm) are plotted against a small angular reading of polarizer around 0°. For a rotating analyzer experiment, sin (P-P_{off}) and cos (P-P_{off}) are applied so that the resulting functions can be fit in quadratic and linear forms to obtain A_{off}, and P_{off} and η. The first step of the calibration procedure involves the calculation of the POI for which the polarizer offset P_{off} is calculated from the raw Fourier coefficients. Once the P_{off} is determined, A_{off} and η can be obtained as described below.

The residual method is based on the fact that the light beam is linearly polarized only along either of its orthogonal axes (p or s directions), then the light reflecting from an isotropic sample must also be linearly polarized. In all other cases, the reflected light beam is elliptically polarized (section Therefore, in the absence of other errors, the experimentally determined modulation $\alpha^2 + \beta^2$ should have its highest value (1) when $P' = 0$ or $P + \pi/2$ radians i.e. P' along p- or s- directions. Therefore, the residual function R(P) is defined as the amplitude function's deviation from the its maximum as described in Equation 3.22.

$$R(P) = 1 - (\alpha'^2 - \beta'^2) = 1 - \frac{(\alpha^2 - \beta^2)}{\eta^2} \tag{3.22}$$

Once the Fourier coefficients are determined at a fixed wavelength (here 400 nm) and plotted for different values of P around P_{off} or $P_{off}+\pi/2$, the minimum in experimental

residual function can be determined. The value of *P* where the best fit line of the quadratic function is the minimum is *P'* as shown in Figure 3.16.

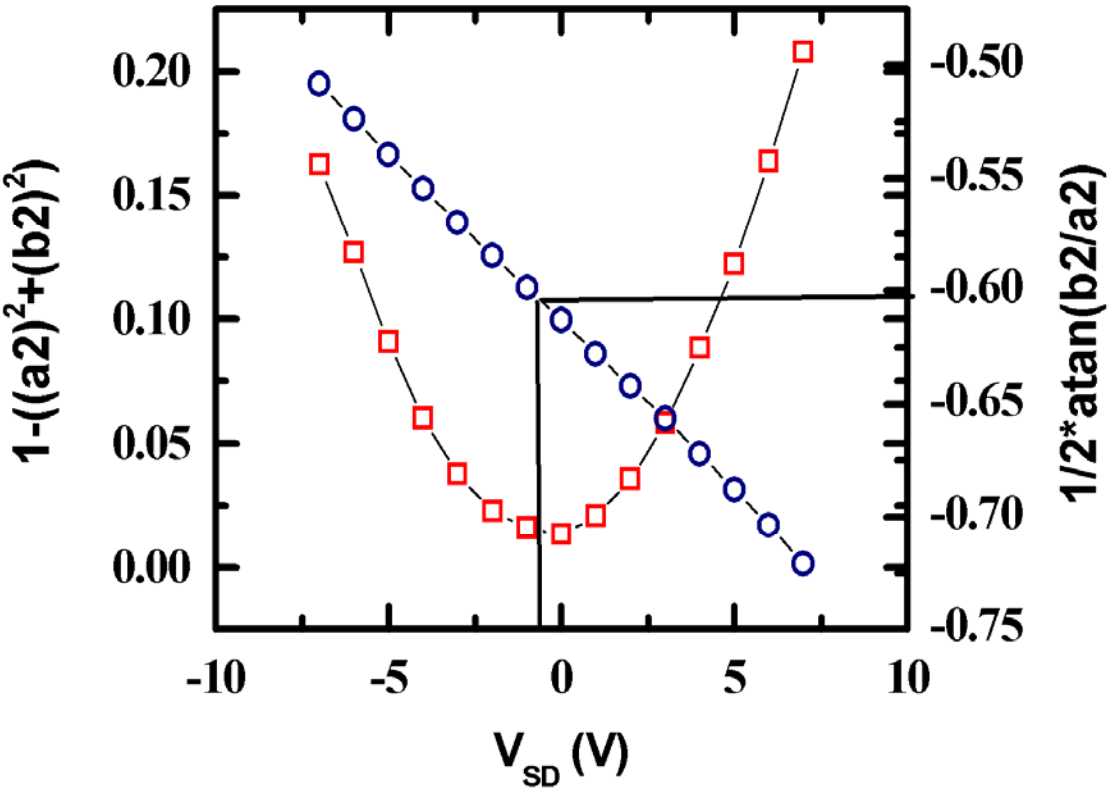

Figure 3.16. Calibration of ellipsomter to obtain Polarizer offset, analyzer offset and offset due to electronic filtering, η.

Once P is determined and the respective R calculated, η can then be determined by Equation 3.23.

$$\eta = \frac{1}{\sqrt{1 - R_{\min}}} \tag{3.23}$$

The phase function for the rotating analyzer is determined by the following Equation.

$$\Theta(P) = \frac{\tan^{-1}\left(\beta / a\right)}{2} \tag{3.24}$$

When Experimental Fourier coefficients (α and β) are substituted in Equation 3.24 and plotted against the same values of P used in Equation (3.22), a linear function is observed as shown in Figure 3.16. The y coordinate (position of the polarizer) where *P* is minimum in the linear function thus becomes the offset in analyzer, A_s. A value of π/2 is added to A_{off} when the *atan* function is used if the values of (α and β) are negative.

As the values of η and A_{off} are both dependent on P_{off}, the standard deviation of azimuth of *P* has been calculated by Equation 3.25.

$$\sigma_P^2 = \left(\frac{1}{2D_2}\sigma_1\right)^2 + \left(\frac{D_1}{2D_2^2}\sigma_2\right)^2 \tag{3.25}$$

Here the D_1 and D_2 are the coefficients of the parabolic equation of the best fit quadratic equation in Figure 3.16 and σ_1 and σ_2 are the associated errors. And σ_P decreases with the increasing curvature (i.e. increasing D_2). Once the calibration is completed, the ellipsometry automation program is ready for data collection (Ψ and Δ). Optical modeling of

the data using ellipsometric software for regression analysis can then be used to extract the optical properties of the material or film under investigation.

3.6. Optical modeling

Ψ and Δ are functions of the optical properties and thickness of a material but Ψ and Δ do not measure these properties directly. Therefore the optical properties and the film thickness must be extracted from the Ψ and Δ using an optical model based on different physical relationships described in Section 3.3. Commercial software (WVASE™ J. A. Woollam) is used to analyze the spectral data and fit it with a model that is developed from a variety of results. A strategy to develop the optical model is given in Figure 3.17. The process starts with the construction of a model with a correct stack of films in the correct order along with their optical characteristics and film thickness as shown in Figure 3.18. Complimentary techniques such as AFM and UV-vis spectroscopy can also be used to obtain some of the pertinent information of the material under investigation. When values are not known for a parameter in the model, an educated guess is made.

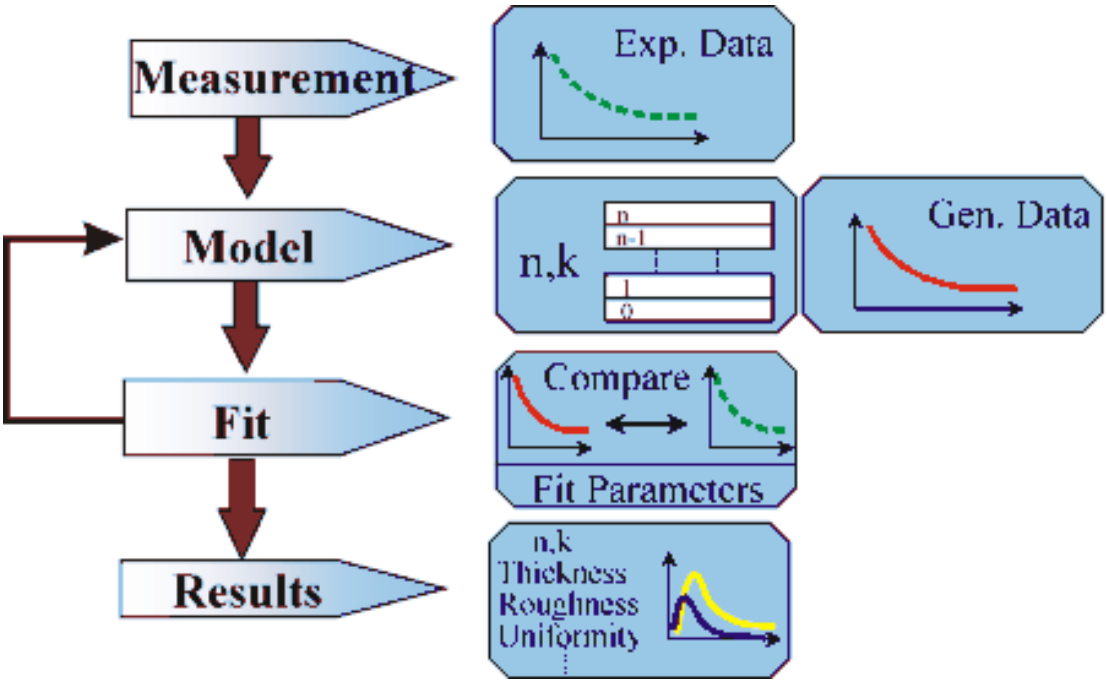

Figure 3.17. Strategy used to extract the optical information from Ψ and Δ by developing an optical model for the system under investigation.

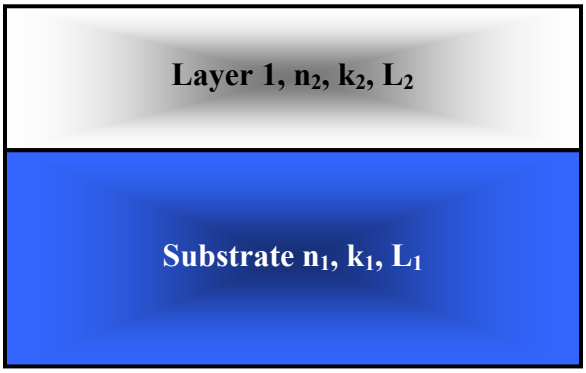

Figure 3.18. Initial assumption of sharp interface made about the film on a substrate. Known optical properties are input into the model.

A simple model with sharp interfaces between the layers, and no optical anisotropy is first assumed at the beginning of the model (Fig. 3.18). Complexity is added as more information about the material is known. Once the preliminary model is complete, a set of data is generated based on the optical properties and the thickness information available and it is compared with the experimental data. Gradually various parameters that influence the optical properties of the material are varied iteratively so that errors between the generated data and experimental data are minimized. Mean squared Error (MSE) technique is used to quantify the difference between experimental and generated data with smallest MSE value implying the best possible fit.

$$MSE = \frac{1}{2N - M} \sum_{i=1}^{N} \left[\left(\frac{\Psi_i^{\text{mod}} - \Psi_i^{\text{exp}}}{\sigma_{\Psi i}^{\text{exp}}} \right)^2 + \left(\frac{\Delta_i^{\text{mod}} - \Delta_i^{\text{exp}}}{\sigma_{\Delta i}^{\text{exp}}} \right)^2 \right] \tag{3.26}$$

where N is the number of Ψ and Δ pairs used, and M is the number of parameters varied in the regression analysis, while σ is the standard deviation of the experimental data points.

It should be noted that the results obtained from modeling are dependent on the accuracy of the assumptions about the physical properties of the material. Therefore once an initial fit between the experimental and generated data sets is obtained, the resulting fit parameters are evaluated for sensitivity and possible correlation between the parameters. The model is then tested to see if the MSE value can be further lowered and the 90% confidence interval minimized by increasing the complexity of the model such as a roughness layer and anisotropy of the film. The resultant parameters are tested for their "realness." e.g. a negative thickness would instantly flag the inaccuracy of the assumption in the model. Likewise, the n must decrease with increasing λ if k = 0.

Details of the models used in our approach to understand the optical properties of POMA are discussed in Chapter 4.

3.7. References

1. Tompkins, H. G., Irene, E. A., Handbook of Ellipsometry. In Norwich NY; William Andrew Pub.; Heidelberg Germany; Springer: 2005.

2. Irene, E. A.; Goncalves, D., Fundamentals and applications of spectroscopic ellipsometry (vol 25, pg 794, 2002). *Quimica Nova* **2002,** 25, (6A), 1050-1050.

CHAPTER 4 - OPTICAL and MORPHOLOGICAL CHARACTERIZATION of POLY(*o*-METHOXYANILINE)

4.1. Overview

The poly(*o*-methoxyaniline) as shown in Figure 4.1 has been introduced in earlier chapters. A primary advantage of using POMA over its more widely investigated parent compound, polyaniline is the presence of the *o*-methoxy group in the emeraldine base form of POMA. This methoxy group increases its solubility in various organic solvents compared to that of PANI, while maintaining similar optical and electronic properties.[2] Solubility facilitates the doping process in organic polymers and enables the fabrication of devices such as organic thin film transistors (OTFT) and organic light emitting diodes (OLED).

The solid state optical properties are required to aid the fabrication of devices and to understand the electronic and optical nature of these organic materials. It has been found that the optical properties of a solid are usually different from those of a solution.[3, 4] In this study, we report the optical properties of spin-coated POMA films in the UV-Visible light range (1.5-4.5 eV) as obtained using spectroscopic ellipsometry (SE). The refractive index (n), and the extinction coefficient (k) were obtained from regression analysis using an optical model developed in this study along with experimental results and optical anisotropy results are also

reported. A combination of rotating analyzer spectroscopic ellipsometry (RAE), ultraviolet-visible (UV-Vis) spectroscopy, and Atomic Force Microscopy (AFM) was used to collect data.

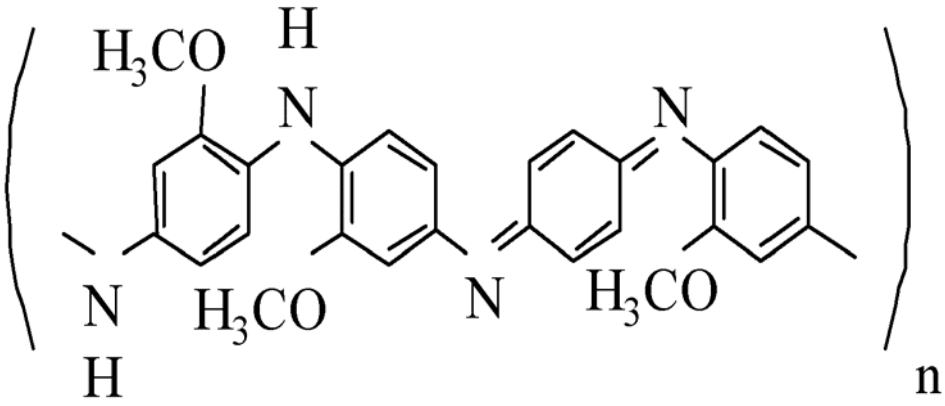

Figure 4.1. Molecular structure of POMA

4.2. Experimental Procedure

Before film deposition Si, (single crystal, p-type, <100> orientation) substrate wafers were cleaned using the RCA procedure.[5] A "sacrificial" oxide layer was grown before the Si wafer was cut to a desired size (~2 cm^2) using a diamond scribe. The cut wafers were dipped in 48 wt % HF, and rinsed in de-ionized water to remove any trace of SiO_2 or Si particles on the substrate surface resulting from the wafer cleaving process. Subsequently the wafers were placed in oxidation furnace to grow about 20 nm of SiO_2. For UV-Vis data acquisition, pyrex and fused silica slides were used as transparent substrates for the POMA films. The surfaces of these substrates were also prepared using RCA cleaning procedure, but without the HF dip step.

The POMA used in this study was obtained commercially from Alfa Aesar. A fresh solution for spin coating was prepared by dissolving POMA in chloroform. The mixture was stirred for 2 hrs at room temperature and pressure in a closed container, and the resulting dark blue solution was vacuum filtered using a 1 μm filter.

Solution concentrations in the range 0.5- 2.0 wt % were spin-coated at 500-9000 RPM onto Si, SiO_2, and glass slide surfaces. A micropipette was used to dispense 10 μL of POMA solution on to the spinning substrate surface at close proximity, and the substrate was allowed to spin for about 2 min in N_2 ambient.

The UV-Vis spectrum of a 0.05 wt % POMA solution in chloroform in a quartz cuvette, and the spectra of POMA film spin-coated onto fused silica were taken using a LAMBDA 950 Spectrophotometer.

A custom built variable angle rotating analyzer spectroscopic ellipsometer and a JA Woollam Co. model M88 spectroscopic ellipsometer were used for data collection. Both of these instruments have a spectral range of about 1.5-4.5 eV, and the measurements were made at 5 meV intervals. Twenty data sets were averaged per wavelength to improve signal to noise ratio, and 4 incident angles were used. The criteria for the selection of these angles are discussed below.

Ellipsometry measures the change in the state of the polarization of the light reflected from the sample.[6] A detailed introduction of ellipsometry is given in Chapter 3. The measurables in this technique, Δ and Ψ, are related to ρ the complex reflection coefficient and to the Fresnel coefficients $\tilde{R}_p$ and $\tilde{R}_s$ by the formula:[7]

$$\rho = \tilde{R}_p / \tilde{R}_s = \tan(\Psi) e^{i\Delta} \tag{4.1}$$

Likewise, the dielectric response function ε, and pseudo dielectric function $\langle\varepsilon\rangle$, a composite dielectric function of a multi-film stack upon a substrate are both obtained from the formula:

$$\varepsilon \text{ or } \langle\varepsilon\rangle = \varepsilon_1 + i\varepsilon_2 = \sin^2\phi \tan^2\phi \left(\frac{1-\rho}{1+\rho}\right)^2 \tag{4.2}$$

The parameterization of the optical dielectric function, ε is based on the fact that ε is related to band-to-band transitions that could be expressed by different oscillators. However, it should be pointed out that there is no simple correlation between the energies of optical transitions and oscillator resonance energies in the oscillator model that will be described below.[8] Consistent with the broad absorption observed in the UV-Vis spectra of POMA

films, Lorentzian oscillators were used to describe POMA's optical properties (ε_1 and ε_2 and n and k).[8] The quality of the fit of the data to the model is assessed by the mean square error (MSE) defined as follows: [9]

$$MSE = \frac{1}{2N - M} \sum_{i=1}^{N} \left[\left(\frac{\Psi_i^{\text{mod}} - \Psi_i^{\text{exp}}}{\sigma_{\Psi i}^{\text{exp}}} \right)^2 + \left(\frac{\Delta_i^{\text{mod}} - \Delta_i^{\text{exp}}}{\sigma_{\Delta i}^{\text{exp}}} \right)^2 \right] \tag{5.3}$$

A MSE value of 0 indicates a perfect correspondence of measured and model calculated results. Another important factor that impacts the fit is the correlation among the parameters. In order to minimize correlation, multiple samples were used and several other techniques such as AFM and UV-Vis spectroscopy, and were used to provide complementary support to the models used. AFM images were obtained in tapping mode using the Multimode IIIa Atomic Force Microscope and reported for an area of 1 x 1 μm^2. (For the dynamic operating mode of AFM, the drive frequency was 172.3 KHz, scan speed 10 μm/s, scan size was 2x2 or 1x1μm^2, sampling rate was 1 Hz. The tip (model NSC14/noAl) was purchased from Ultrasharp with a resonant oscillation frequency of 160 KHz).

All POMA films and the polymer solutions were stored in nitrogen ambient between measurements and solution preparation. No significant change in optical properties was observed for the films over period 1-2 month periods.

4.3. Results and Discussion

4.3.1. Film Deposition

Besides the fact that the concentration of the POMA solution and the speed can affect the film thickness, the interactions among the polymer, solvent and the substrates (Si and SiO_2) during film deposition can also affect the adsorption of POMA, anisotropy, and thickness. As shown in Table 4.1, a significant difference in the POMA film thickness was found depending on the substrate being either bare Si or SiO_2 where the spin casting conditions were otherwise the same (RPM and concentration).

Wt% POMA in CH_3Cl	**Spin speeds (RPM)**	**Substrate**	**POMA Thickness nm)**
2%	9000	SiO_2	69.0±8.0
2%	9000	Si	43.2±4.2
2%	4500	SiO_2	170.7±8.0
2%	4500	Si	120.8±11.0
0.5%	3000	SiO_2	46.0±2.9
0.5%	3000	Si	37.0±4.0
0.5%	1000	SiO_2	5.6±20.0
0.5%	1000	Si	15.0±16.0

Table 4.1. Concentration, spin speed, and POMA film thickness for Si and SiO_2 substrates.

The reason for thicker films on the SiO_2 substrate likely lies with the difference in surface energy of the substrates. The surface energy for freshly HF dipped Si (hydrogen terminated) is significantly smaller than that of SiO_2 as shown in Table 4.2.[10] Therefore the POMA solution wets the H-terminated Si surface far less than the SiO_2 surface. Considering

that for spin casting, only a single drop (10 μL) of POMA solution was dispensed at the center of the spinning wafer (2 cm^2 area), the polymer-substrate interaction dictates the amount of solution that adheres to the substrate surface and therefore determines the film thickness. The thickness value of SiO_2 does not have to be large, even a thin native oxide (~1 nm), that grows in air after the HF dip increases the POMA-surface energy (hydrophilicity) and permits wetting and thicker polymer films.

Substrate	**Surface Energy (dynes/cm^2)**	**Surface Energy (Pascal)**
Si	1100	110
SiO_2	2000	200
Si H-terminated	27	2.7

Table 4.2. Comparison of surface energies for Si, SiO_2, and H-terminated Si.

Another factor that influences the film thickness and its uniformity is the evaporation of the solution during spinning.[11, 12] As the solution dries during spin casting, the concentration and viscosity of the solution increases leaving thicker films near the edges of the substrate. Therefore, the films prepared at the slowest spin speeds (lower than 1000 RPM), sometimes contained polymer agglomerates and bare areas which resulted in large standard deviations as seen in Table 4.1. In the present study, we found that increasing spinning speed to 3000-5000 RPM helped achieve more uniform film thickness.

4.3.2. Optical Characterization

The thickness measurements presented in Table 4.1 and the optical properties determined in this study were obtained using spectroscopic ellipsometry (SE). SE requires formulation of an optical model that is used to extract the thickness and optical information from the ellipsometric measurables, Ψ and Δ by means of regression analysis. In order to develop this model, a simple film on substrate model with sharp interfaces and no roughness was initially assumed and shown in Figure 4.2 with a POMA film on a Si substrate.

A Cauchy formula for n shown below was used to analyze the SE data at the lower energies (1.96-2.48 eV) where the thin POMA film is transparent (i.e. k is negligible).[9]

$$n(\lambda) = A + \frac{B}{\lambda^2} + \frac{C}{\lambda^3} \tag{4.4}$$

In the Cauchy formula, λ is the wavelength and A, B, and C are parameters that are fit in the analysis. The experimental data, model fit to the data, and the fitted parameters (inset) obtained from Cauchy model are given in Figure 4.3. This model, when used in the appropriate wavelength range, minimizes the number of variables and enables a more accurate determination of the film thickness that can be used (below) in a more complete optical model that covers the entire SE optical range. In addition, complimentary data was acquired using AFM to approximate the film thickness.

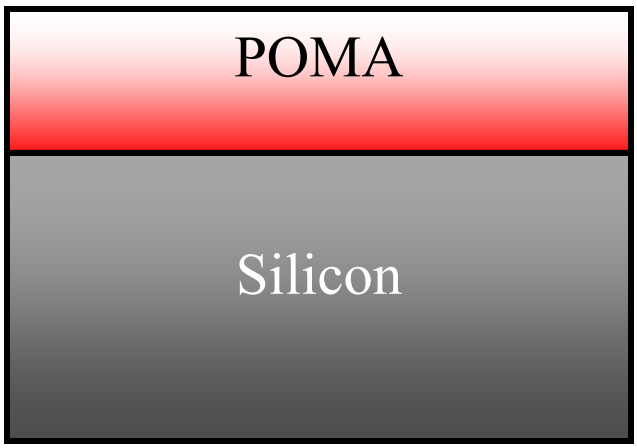

Figure 4.2. Single POMA film on Si substrate model with sharp interface and no roughness

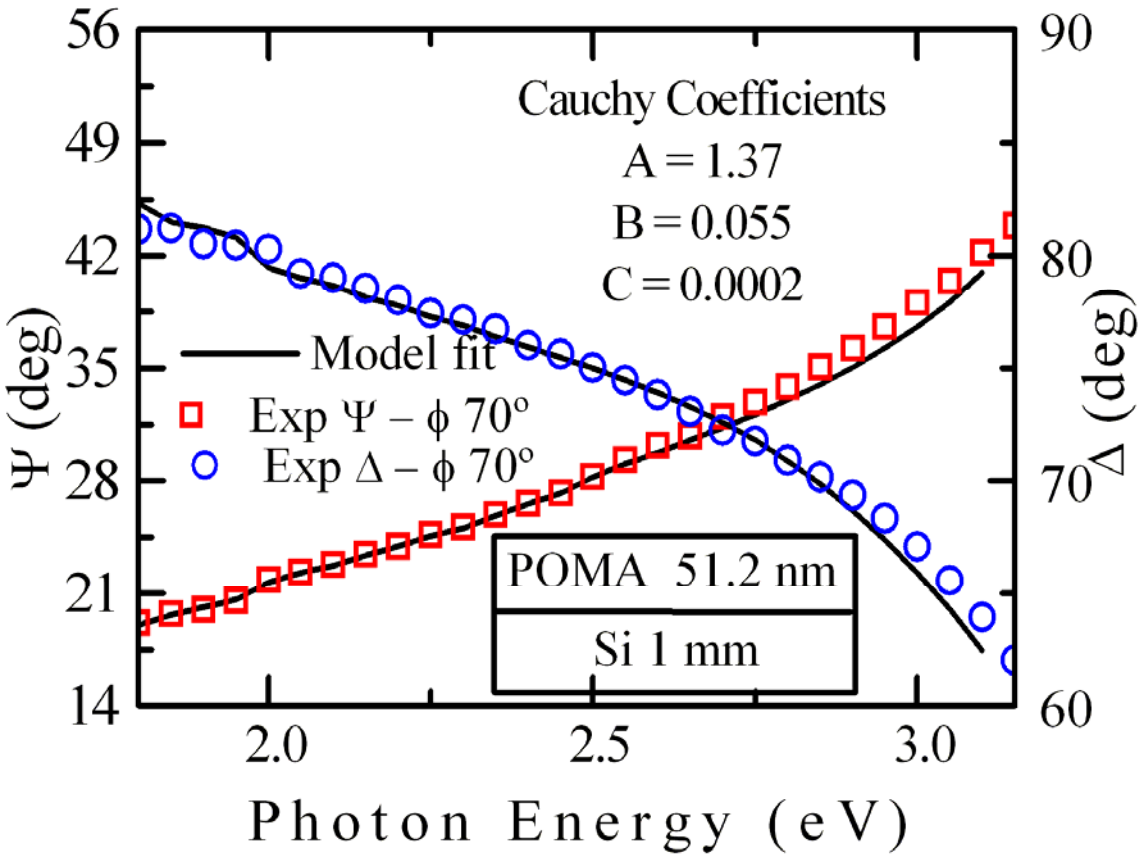

Figure 4.3. Single film optical model (shown) with fits to the Cauchy formula for lower photon energies. The fitted Cauchy parameters are in the inset.

The use of the Cauchy model was initially used with the assumption that thin films (less than 55 nm) displays nearly zero total absorption. From Figure 4.3, it is apparent that the Cauchy model fits well for low energies but not very well where there is higher absorbance at photon energies above 2.5 eV. However, this simple model was useful in extracting a good value for the film thickness that in turn is used for the more complete analysis over a broader spectral range and with the thickness as an input value reduces correlation among the variables.

In order to improve on the Cauchy model, UV-Vis optical transmission study was carried out to obtain the absorbance of POMA. A UV-Vis spectra of POMA solution (similar to that of PANI) shows a strong absorbance in the uv-region of the spectrum.[13] However, the spectrum obtained in solution differs from that of the solid film because of different distributions of polymer strands in solution and in film. Therefore, the optical absorption in the UV-Vis range of solid POMA film was independently determined and incorporated in the more complete optical model. Figure 4.4 shows the absorption spectrum determined for solid POMA films with broad absorption bands at 1.8-2.1 eV, 3.9-4.3 eV and 6.1 eV. Similar spectral features are also exhibited by PANI thin films.[14]

Thus a Lorentz oscillator model was used in order to incorporate the UV-Vis absorbance data in the optical model for POMA, and to extend the ellipsometric model in higher energies, which permits inclusion of the physics of the interaction of the conjugated double bonds in the polymer backbone with the polarized light. The Lorentz osciallator model has been successfully used in the optical region where the fundamental band gap is observed and has the form shown in Equation 5.5.[9, 15, 16]

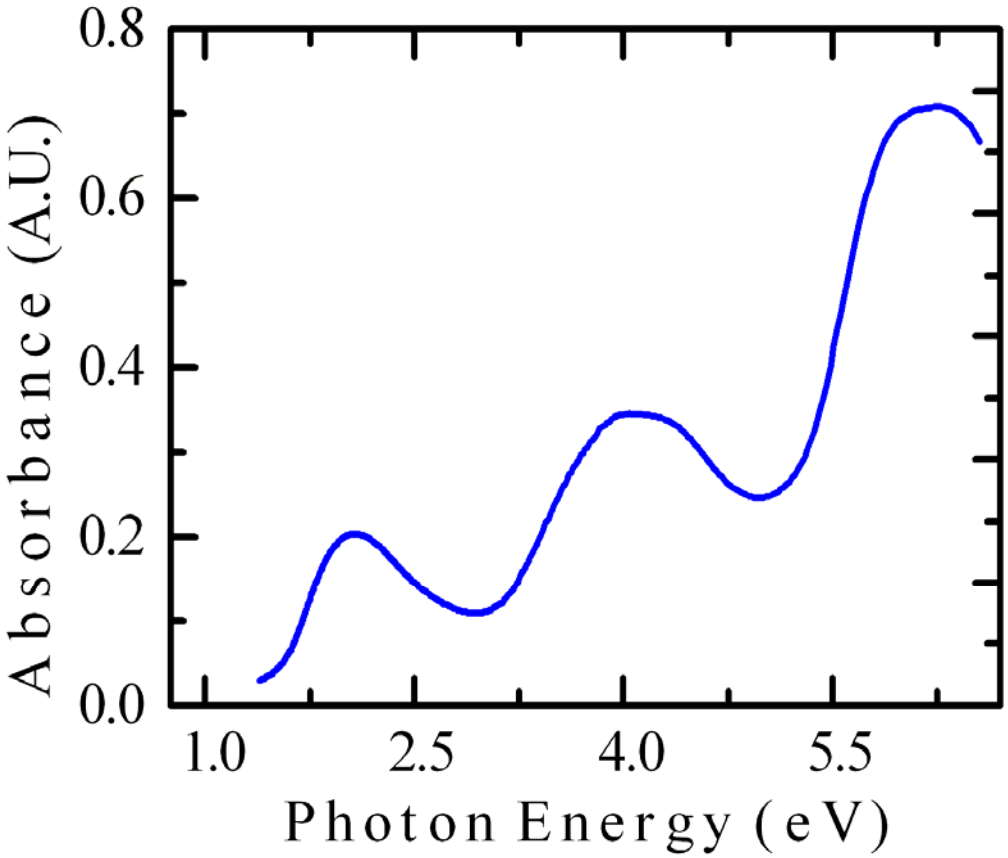

Figure 4.4. The absorption spectra of a POMA film deposited by spin coating on a fused silica slide.

$$\varepsilon(E) = \varepsilon_1(\infty) + \sum_{i-1}^{N} \frac{A_i E_i}{E_i^2 - E^2 - iB_i E} \tag{4.5}$$

$\varepsilon(E)$ is the dimensionless complex dielectric function, $\varepsilon_1(\infty)$ is the real part of the dielectric function at infinite energy, and N is the number of oscillators used in the model. Each oscillator is described by three parameters (with units of eV): A_i is the amplitude of the oscillator, B_i is the broadening parameter of each oscillator and E_i is the center energy location. For the ellipsometric model in this study, 3 oscillators were used that correspond to the main absorption peaks in the UV-Vis spectrum. The A_i, B_i, and E_i parameters were extracted from the model and are presented in Table 4.3.

	A_i (eV)	**E_i (eV)**	**B_i (eV)**
Lorentz Oscillator #1	1.48	1.92	0.698
Lorentz Oscillator #2	1.24	4.00	1.24
Lorentz Oscillator #3	22.3	6.3	0.222

Table 4.3. Lorentz oscillator parameters for POMA.

The model shown in the inset of Figure 4.5 was used to analyze a range of POMA films with different thicknesses and the fit of the data to the model is also shown in Figure 4.5. The resulting optical properties of POMA in terms of n and k extracted from the regression analysis are shown in Figure 4.6.

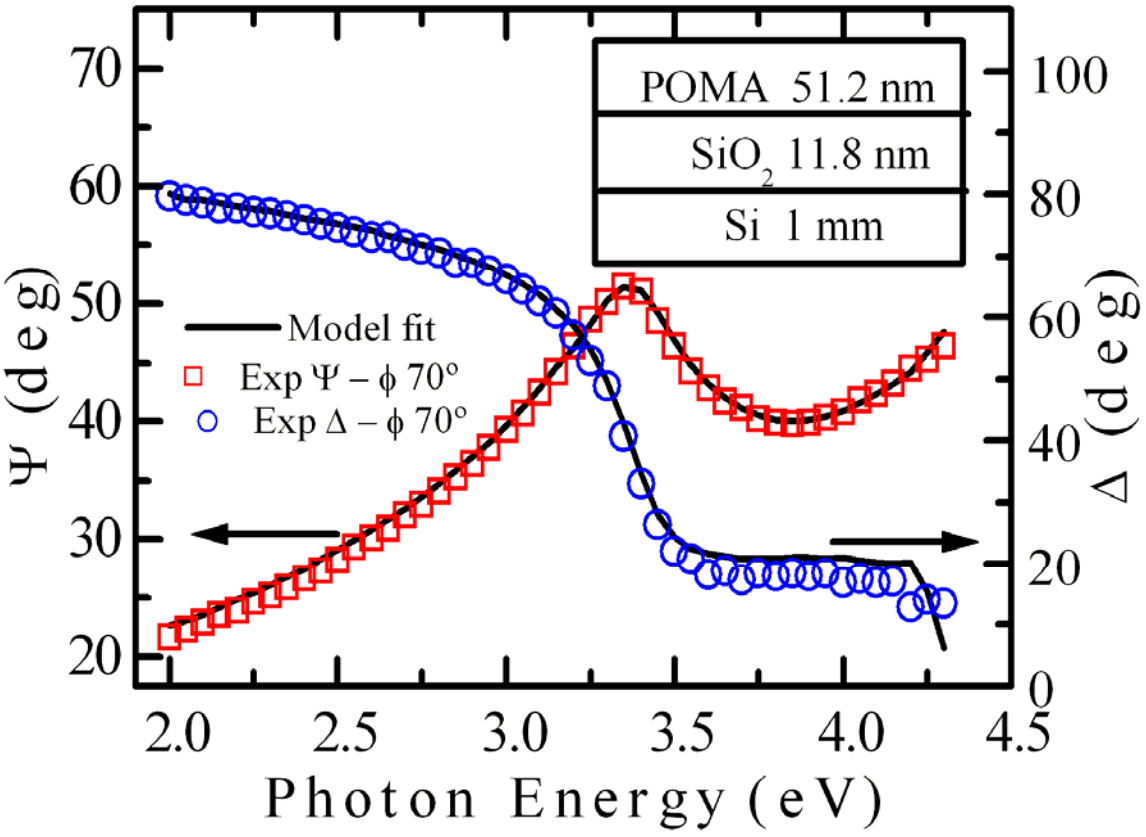

Figure 4.5. Experimental data with fit to the Lorentz oscillator model for POMA on SiO_2.

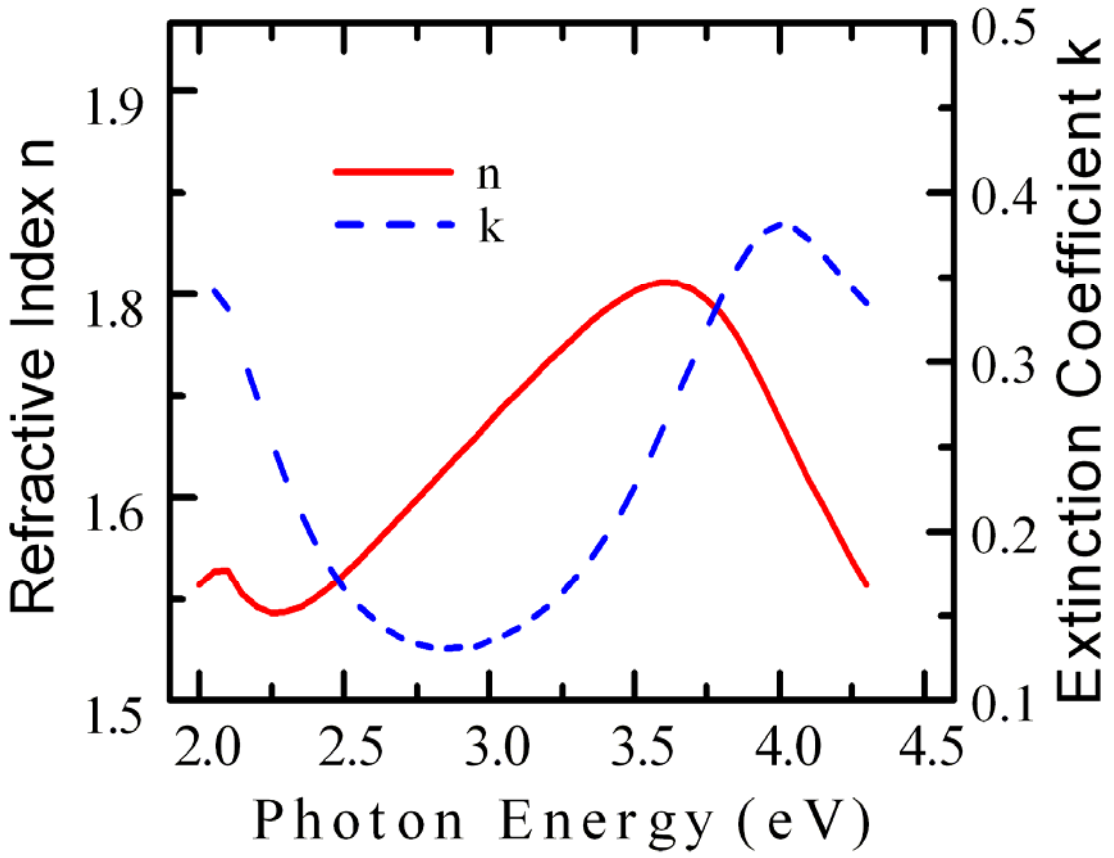

Figure 4.6. Optical constants of POMA—the refractive index (n) and extinction coefficient (k) obtained from the isotropic Lorentz oscillator model.

This spectrum of optical properties n and k has similar features to the spectrum of PANI [13]. MSE values were 25 for 50 nm thick POMA film sample and 40 for 120 nm sample. The model so far does not consider possible optical anisotropy, which is discussed in the following section.

4.3.3. Optical Anisotropy

When polymer chains align in a preferred orientation on a substrate, optical anisotropy can result as is illustrated in Figure 4.7 where polymer chains lie in the plane of the film, and the spin coating process can lead to anisotropy.[8, 9, 17] Typically out-of-plane uniaxial anisotropy has been reported for spin cast polymers indicating that the chains lie disordered in the plane of the film. The nomenclature used in this study is $n_{\|}$ and $k_{\|}$ and $n_{\perp}$ and $k_{\perp}$ to indicate the optical properties for the probing light traveling parallel or perpendicular to the optic axis. Often "ordinary ray" n_o and "extraordinary ray" n_e is found in the literature and using this nomenclature $n_{\|} = n_o$ and $n_{\perp} = n_e$.

In order to investigate in-plane anisotropy in our spin-cast POMA films, ellipsometric measurements were obtained at different azimuth angles in-plane—90°, 180°, and 270° with the angle of incidence $\phi = 70^{o}$. The resulting spectra for $\langle\varepsilon_1\rangle$ and $\langle\varepsilon_2\rangle$ were found to be identical within error limits as shown in Figure 4.8.

These results indicate no detectable in-plane anisotropy for our spin cast POMA films. In order to determine if any out of plane or uniaxial anisotropy exists, SE was performed at multiple angles of incidence (ϕ) from 55°-70° in 5° intervals.[18] The choice of

these angles was made using calculated Δ-Ψ trajectories at various photon energies between 1.96 and 4.13 eV.

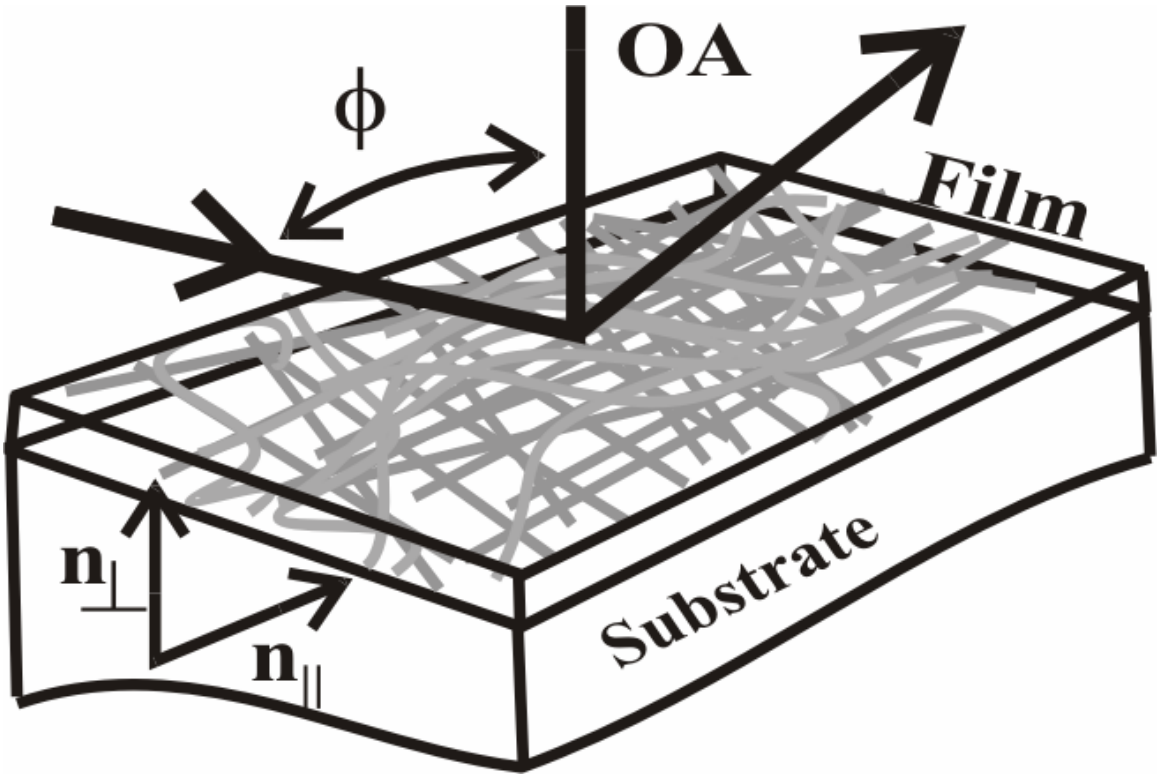

Figure 4.7. Polymer film coated substrate with chains in the film plane with the optical axis OA and angle of incidence ϕ. $n_{\parallel}$ and $n_{\perp}$ are the anisotropic refractive indices.

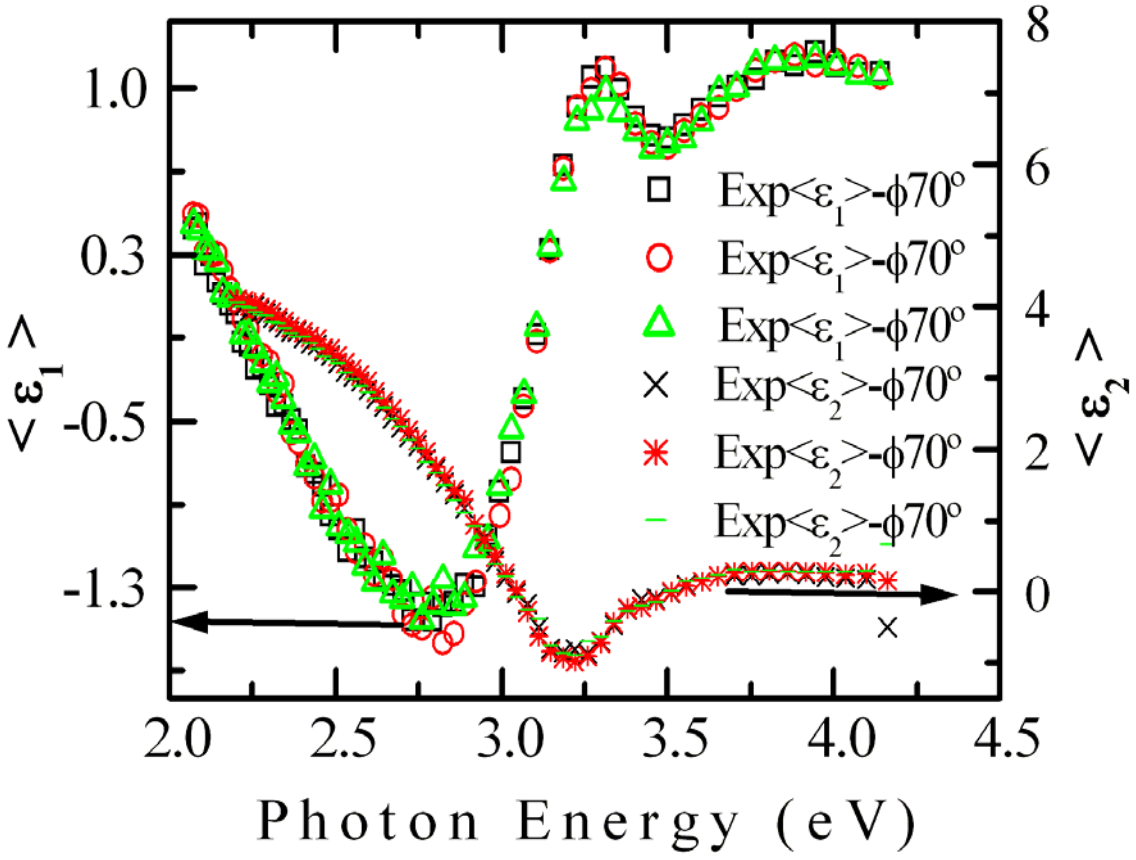

Figure 4.8. Pseudo dielectric constants $< \varepsilon_1 >$ and $<\varepsilon_2>$ for 50 nm POMA film on Si taken at different azimuth in-plane angles—90°, 180° and 270°

Figure 4.9 shows calculated Δ-Ψ trajectories for 2.48 eV light with ϕ values from 55 ^{o} – 70 ^{o} and with POMA thicknesses from 1-150 nm at 4 nm intervals. The change in Δ and Ψ indicate that the most sensitive ϕ values were 60 ^{o} – 70 ^{o} which were therefore selected for use in this study.

The extracted n and k spectra of POMA at various angles are shown in figures 4.10a and b respectively. While no large differences in n and k were observed, a small systematic trend in n was seen. Thus a uniaxial model (available in WVASE software) was used to model the anisotropy. Two Lorentzian oscillator layers called dummy layers with the same oscillators obtained in the isotropic model but with thicknesses set to zero were included below the uniaxial layer. These dummy layers were used to extract the optical constants for the parallel and perpendicular components of the optical properties of POMA, since they can be varied independently. A uniaxial layer for the film, which uses these two sets of optical properties were used simultaneously to calculate a fit with the experimental data and the resulting thickness of the film.

Figure 4.11 shows $<\varepsilon_1>$ and $<\varepsilon_2>$ data together with the best-fit simulated curve for POMA. The MSE for a 50 nm film value improved from 25 to 15 using the anisotropic model and the 120 nm sample also saw improvement in fit from 40 to 30.

From this anisotropic model, the values for $n_{\|}$, $k_{\|}$ and $n_{\perp}$, $k_{\perp}$ were extracted and shown in Figure 4.12 along with the initial isotropic model. No differences are seen for k values so the film is not dichroic. At higher photon energies, differences in n are seen.

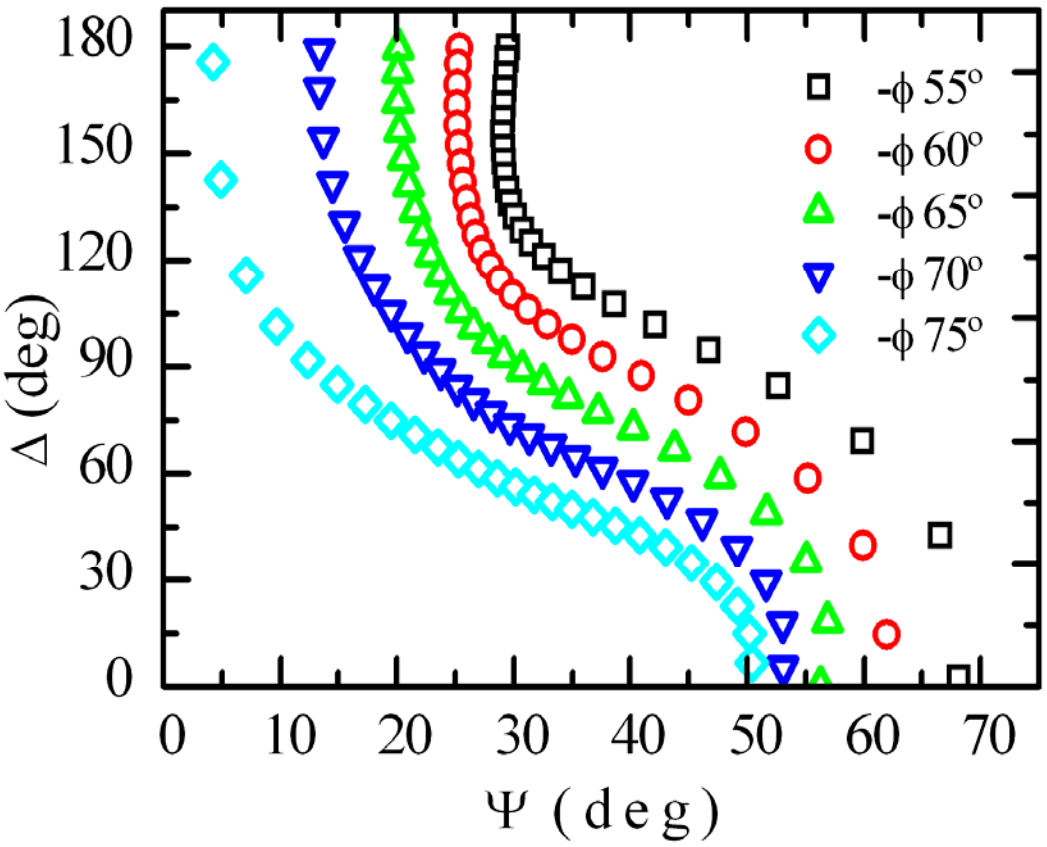

Figure 4.9. Simulated Δ-Ψ trajectories for various ϕ using an isotropic model of POMA film on Si. Simulated film thicknesses were from 0-150 nm in 4 nm intervals at a photon energy of 2.48 eV.

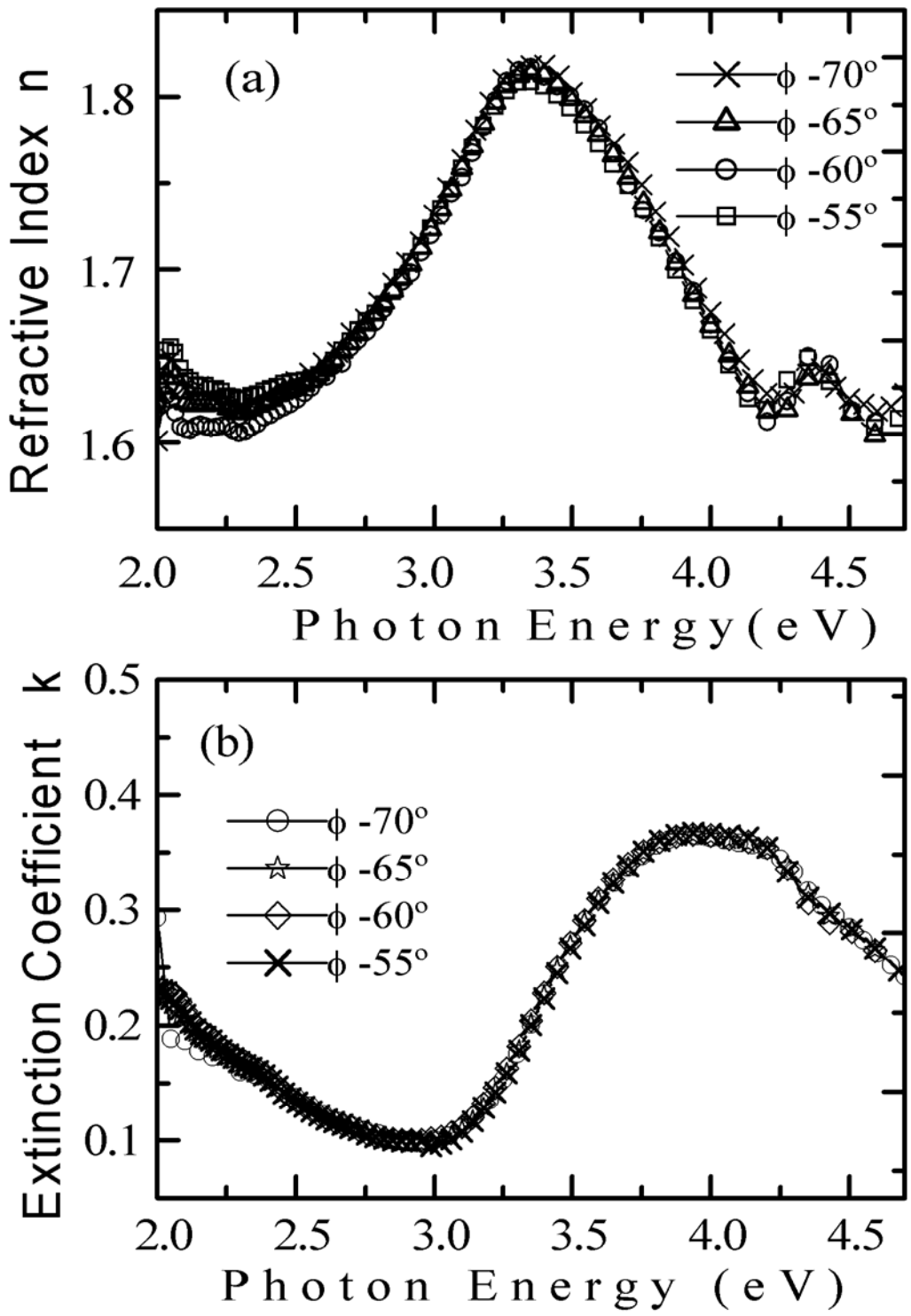

Figure 4.10. Optical constants (a) n and (b) k of POMA films at various incident angles (55 – 70°)

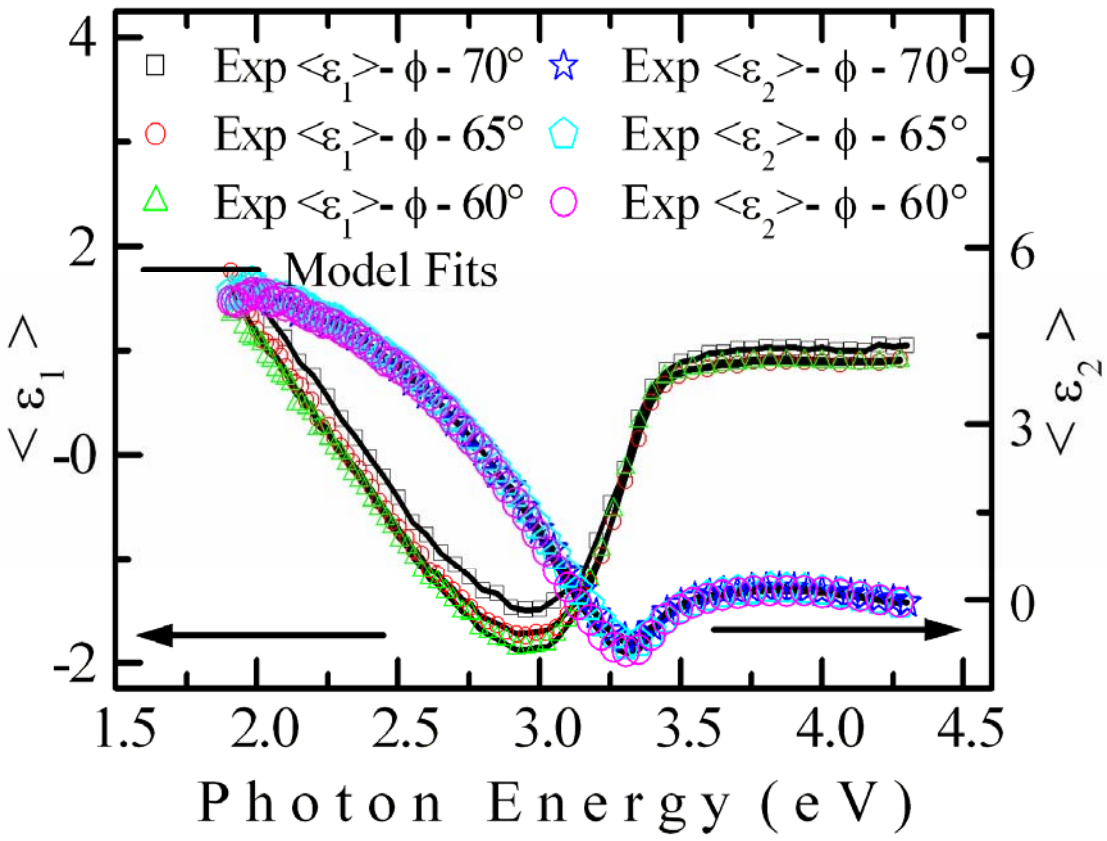

Figure 4.11. Experimental data and fits to the anisotropic model for POMA at various ϕ between 60°-70°.

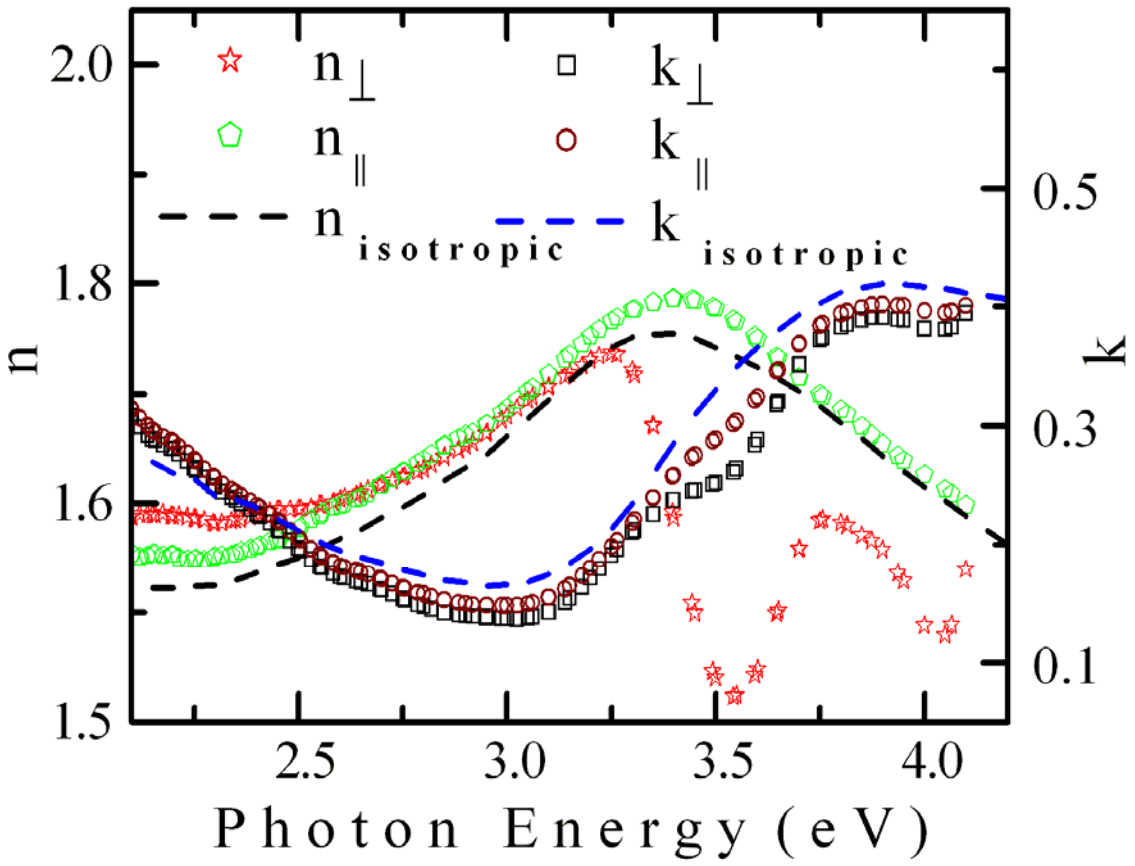

Figure 4.12. Extracted $n_{\parallel}$ $k_{\parallel}$ and $n_{\perp}$ $k_{\perp}$ of POMA along with isotropic model in dashed lines.

As typically observed for anisotropic polymer films, $n_{\|}$ is greater than $n_{\perp}$ at higher photon energies where the optical absorption is larger (Fig. 4.4). This observation can be rationalized by considering that when the polarized light is maximally absorbed, the π electrons oscillate more in the plane of the film leading to a larger $n_{\|}$. The oscillatory behavior of $n_{\perp}$ can be explained in that the dips in $n_{\perp}$ occur near absorption peaks (Fig. 4.4) indicating a weak but observable anomalous dispersion for $n_{\perp}$. Polynomial formulas that closely reproduce the optical constants obtained in this study are included in the Appendix.

An explanation for the lack of significant difference in n and k at lower energies and within 10° change in ϕ could be due to smaller molecular weight of the polymer used in this study. POMA used in this study was 21,000 g/mol. These shorter chains are less likely to be influenced by the forces exerted on them during spinning. In the literature, polymers exhibiting more prominent anisotropy were found to be 500,000 g/mol and higher.[13, 19]

Optical properties of PANI have been reported in the literature.[16] However the report shows variation in n and k with changes in thickness of the film as well as various preparation conditions. Therefore, direct comparison could not be made with present results other than to note the similarity in the general features of n and k across the spectrum.

4.3.4. Film Roughness

The film surface morphology was examined using AFM with typical images for POMA on SiO_2 and POMA on Si are shown in Figure 4.13a and b respectively. The roughness data was incorporated into our optical model as a Bruggeman effective medium

approximation (BEMA) layer. The BEMA layer is a mixture of the POMA layer with voids (n = 1 and k = 0) and is formulated as:

$$f_v \frac{\varepsilon_v - \varepsilon}{\varepsilon_v + 2\varepsilon} + f_c \frac{\varepsilon_{POMA} - \varepsilon}{\varepsilon_{POMA} + 2\varepsilon} = 0 \tag{4.6}$$

where fv + f_{POMA} = 1 and where f_v and f_{POMA} and ε_v and ε_{POMA} are the volume fractions and dielectric functions of void and POMA respectively. Also, ε is the composite effective dielectric function. Roughness layer thickness of 9.4 nm was obtained as an approximation by doubling the root mean squared (RMS) roughness (4.7 nm x 2) observed by AFM measurement as seen in Figure 4.13 b. This layer was added to the current model as a BEMA layer, which consists of 50 % voids and 50 % anisotropic POMA layer.

In Table 4.3, the anisotropic model along with BEMA used to fit the experimental data for POMA on Si is given. The result of this enhanced model further improved the MSE for 50 nm sample from 15 to 9 and for thicker films (120 nm) from 30-22. However the use of BEMA did not change the optical properties of POMA.

The complete model developed in our study was put to test on three separate samples which were prepared using same POMA solution and same spin speed. Overlapping spectra in Figure 4.14 for all three samples suggests similar morphology and optical properties for these samples.

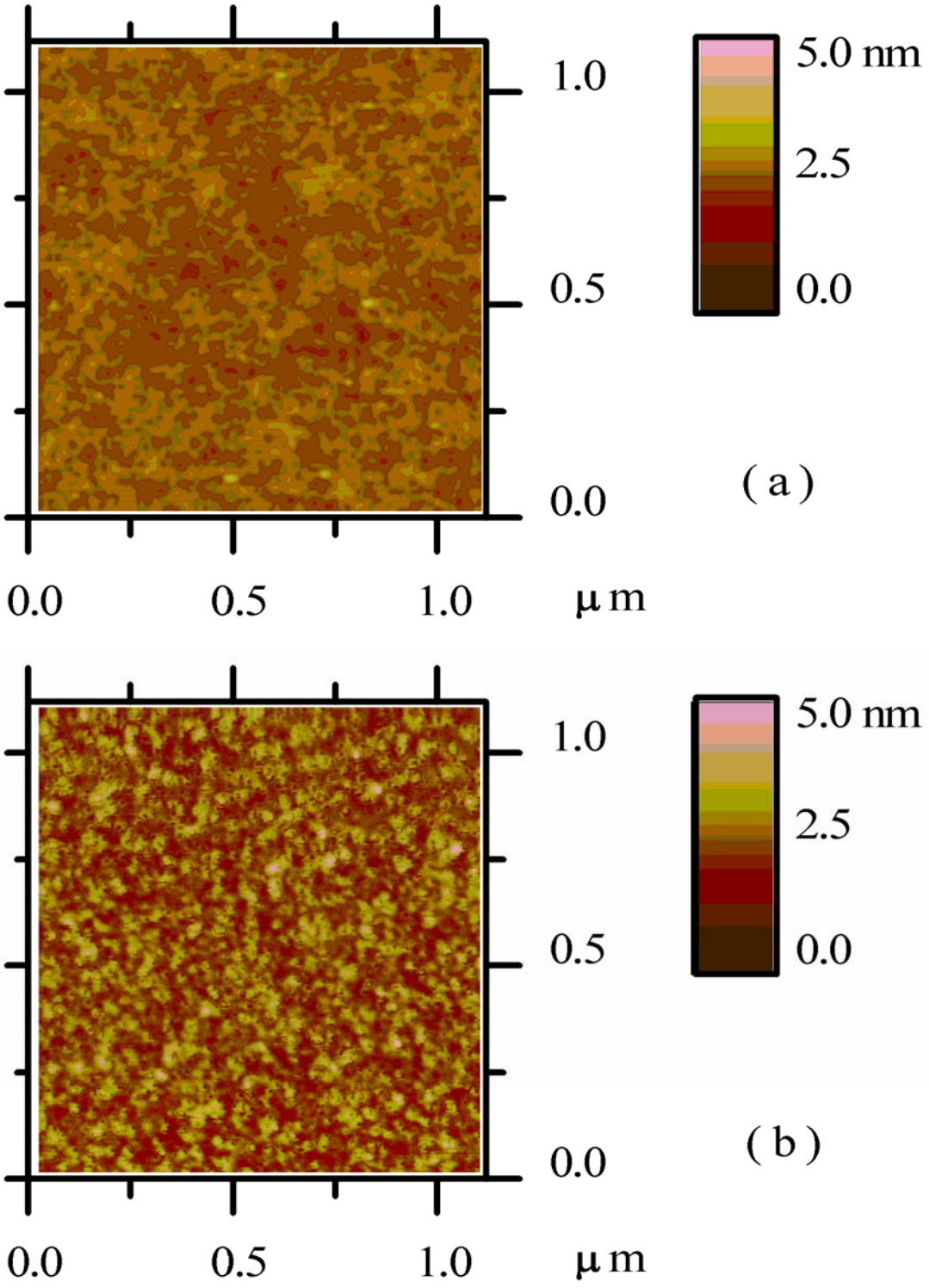

Figure 4.13. AFM images of POMA film on (a) native SiO_2 on Si substrate and (b) Si substrate. RMS roughness was 2.6 nm for POMA films on SiO_2 and 4.7 nm for POMA films on Si.

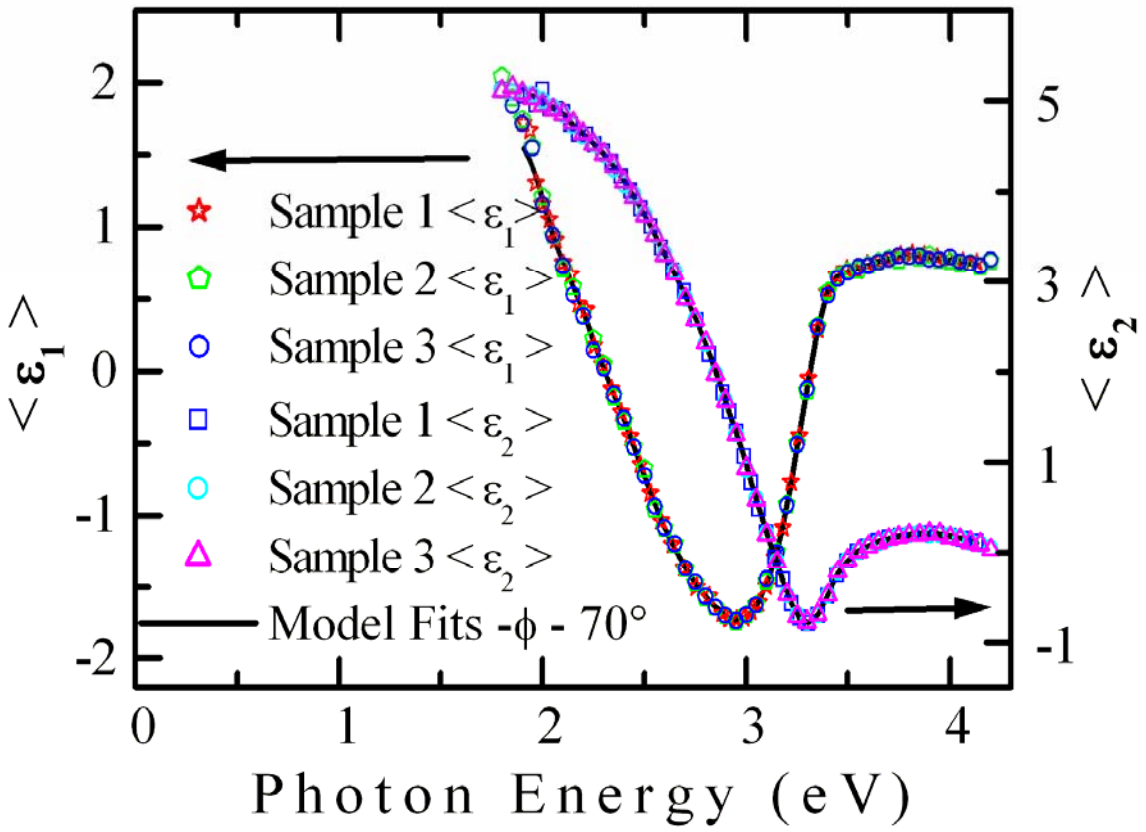

Figure 4.14. Spectra for 3 samples prepared in under similar conditions of concentration and spin speeds.

The complete model was also tested for POMA deposited onto SiO_2. It should be noted that the roughness of POMA films deposited on SiO_2 was smaller than that of films spin cast on Si 5.7 nm for (Si vs. 2.7 nm for SiO_2). Figure 4.15 shows the extracted pseudo dielectric constants of the sample (POMA on SiO_2 substrate), which are in excellent agreement with the model. MSE for the model fit was 12, which suggest a reasonable accuracy.

4.4. Conclusions

The optical properties modeling process and the optical properties (n and k) of thin POMA films are reported. Various complimentary techniques such as UV-Vis spectroscopy and AFM were used to improve the ellipsometric model and reduce the number of parameters that were needed to be fit. The Lorentz oscillator model was used to determine uniaxial anisotropic optical properties, and no in-plane anisotropy was observed. The parallel and perpendicular components ($n_{\|}, k_{\|}$) and ($n_{\perp}, k_{\perp}$) were obtained using this optical model. A BEMA was found to improve the fit of data to the model but did not change the optical properties obtained from the fit.

It is well known that film optical properties are dependent on the preparation conditions. In the present study we report the conditions that reproducibly yielded good films, and optical properties corresponding to the resulting films. The reported properties should serve as a guideline and in a future report we will detail how the optical properties can change with post deposition treatments.

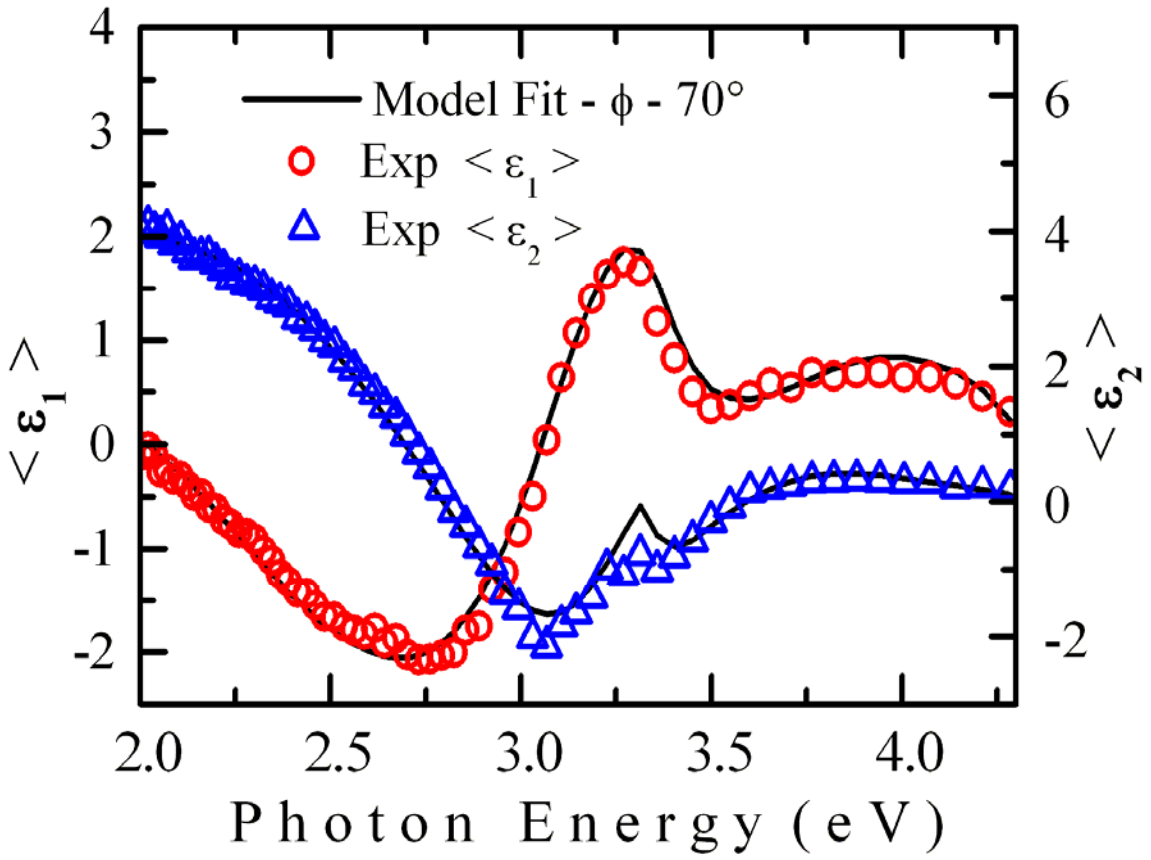

Figure 4.15. Experimental and fit data of POMA on SiO_2 using Lorentz oscillator and BEMA Models.

BEMA (50% void)	9.4nm
Uniaxial ($n_{\parallel}$, $k_{\parallel}$ & $n_{\perp}$, $k_{\perp}$)	46.0nm
POMA ($n_{\perp}$, $k_{\perp}$)	0nm
POMA ($n_{\parallel}$, $k_{\parallel}$)	0nm
Interfacial SiO_2	1.0nm
Si Substrate	1mm

Table 4.4. Model with roughness layer (Bruggeman effective medium approximation (BEMA))

4.5. Appendix

Formulas to reproduce the optical properties observed in n and k reported in Figure 4.11 and with x as the photon energy in eV in specific ranges

$n_{\parallel}$:

Photon Energy (2-4.3 eV)

$y = 0.0656\ x^6 - 0.951\ x^5 + 5.30\ x^4 - 13.9\ x^3 + 16.1\ x^2 - 3.19\ x - 3.51$

$k_{\parallel}$ and $k_{\perp}$:

Photon Energy (2-3 eV)

$y = 2.68\ x^6 - 41.5\ x^5 + 267\ x^4 – 913\ x^3 + 1750\ x^2 – 1780\ x + 751$

Photon Energy (3-4.3 eV)

$y = 26.8\ x^6 – 569\ x^5 + 5018\ x^4 – 23500\ x^3 + 62000\ x^2 – 86900\ x + 50600$

$n_{\perp}$:

Photon Energy (2-3 eV)

$y = 0.0913\ x^3 - 0.526\ x^2 + 0.985\ x + 1.05$

Photon Energy (3-3.6 eV)

$y = 112\ x^5 – 1800\ x^4 + 11500\ x^3 – 36700\ x^2 + 58500\ x – 37200$

Photon Energy (3.6-4.2 eV)

$y = 536\ x^6 – 12300\ x^5 + 118000\ x^4 – 599000\ x^3 + 2.00\ x10^6\ x^2 – 3.00\ x10^6\ x + 2.00\ x10^6$

4.6. References

1. Hwang, G. W.; Wu, K. Y.; Hua, M. Y.; Lee, H. T.; Chen, S. A., Structures and properties of the soluble polyanilines, N- alkylated emeraldine bases. *Synthetic Metals* **1998,** 92, (1), 39-46.

2. Mattoso, L. H. C.; Macdiarmid, A. G.; Epstein, A. J., Controlled Synthesis of High-Molecular-Weight Polyaniline and Poly(O-Methoxyaniline). *Synthetic Metals* **1994,** 68, (1), 1-11.

3. Monkman, A. P.; Adams, P., Stretch aligned polyaniline films. *Solid State Communications* **1991,** 78, (1), 29-31.

4. Losurdo, M.; Giangregorio, M. M.; Capezzuto, P.; Bruno, G.; Babudri, F.; Colangiuli, D.; Farinola, G. M.; Naso, F., Spectroscopic ellipsometry for characterization of organic semiconductor polymeric thin films. *Synthetic Metals* **2003**.

5. Kern, W.; Puotinen, D., *RCA Rev* **1970,** 31, 187.

6. Irene, E. A.; Goncalves, D., Fundamentals and applications of spectroscopic ellipsometry (vol 25, pg 794, 2002). *Quimica Nova* **2002,** 25, (6A), 1050-1050.

7. Tompkins, H. G., *A User's Guide to Ellipsometry*. Academic Press Ltd.: 1993.

8. Losurdo, M.; Bruno, G.; Irene, E. A., Anisotropy of optical properties of conjugated polymer thin films by spectroscopic ellipsometry. *Journal of Applied Physics* **2003,** 94, (8), 4923-4929.

9. Woollam, J. A., *Guide to Using Wvase32*. JAWoollam Co. Inc: Lincoln, 1999; p 12-45.

10. Fowkes, F., *Contact Angle Wettability and Adhesion*. American chemical Society: Washington DC, 1964; p 240.

11. Schubert, D. W., Spin coating as a method for polymer molecular weight determination. *Polymer Bulletin* **1997,** 38, (2), 177-184.

12. Silberbe, A., Adsorption of Flexible Macromolecules and Effect of Solvent-Solute Interactions Solute Concentration and Molecular Weight. *Journal of Chemical Physics* **1968,** 48, (7), 2835.

13. Zhou, J.; Monkman, A. P., Optically Anisotropic Films and Fibres from Conductive Polyaniline Solution. *Synthetic Metals* **2003,** 135-136, 373-374.

14. Pomfret, S. J.; Rebourt, E.; Monkman, A. P., Electroabsorption measurements of the emeraldine base form of polyaniline. *Synthetic Metals* **1996,** 76, (1-3), 19-22.

15. Losurdo, M.; Roca, F.; De Rosa, R.; Capezzuto, P.; Bruno, G., Spectroscopic ellipsometry study of interfaces and crystallization behavior during annealing of a-Si:H films. *Thin Solid Films* **2001,** 383, (1-2), 69-72.

16. Al-Attar, H. A.; Al-Alawina, Q. H.; Monkman, A. P., Spectroscopic ellipsometry of electrochemically prepared thin film polyaniline. *Thin Solid Films* **2003,** 429, (1-2), 286-294.

17. McCall, R. P.; Scherr, E. M.; Macdiarmid, A. G.; Epstein, A. J., Anisotropic Optical-Properties of an Oriented-Emeraldine-Base Polymer and an Emeraldine-Hydrochloride-Salt Polymer. *Physical Review B* **1994,** 50, (8), 5094-5100.

18. Sassella, A.; Tubino, R.; Borghesi, A.; Giardini, M. E.; Quadrelli, L., Spectroscopic ellipsometry measurements on an anisotropic organic crystal: potassium acid phtalate. *Thin Solid Films* **1998,** 313-314, 347-350.

19. Zhokhavets, U.; Gobsch, G.; Hoppe, H.; Sariciftci, N. S., Anisotropic optical properties of thin poly(3-octylthiophene)-films as a function of preparation conditions. *Synthetic Metals* **2004,** 143, (1), 113.

CHAPTER 5 – CHARACTERIZATION and OPTIMIZATION of a P-CHANNEL POLY(*O*-METHOXYANILINE) BASED THIN FILM TRANSISTORS

5.1. Overview

The introduction to POMA and organic thin film transistors (OTFT) has been outlined in Chapters 1 and 2. The inherent advantages of the organic devices are significantly lower cost of fabrication, the possibility for use with flexible or larger area substrates, and lightweight.

OTFT is an important device in organic electronics, and charge carrier mobility is a key parameter to gauge OTFT performance. At present, the main limitation for widespread application of OTFT technology is low charge carrier mobility. Recorded OTFT mobilities are often several orders of magnitude lower than that for single crystalline Si, Ge, and GaAs.[1-3] The charge mobilities as high as 10^3 cm^2 V^{-1} s^{-1} are observed for Si. On the other hand, the charge transport in OTFT's depends on the degree of ordering of the molecules and/or polymer chains in the solid state, the grain boundaries, and the density of defects that are present in the system. This the lack of proper lattice in amorphous organic films severely restricts the mobility in OTFT as a charges are not delocalized.[4, 5] In these systems, charge transport is reported to take place by "hopping" of charge carriers between localized potential

wells in the direction of the electric field.[6, 7] Lower mobility in the range of 10^{-5} to 10^{-1} cm^2 V^{-1} s^{-1} have been reported for OTFT at room temperature in the literature.[8]

In this chapter, the electronic properties of OTFT's based on POMA is reported. The increased solubility of POMA compared to its parent, PANI (Fig 5.1) facilitates doping process, as well as purification, and enables the polymer to be spin cast on to different substrates for fabrication of OTFT's. A variety of factors and preparation conditions affect the mobility of charge carriers and performance of OTFT. In this study, we have considered three gate dielectric layers with different dielectric constants for the OTFT's, and also considered post fabrication treatments such as annealing and doping to improve the mobility of the OTFT.

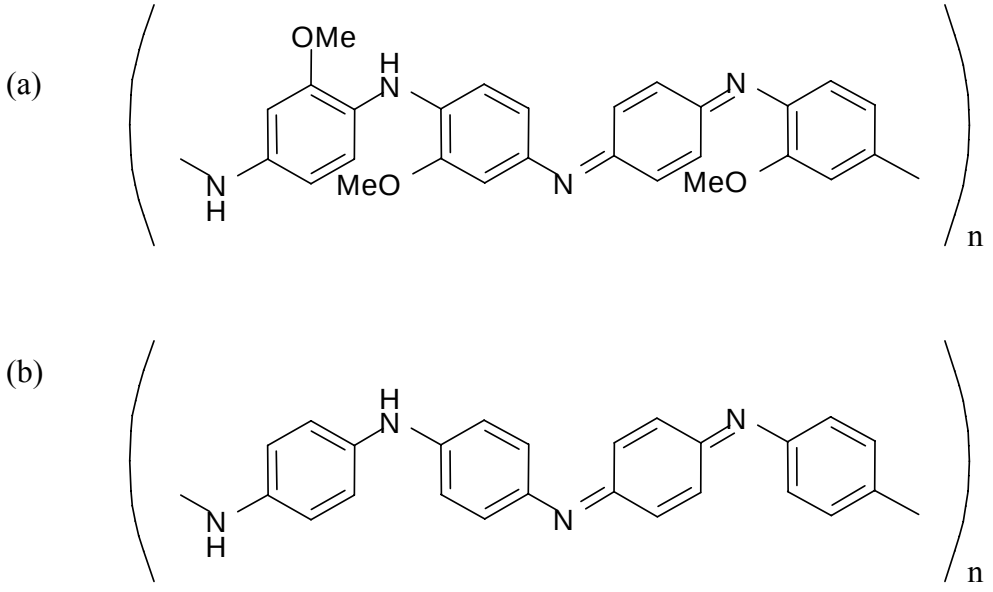

Figure 5.1. Molecular structure of (a) POMA and (b) PANI.

5.2. Experimental Procedures

Before film deposition, Si (single crystal, n-type, <100> orientation, resistivity < 0.02 Ωcm) wafers were cleaned using the RCA procedure.[9] A "sacrificial" oxide layer was grown before the Si wafer was cut to a desired size (~2 cm^2) using a diamond scribe. The cut wafers were dipped in 48 wt % HF, and rinsed in de-ionized water to remove SiO_2 or Si particles on the substrate surface resulting from the wafer cleaving process. Subsequently, the wafers were placed in an oxidation furnace to grow approximately 30 nm of SiO_2. In order to reduce any surface states on Si and SiO_2, the oxide was annealed in forming gas, which is 5 % H_2 gas in 95 % N_2 gas at 450 °C for 15 min.

Gold (Au) lines of various dimensions were deposited by thermal evaporation of gold from a point source through a custom designed shadow mask. The thickness of the lines (~ 200 nm) was determined using a quartz crystal monitor. The channel length was varied from 75 μm to 500 μm while most channel widths were kept constant at 5 mm. A design of this gold pattern is given in Figure 5.2.

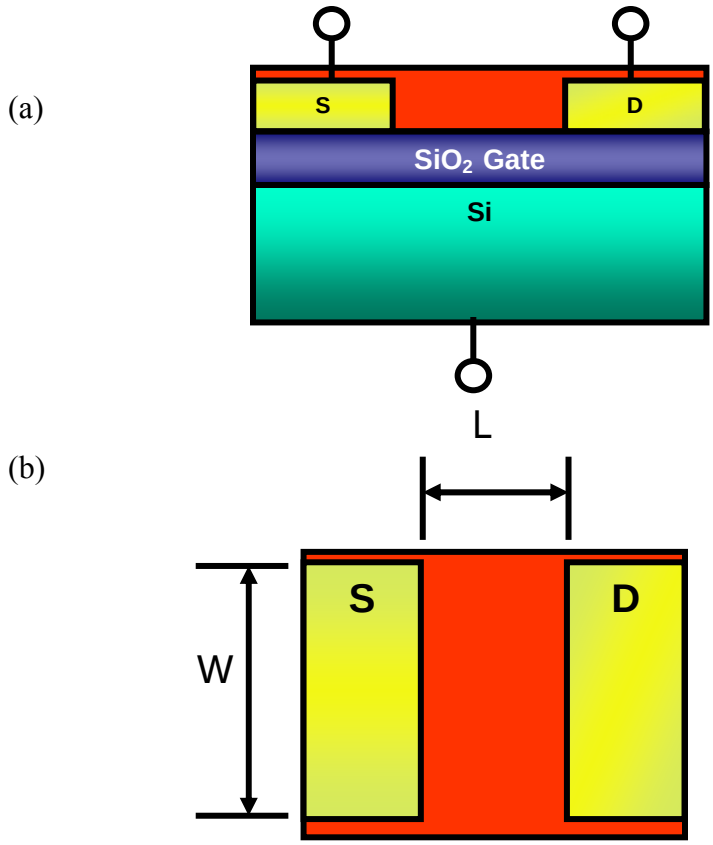

Figure 5.2. (a) cross section view of the OTFT and (b) top view of gold line patterns. L is the channel Length (5 mm) and W is the channel width 75 – 250 μm.

POMA used in this study was obtained commercially from Aldrich (molecular weight 120K Daltons). The POMA solution for spin coating was prepared by dissolving POMA in 50/50 (vol %) mixture of dichlromethane and chloroform also obtained commercially from Fisher and Aldrich respectively. The resulting dark blue solution was stirred for 2 hrs at room temperature and pressure in a closed container, and vacuum filtered using a 1μm filter disc.

The filtrate was stirred for another hour before spin coating the solution onto the gold patterned substrate at 3000 RPM. A micropipette was used to dispense 20 μL of POMA solution on to the spinning substrate surface at close proximity, and the substrate was allowed to spin for about 2 min in ambient N_2. In order to investigate the effects of annealing on electrical properties of POMA, some were annealed at temperatures ranging from 25 - 150 °C and a pressure of 10^{-6} torr.

In addition to SiO_2 (static dielectric constant K = 3.9) as the gate dielectric for the OTFT's, polyethylene (PE) was used as a low-K non polar dielectric layer (K = 2.3), and the copolymer of vinylidene fluoride with trifluoroethylene (PVDF-TrFE) was used as a more polar high-K dielectric organic layer (K = 7.5) on RCA cleaned Si substrates. Commercially available medium density PE (Aldrich) 2-5 wt % was dissolved in decahydronapthalene (Decalin) at ~ 70 °C and spin coated at 3500 rpm promptly in order to maintain the temperature and keep PE in solution. Likewise, PVDF-TrFE in molar ratio of 50/50, obtained from Atochem Inc, was spin coated from solutions of 0.3 - 4 wt% of the copolymer dissolved in methylethylketone (MEK). Experiments were carried out to ensure that PE and PVDF-TrFE did not dissolve in chloroform or dichloromethane and likewise POMA did not

dissolve in Decalin or MEK. The resulting PE and PVDF-TrFE films were annealed at 10^{-6} torr and 90 °C and 27° C respectively overnight to remove traces of solvents from the film matrix, and potentially allow the strained polymer strands to relax.

Gold lines were deposited on top of the dielectric films as mentioned earlier followed by POMA film deposition. The samples were stored in low humidity N_2 environment between experiments.

The optical properties of the films of POMA and PVDF-TrFE were characterized using custom built rotating analyzer spectroscopic ellipsometer, and have been reported.[10, 11] A detail description of Ellipsometry is given in Chapter 3. These optical properties were used in the ellipsometric model to non-destructively measure the film thicknesses.

PE and PVDF-TrFE thin films were ellipsometrically modeled using the Cauchy model as no apparent absorbance was observed during transmission UV-Vis spectroscopy of the film on quartz substrate. The Cauchy formula used is as follows: [12]

$$n(\lambda) = A + \frac{B}{\lambda^2} + \frac{C}{\lambda^3} \tag{5.1}$$

Where λ is the wavelength and A, B, and C are parameters that are fit in the analysis. The quality of the fit of the data to the model is assessed by the mean square error (MSE), whose value of 0 indicates a perfect correspondence of measured and model calculated results. Once a satisfactory fit was observed, the optical properties (refractive index) were extracted and are given in Figure 5.3a for PE and b for PVDF-TrFE.

The thermogravimetric analysis (TGA) of POMA in both film and powder forms were carried out using TA instruments high resolution thermo-gravimetric analyzer model

6220. A known weight (~20 mg) of POMA powder and POMA films were heated in an aluminum weigh pan from room temperature to 550 °C at the rate of 10 °C/min in a nitrogen environment with flow rate of 15 mL/min.

Once the temperature range of thermal stability of the POMA was determined, the annealing of POMA films was carried out in the vacuum chamber with *in-situ* ellipsometry capabilities shown in Figure 5.4. During annealing, the polymer films were exposed to various temperature settings and for various durations at 10^{-6} Torr. The ellipsometric measurements were carried out during the annealing process to obtain change in film thickness and optical properties of POMA films.

(a)

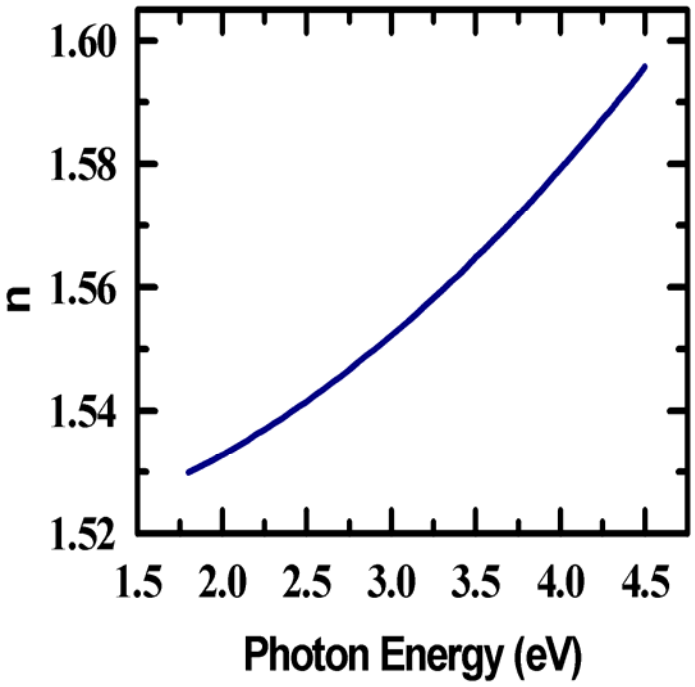

(b)

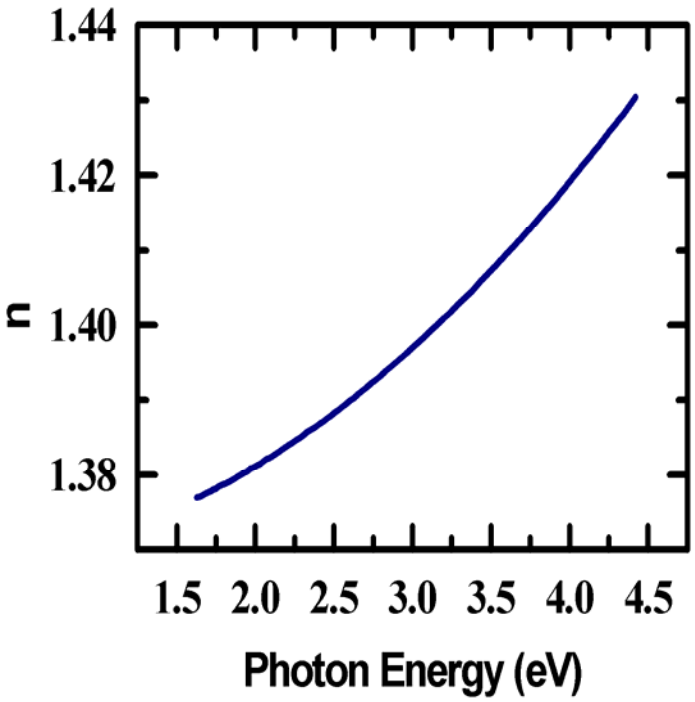

Figure 5.3. (a) Extracted optical properties of PE. k = 0 (b) extracted optical properties of PVDF-TrFE k=0.

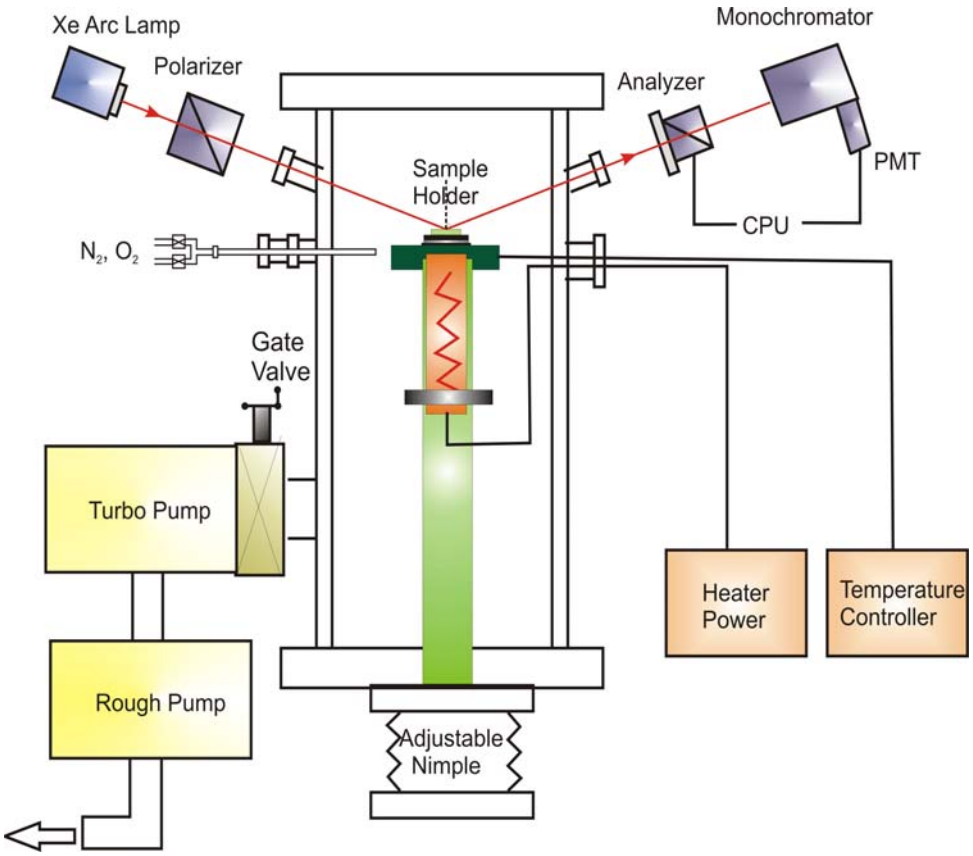

Figure 5.4. Custom built vacuum chamber with *in-situ* ellipsometer for annealing experiments.

The electronic measurements on OTFT were carried out using a Keithley 236 Source Measure Unit and an additional power supply was used to supply the gate voltage. The custom built dual probe station (probes from Signa Corporation) were connected to the source and drain electrodes. The vacuum chuck was used as the gate electrode. The reverse side of Si substrate was sanded with a diamond scriber to remove SiO_2 layer and Ga-In eutectic coating was applied to make an ohmic contact between the device and the gate electrode. With the source electrode grounded, the voltages reported here are source-drain voltage and source-gate voltages.

The current flowing between source (S) and drain (D), I_{SD} obtained from the I-V transfer characteristics plots was used for comparison of device performance. From the turn-on characteristics plot (I_{SD} vs. V_G where G is the gate) as shown in Figure 5.5b, field effect mobility was calculated using the following formula.

$$\mu = \frac{L}{WC_{die}V_{SD}}\left(\frac{\partial I_{SD}}{\partial V_G}\right) \tag{5.2}$$

where μ is the field effect mobility, W is the channel width, L is the channel Length (both measured in cm), $\frac{\partial I_{SD}}{\partial V_G}$ is the slope in the turn-on characteristic (I_{SD} vs V_G) curve, and C_{die} is gate dielectric capacitance per unit area (F/cm).

5.3. Results and Discussion

5.3.1. POMA OTFT with SiO_2 Dielectric Layer

The OTFT transfer characteristics of an OTFT showing the drain current (I_{SD}) versus drain voltage (V_{SD}) at different gate voltages (V_G) are given in Figure 5.5a and b. An increasing positive I_{SD} for increasing negative V_G and positive V_{SD} (Fig. 5.5a) indicates a P-Channel device. Likewise, a negative I_{SD} for negative V_{SD} and negative V_G (Fig. 5.6a) confirms the P-channel nature of the device operating in accumulation mode.

From the slope of the turn-on characteristics showing I_{SD} versus V_G at different V_{SD} shown in Figure 5.5b, the OTFT dimensions (Fig. 5.2) and thickness of the dielectric layer, the mobility of POMA OTFT is calculated using Equation 5.2. The mobility calculated for a typical POMA OTFT with SiO_2 gate dielectric was of the order of 10^{-3} $cm^2 V^{-1} s^{-1}$ which is the range reported in the literature. Mergulhao *et al.* have extracted a POMA mobility of $2x10^{-4}$ using time of flight experiments,[13] while Patil *et al.* have used cyclic voltametry and OTFT measurements to determine the mobility of POMA in 10^{-3} range.[14] The borderline between the de-localized process such as band-transport and a localized process such as hopping mechanism is usually taken at the mobility between 0.1- 1 $cm^2 V^{-1} s^{-1}$. Therefore a hopping mechanism is a more plausible method of charge transport in POMA OTFT's. With this mechanism of charge transport in consideration, several post fabrication treatments were carried out in order to optimize the mobility of the OTFT: Annealing the devices at moderate temperatures and vacuum to reduce trap density and levels, doping the POMA film with HCl to increase carrier density, and substituting the SiO_2 dielectric layer with organic films of

higher and lower K to reduce localization. The results of these investigations are reported below.

(a)

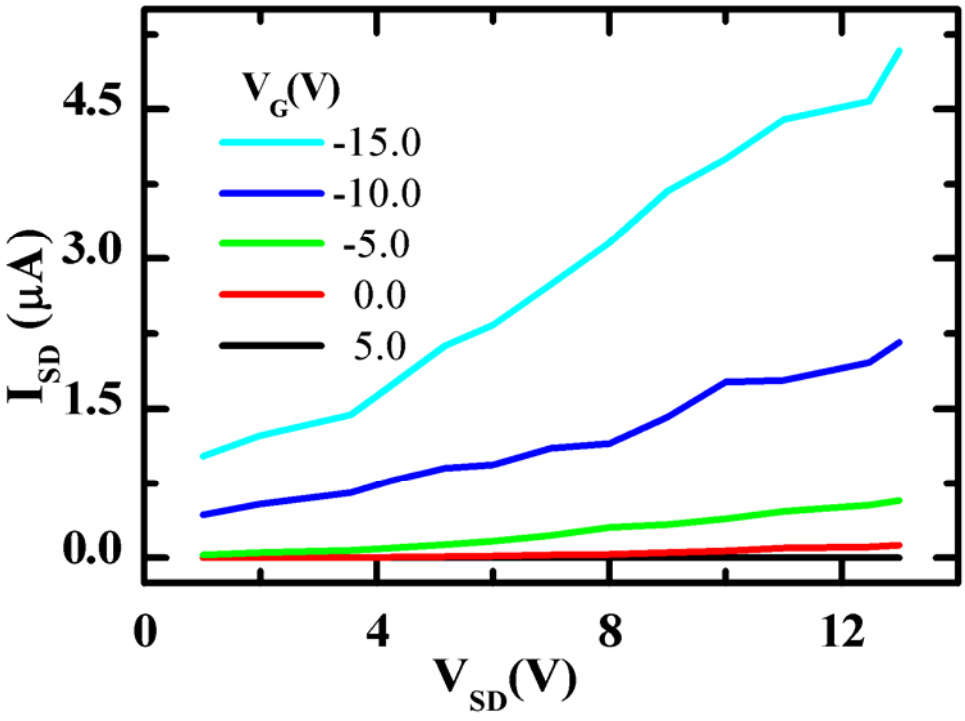

(b)

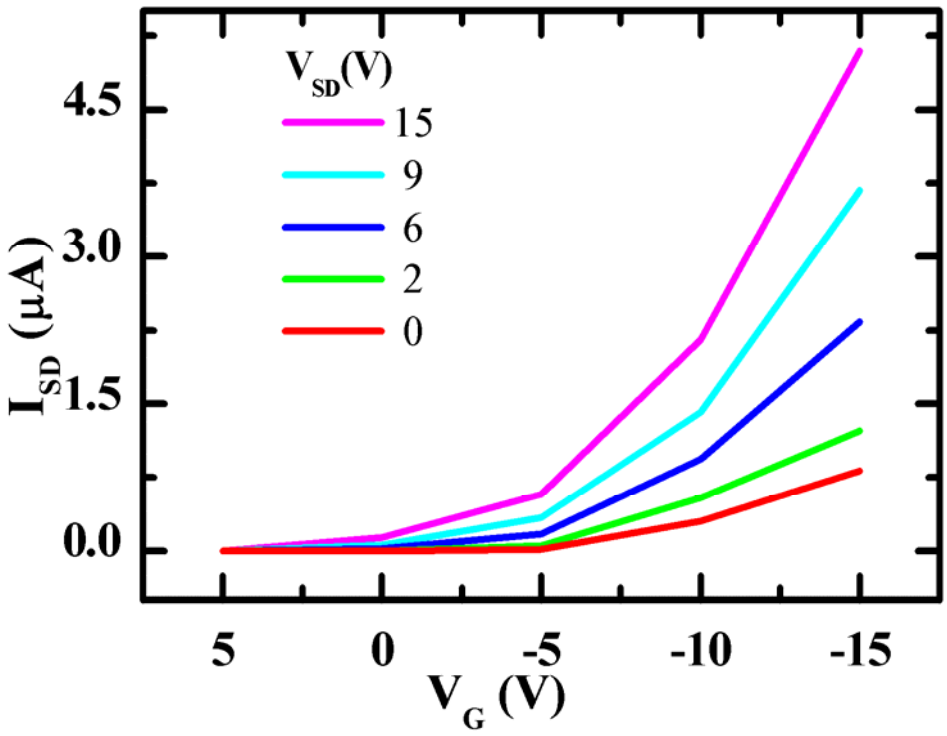

Figure 5.5. (a) The transfer characteristics of POMA OTFT and (b) Turn-on characteristic plot.

(a)

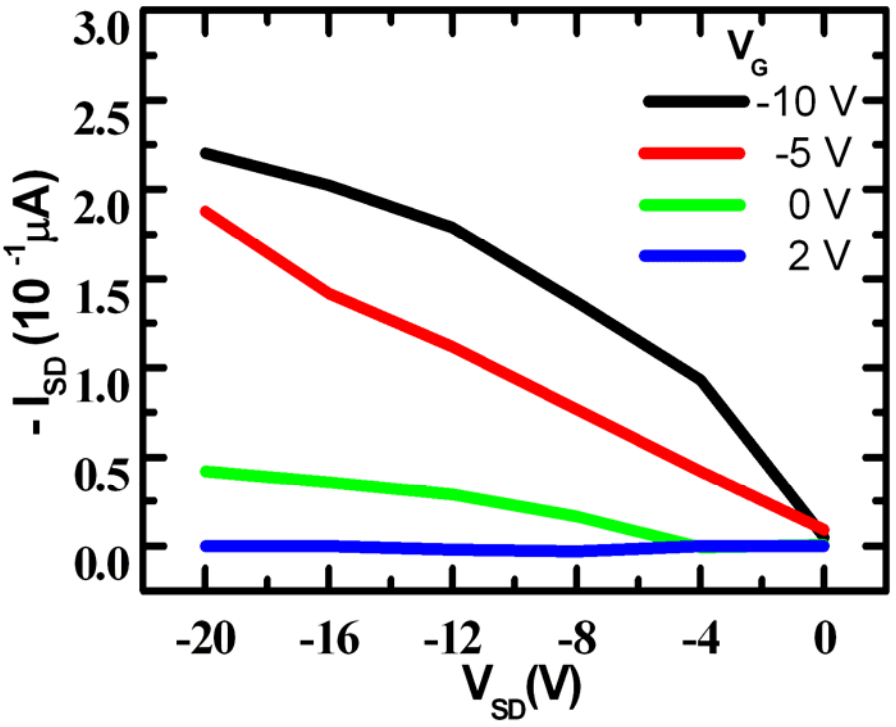

(b)

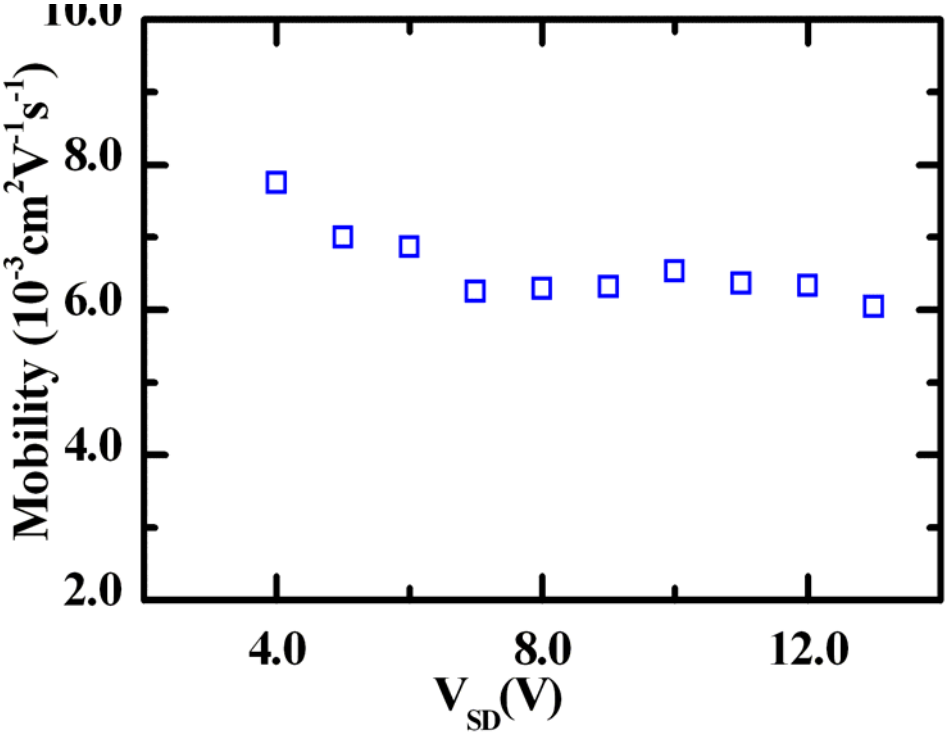

Figure 5.6. (a) The transfer characteristics of POMA OTFT in the negative V_{SD} range, and (b) the calculated mobility for POMA OTFT.

5.3.2. Effect of Thermal Annealing on Mobility

Thermal annealing at moderately high temperature and vacuum helps remove moisture, solvent, and other smaller molecules trapped in the film during the spin coating process, and also prevent oxidation of the film during the process. Moderate heating also provides energy for polymer strands to relax and reorganize to a thermodynamically stable state thus improving molecular alignment and ordering.[2] This process could reduce the density of trap sites and eliminate deep traps from the system resulting in improved mobility of the OTFT.

In order to investigate the thermal stability of the POMA film, TGA analysis was carried out by heating POMA powder and POMA films in the TGA analyzer under ambient N_2. A typical TGA thermograph of POMA obtained in our investigation is shown in Figure 5.7. The general features in the thermograph of the polymer film and the powder form were similar.

In Figure 5.7, an initial gradual weight loss of 10-20 % observed at 70 - 150 °C can be explained by the loss of moisture, solvents (chloroform, and dichloromethane), and smaller molecules present in the film. A sharper decline in weight is observed at temperatures above 150 °C indicating deterioration of the polymer chains. At these high temperatures, the HCl molecules from doped POMA films are also removed, but the weight loss is less significant as the dopant only occupies a small percentage of the bulk weight.[15] The HCl dopant is not affected during annealing at moderate temperatures (< 150 °C) which has been verified by mass spectrometry, chemical titration, and elemental analysis.[15, 16] Similar thermal behavior has been reported for PANI and some of its derivatives albeit at

slightly different temperatures.[17] This difference can be attributed to the difference is molecular structure and weight. The deterioration of POMA is severe in an oxygen containing environment where 50 % or greater weight loss was observed for POMA at 250 °C in air.

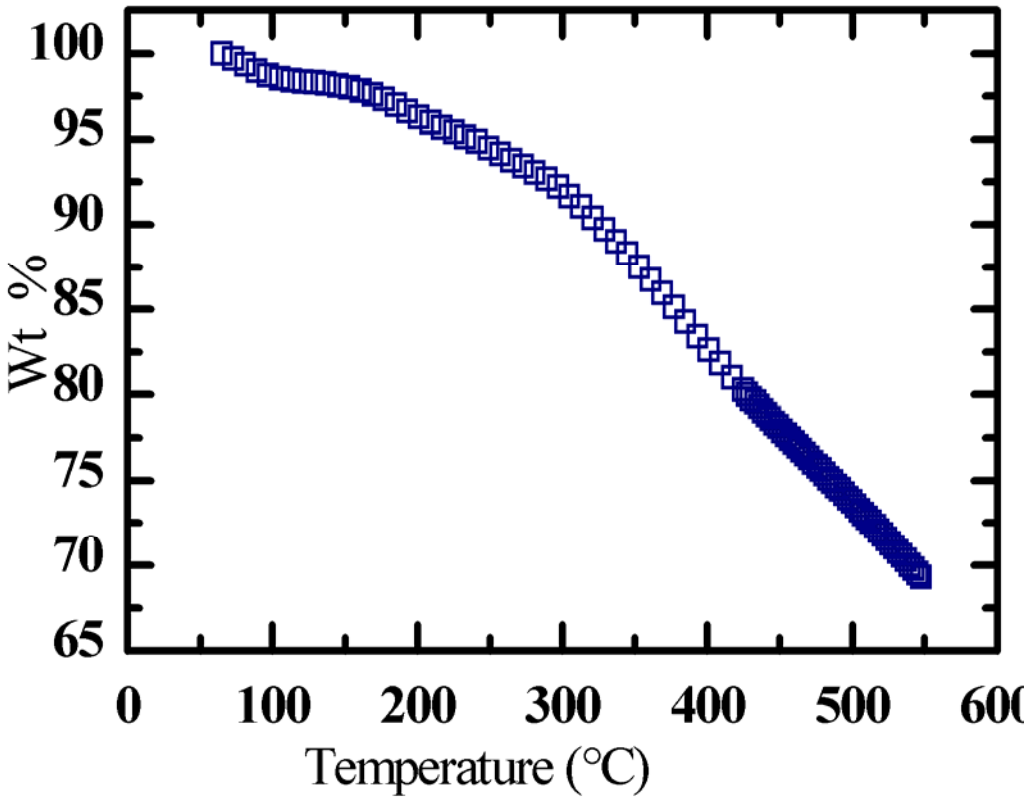

Figure 5.7. TGA thermograph of POMA film in N_2 environment and the temperature range of 70-550 °C obtained at 10 °C/min increment.

These results reveal good thermal stability for POMA films below 150 °C where the subsequent annealing experiments were carried out. The vacuum chamber with *in-situ* rotating analyzer ellipsometer (Fig. 5.4) as described in Chapter 3 was used to observe a gradual change in optical properties and film thickness of POMA on native SiO_2 substrates. Figure 5.8a shows the decreasing film thickness of POMA at various annealing temperature settings. During spin coating of POMA film, shearing forces can disentangle the polymer chains and orient them in patterns that may not be the most efficient for charge transport.[18] These twisting in the π-bonded phenyl rings is decreased when the film is annealed at temperatures around 100 °C. The consequent alignment of the polymers into a favorable thermodynamic equilibrium results in reduced thickness.[19] This decrease in thickness is accompanied by the increase in n and k of POMA as shown in Figure 5.8b, which confirms densification of the POMA films during annealing at moderate temperatures.

(a)

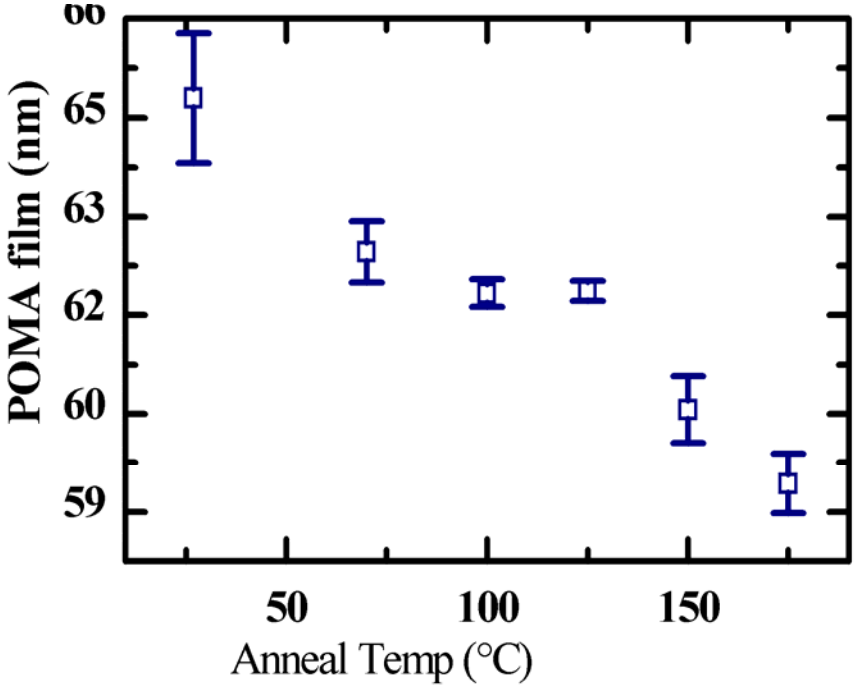

(b)

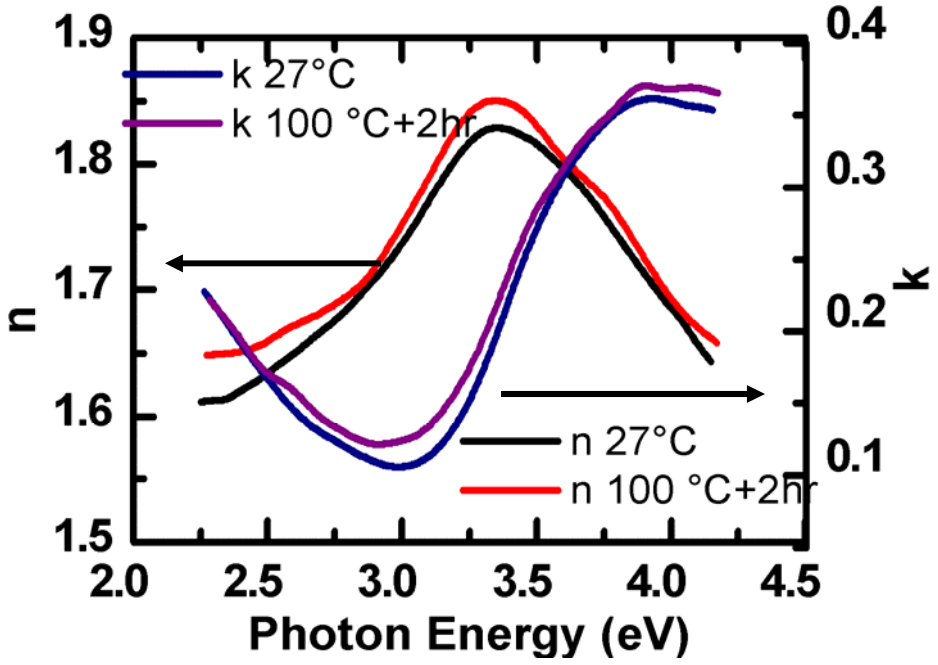

Figure 5.8. (a) Densification of POMA film during the initial stages of annealing process is accompanied by increase in n and k (b). At high temperatures >150 °C, POMA film deteriorates to amorphous carbon (a).

The mobility of annealed POMA OTFT measured at room temperature relative to the unannealed mobility is shown in Figure 5.9. A general improvement in field effect mobility is observed for short annealing times after which the mobility decreases depending on annealing temperature and time.

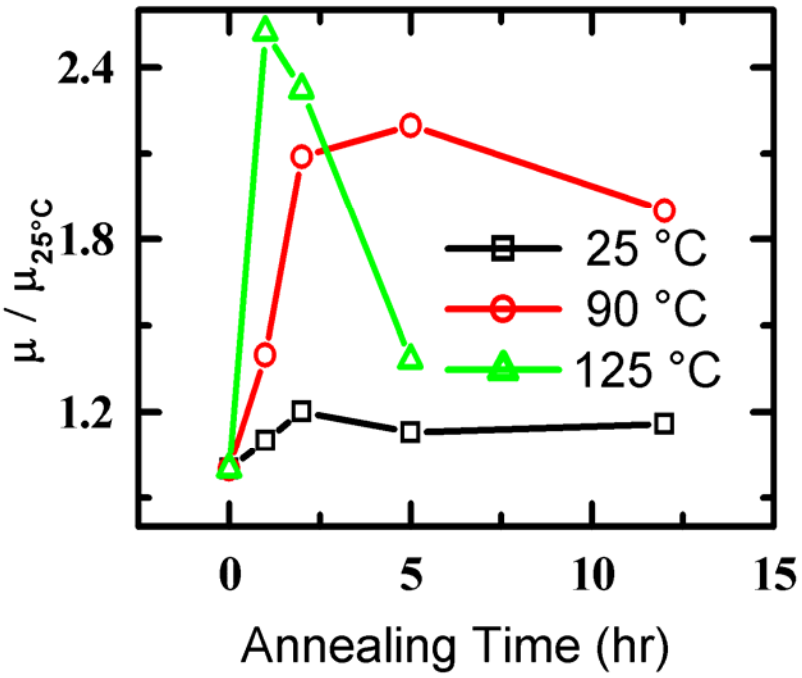

Figure 5.9. Annealing effect on normalized mobility of POMA OTFT

In Figure 5.9, the normalized mobility of the OTFT annealed in vacuum at room temperature does not change significantly regardless of annealing times (up to 12 hrs). When POMA is annealed at 90 °C, a two fold increase in normalized mobility is observed roughly after around 2 hours of annealing. Annealing at moderate temperature regularizes the amorphous polymer, and densification has already been evidenced from ellipsometric analysis of POMA films earlier (Fig. 5.8).

The improvement in mobility after annealing is consistent with improvements expected from a hopping mechanism of charge transport in POMA. The deep trapping sites are reduced and both deep and shallow traps sites are brought closer together by densification. Elemental analysis has been reported to show no change in chemical composition for PANI films during annealing at moderate temperatures, nor was doping concentration altered during annealing.[20] Therefore this moderate annealing procedure can also be used for doped film as well. In addition, the formation of "crystallites" or metallic islands of up to a few microns in size during annealing of organic polymers which improves charge mobility have also been reported by Dodabalapur *et al.*[21] Similar improvements in mobility has been reported from X-ray diffraction experiments carried out for PANI.[20]

Morphological improvement and decreased roughness during annealing have been observed from the ellipsometry for POMA films. The Bruggeman effective medium approximation (BEMA) layer incorporated into the ellipsometric optical model shown in Figure 5.8 decreased during optical modeling suggesting smoothening of the POMA film.[22] The BEMA layer is a mixture of the POMA layer with voids (n = 1 and k = 0) and is formulated as:

$$f_v \frac{\varepsilon_v - \varepsilon}{\varepsilon_v + 2\varepsilon} + f_c \frac{\varepsilon_{POMA} - \varepsilon}{\varepsilon_{POMA} + 2\varepsilon} = 0 \quad (5.3)$$

where fv + f_{POMA} = 1 and where f_v and f_{POMA} and ε_v and ε_{POMA} are the volume fractions and dielectric functions of void and POMA respectively. Also, ε is the composite effective dielectric function.

The annealing process, especially high temperature annealing is not all good news however. The improved alignment of POMA polymers during the initial stages of annealing which improves the inter-chain hopping parameters is seen to reverse and is even detrimental to the field effect mobility at higher annealing temperatures. Annealing POMA films at temperatures higher than 120 °C shows a decline in electrical mobility (Fig. 5.9). The elevated temperature is believed to cause the disordering of the polymer backbone network and also stimulate the de-doping process.[20] In addition to decomposition of the polymer, chemical modifications considered fatal to electrical properties, like substitution, cross-linking, and destruction of the apparent crystalline islands are also likely at high temperatures.[23]

5.3.3. Effect of Doping on Mobility

The charge transport in conjugated polymers, here POMA, is strongly dopant dependent as seen in Figure 5.10. When POMA film coated substrate was immersed in aqueous hydrochloric acid solution (0.2 M HCl) for various durations up to 20 min, a

significant increase in I_{SD} was observed and the mobility calculated likewise was an order of magnitude higher. Table 5.1 summarizes the improvement in mobility in POMA.

This increase in current can be attributed to the increase in the carrier concentration by controlled doping, and the increase in mobility seen can be explained well in the hopping mechanism of charge transport. HCl protonates the lone pair in nitrogen atom in the polymer to form $POMAH^+$ Cl-. Feng *et al.* have reported the polymer chains straightening from any coiled state by dopant interaction, which also reduces the π-defects created by ring twisting.[19] The dopants can also fill up the trapping sites at the interface,[24] and this shortening of hopping distance between the increased number of hopping centers can facilitate inter-chain transfer of charge carriers.[25]

Several drawbacks regarding the use of inorganic dopants have been documented. Kim *et al.* have reported HCl dopant loss by evaporation from polymer matrix at temperatures higher than 150 °C was greater than organic dopants (such as M-cresol) which have higher molecular weight.[23] In addition, the high surface tension of aqueous solution can have detrimental effects on the device structures, and prolonged exposure of OTFT to HCl solution (> 2 hr) results in partial dissolution of gold electrode which causes a short in the OTFT rendering them useless. To address these concerns, the annealing process was confined to temperatures below 125 °C. The milder temperature assured the stability of inorganic dopant in the POMA matrix. Furthermore, no structural damage was observed using optical microscopy when the OTFT emersion was limited to 0.2 M HCl for up to 20 mins to minimize gold dissolution.

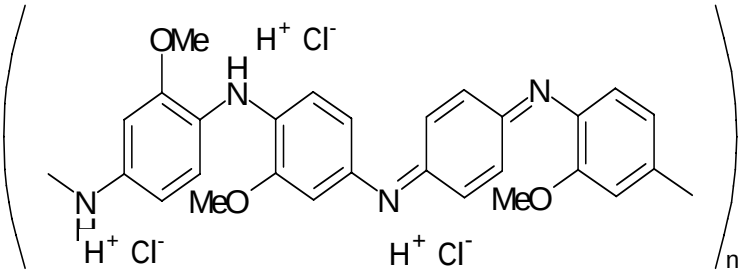

Figure 5.10. HCl protonating the lone pair of Nitrogen atom in POMA.

	Undoped	**3 min/ 0.2 M HCl**	**15 min/ 0.2 M HCl**	**2 hr**
Mobility (10^{-3} cm^2 V^{-1} s^{-1})	1.8	3.3	9.5	n/a

Table 5.1. Improvement in mobility is observed in POMA when doped with HCl for various durations. Prolonged exposure causes dissolution of Au and shorting of the OTFT.

5.3.4. Effect of Gate Dielectric Layer on Mobility

The two dielectric candidates chosen for potential replacements for SiO_2 in OTFT's have dielectric constant, K on both sides of SiO_2 (K = 3.9) used in OTFT thus far. Medium density polyethylene (PE) with K = 2.3 was a low-K, non-polar candidate, and a copolymer of vinylidene fluoride with trifluoroethylene (PVDF-TrFE), a polar organic copolymer with K = 7.5, was a high-K candidate for the OTFT fabrication. The transfer and turn-on characteristics for OTFT's fabricated with alternate dielectrics are given in Figures 5.11a and b and 5.12a and b.

The Mobility in the OTFT with PE layer was 10^{-2}, which was significantly better than the mobility observed in OTFT with either SiO_2 or PVDF-TrFE dielectrics, which were in the 10^{-3} and 10^{-5} $cm^2 V^{-1} s^{-1}$ ranges respectively. These results are summarized in Table 5.2 and are in agreement with the findings of Veres *et al.* who have also reported improvement in charge carrier mobility when a non-polar, low-K gate insulator (K < 3) was used instead of SiO_2.

(a)

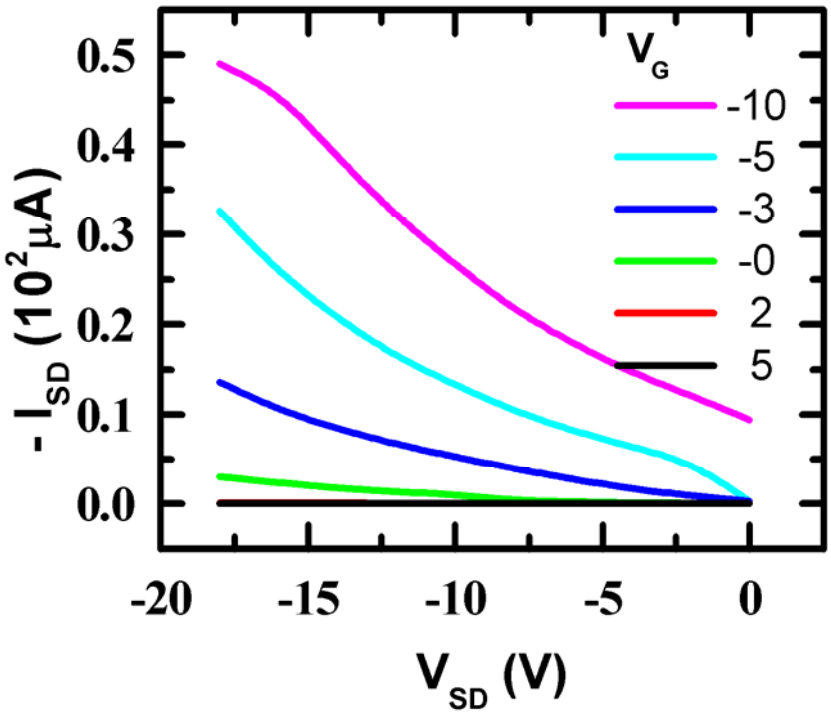

(b)

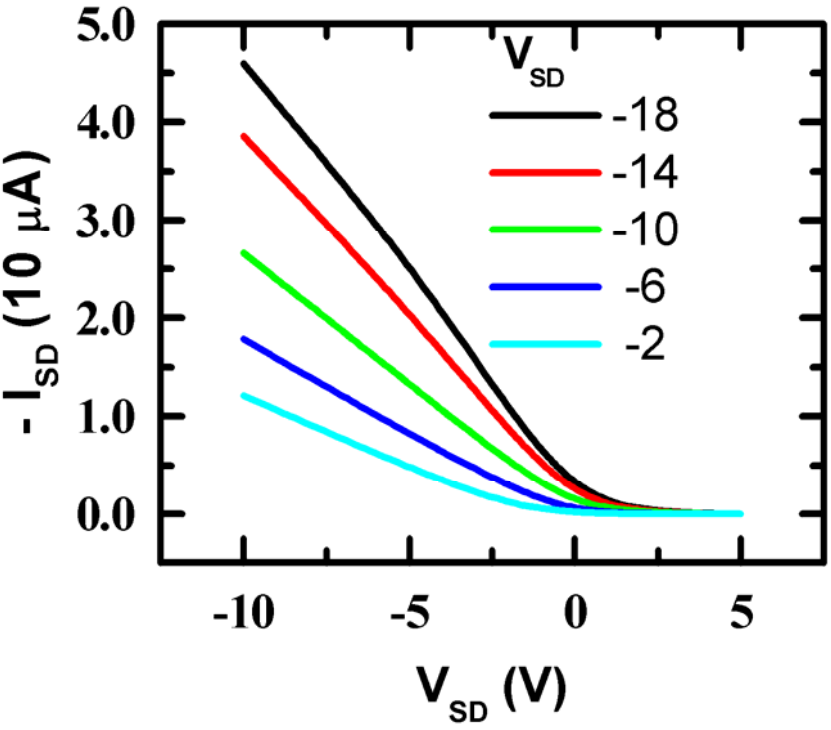

Figure 5.11. (a) transfer and (b) turn on characteristics plot of OTFT with PE dielectric layer.

(a)

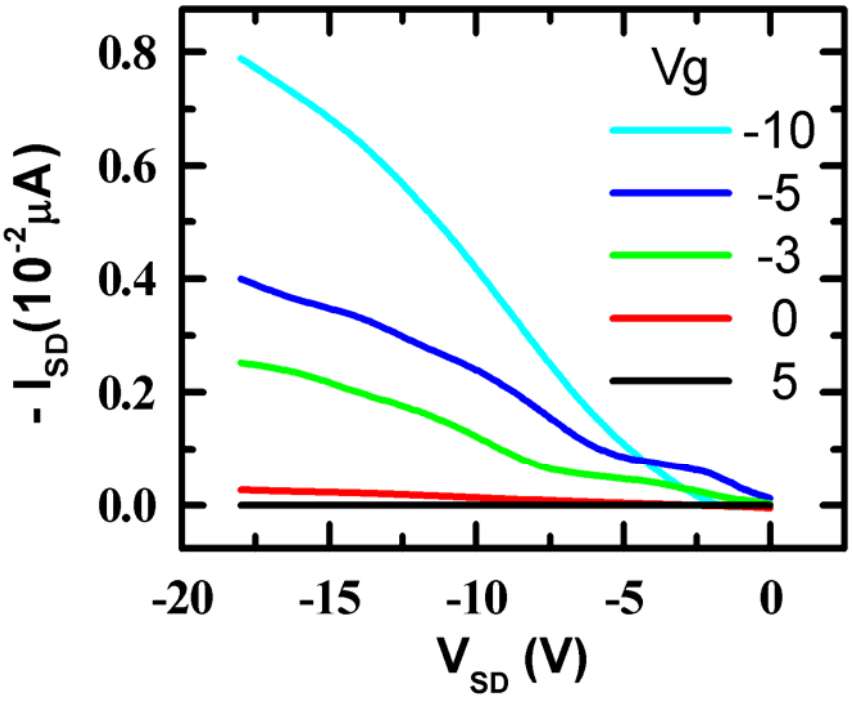

(b)

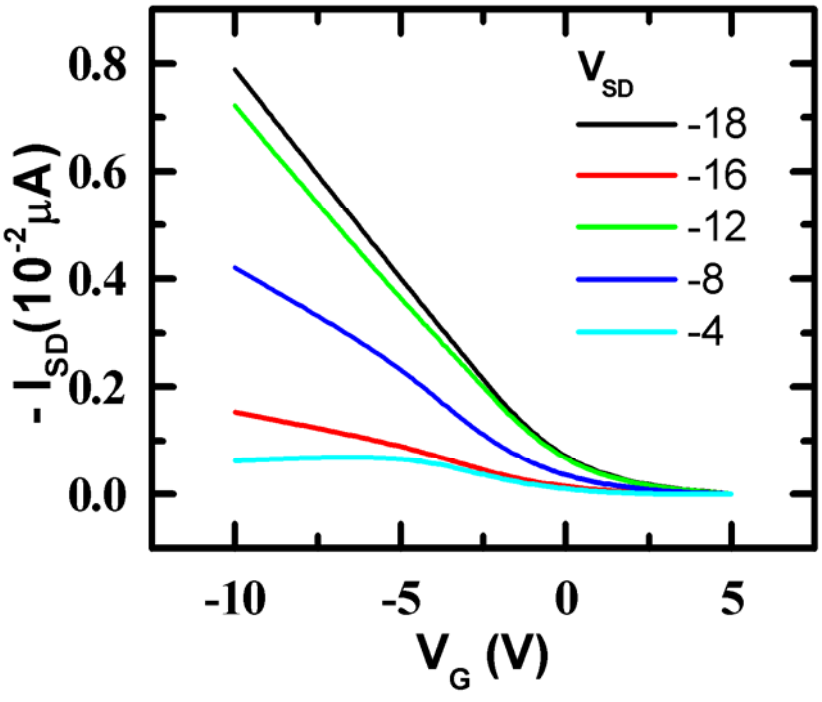

Figure 5.12 (a) transfer and (b) turn on characteristics plot of OTFT with PVDF-TrFE dielectric layer.

Dielectric layer	PE	SiO_2	P(VDF-TrFE)
k	2.3	3.9	7.5
Mobility ($cm^2 V^{-1} s^{-1}$)	$1x10^{-2}$	$5x10^{-3}$	$7x10^{-5}$

Table 5.2. Summary of the mobility of POMA OTFT with PE, SiO_2 and PVDF-TrFE dielectric layers.

During this investigation, PE films were spin-cast on substrates using a 0.5% solution in Decalin. These PE films were smooth and insoluble in subsequent processing solvents such as dichloromethane and chloroform, which allowed a good interface formation and little possibility of intermixing with POMA layer. The integrity and morphology of the films was thus maintained during subsequent film processing. Like PE, PVDF-TrFE also forms uniform film on Si substrate with rms roughness less that 1.3 nm for films under consideration (~ 80 nm).[11] These PVDF-TrFE films were spin-cast from a 1 % solution in methyl ethyl ketone (MEK) and the film thus formed was also insoluble in subsequent processing.

The gate material which capacitively couples the active layer and the contact metal electrodes play a vital role in the performance of OTFT. A dependable gate material should have low defect densities, a smooth surface with very little roughness and form sharp interfaces that facilitates good morphology of the subsequent active layer deposition. Initially, SiO_2 served as an excellent gate material for the inorganic devices with its ease of formation and sharp interface. Unfortunately the SiO_2 based device does not take advantage of one of the main reasons for interest in organic materials, which is the possibility of building electronic devices on flexible plastic substrates. Furthermore, the polar silanol

functional group (Si-OH) present in SiO_2 layer form trapping sites and affect the distribution of local electronic states thus reducing the mobility in OTFT with SiO_2 dielectric layer.[26]

When exploring an organic substitute for SiO_2 gate dielectric, high capacitance dielectric is normally desirable, as it reduces the operating voltage required to turn the device on.[8] PVDF-TrFE with K value of 7.5 was chosen for this reason. It has been reported that the polarity of the dielectric interface can affect the local morphology of the POMA film and the distribution of electronic states in it.[26, 27] The hopping sites in organic semiconductors can be considered localized in an amorphous solid. Therefore, the local variation in dipole orientation due to polar high-K dielectric layer can cause energetic disorder and create localized sites making charge transport difficult as demonstrated in Figure 5.13.[28] This presence of increased trapping sites at the interface has been investigated by many workers, who have reported higher temperature activation requirement for charges to hop between the trap sites when polar high-K dielectric layers were used.[27, 29, 30] Even though PE dielectric layer has a lower K, the decrease in gate capacitance from low-K dielectric is offset by the increase in mobility.

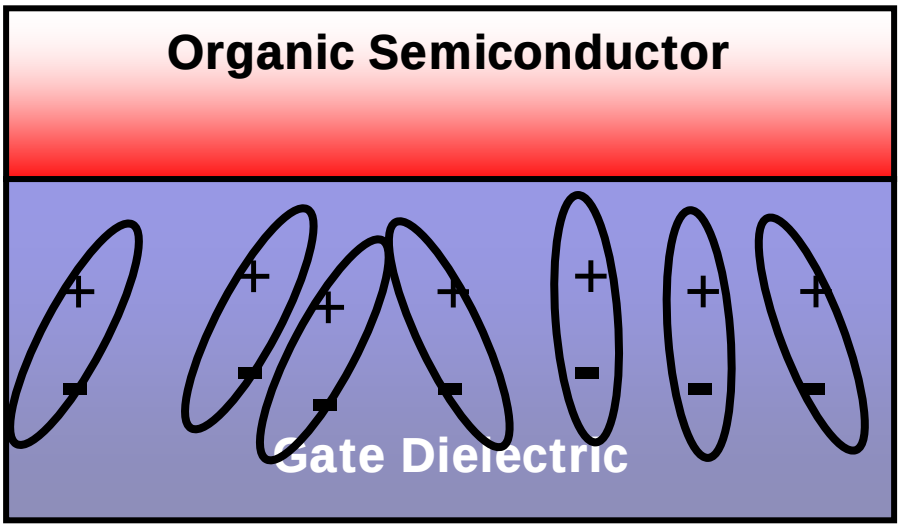

Figure 5.13. Local variation in dipole orientation in polar high-K dielectric creates localization sites in the adjacent semiconductor layer.

It must be noted that not all low-K insulators (with K = 2.1-2.3) provide the advantages seen in PE and few other insulating materials. Some porous low-K insulating materials containing hydroxyl, acrylate, or ester functional groups are found to be not as effective.[27] The use of non-polar layer in general also increases hydrophobicity of the surface and reduces wetting. While dramatic effects were not observed, when spin coating POMA film on top of PE, a careful balance in between low-K and wetting properties in dielectric films is recommended.

5.4. Conclusions

Step Taken	Procedure	Improvement compared to pre-treatment or SiO_2 gate.
Doping	In 0.2 M HCl for 2-20 min	8-10
Annealing	At 90°C and 10^{-6} Torr	2
PE buffer layer	Native SiO_2-PE -POMA	7-10
PVDF-TrFE layer	Native SiO_2 -PVDF-TrFE -POMA	0.02

Table 5.3. Summary of change in mobility of POMA after various treatments.

The change in mobility of POMA OTFT after various post fabrication treatments or substitution of dielectric layers is summarized in Table 5.3. POMA OTFT's were prepared using different gate dielectrics, SiO_2, PE, and PVDF-TrFE each having a different static dielectric constant, K = 3.9, 2.3, and 7.5, respectively. The dominant carrier transport was via holes in all cases resulting in P-Channel OTFT's. Annealing studies revealed rapid destruction of POMA above 150 ^{o}C and annealing at lower temperatures increased the film density and improved the mobility by two folds. Doping with HCl also improved the mobility. The combination of annealing and doping results strongly suggest a hopping mechanism for conduction in POMA. Low dielectric constant non-polar dielectrics also improved the POMA OTFT mobility by a half order of magnitude.

Detailed studies of morphology effects on mobility, the interface between the gold electrode contacts and POMA, charge injection into the semiconductor from the electrodes are essential in gaining a more complete understanding of OTFT performance and should be the subjects for future studies.

5.5. References

1. Taur, Y., *Fundamentals of modern VLSI devices*. Cambridge University Press: Cambrige, UK, 1998.

2. Horowitz, G., Organic field-effect transistors. *Advanced Materials* **1998,** 10, (5), 365-377.

3. Sirringhaus, H., Device physics of Solution-processed organic field-effect transistors. *Advanced Materials* **2005,** 17, (20), 2411-2425.

4. Schon, J. H., High mobilities in organic semiconductors: basic science and technology. *Synthetic Metals* **2001,** 122, (1), 157-160.

5. Garnier, F., Specificity and limits of organic-based electronic devices. In *Photonic And Optoelectronic Polymers*, 1997; Vol. 672, pp 420-436.

6. Vissenberg, M.; Matters, M., Theory of the field-effect mobility in amorphous organic transistors. *Physical Review B* **1998,** 57, (20), 12964-12967.

7. Comber, P. G. L.; Spear, W. E., Electronic Transport in Amorphous Silicon Films. *Physical Review Letters* **1970,** 25, (8), 509.

8. Dimitrakopoulos, C. D.; Malenfant, P. R. L., Organic thin film transistors for large area electronics. *Advanced Materials* **2002,** 14, (2), 99-+.

9. Kern, W.; Puotinen, D., *RCA Rev* **1970,** 31, 187.

10. Shrestha, R. P.; Yang, D.; Irene, E. A., Ellipsometry Study of Poly(o-methoxyaniline) Thin Films. *Thin Solid Films* **2005,** In Press, Corrected Proof.

11. Li, Y. X.; Yan, L.; Shrestha, R. P.; Yang, D.; Ounaiesc, Z.; Irene, E. A., A Study of the Optical and Electronic Properties of Poly (Vinylidene Fluoride-Trifluoroethylene) Copolymer Thin Films. *Thin Solid Films* **2005,** In Press.

12. Tompkins, H. G., *A User's Guide to Ellipsometry*. Academic Press Ltd.: 1993.

13. Mergulhao, S.; Faria, R. M.; Ferreira, G. F. L.; Sworakowski, J., Transport of holes in uniformly and non-uniformly protonated poly(o-methoxyaniline). *Chemical Physics Letters* **1997,** 269, (5-6), 489-493.

14. Patil, R.; Jiang, X.; Harima, Y., Mobilities of charge carriers in poly(o-methylaniline) and poly (o-methoxyaniline). *Electrochimica Acta* **2004,** 49, (26), 4687-4690.

15. Wang, Y. D.; Rubner, M. F., Stability Studies Of The Electrical-Conductivity Of Various Poly(3-Alkylthiophenes). *Synthetic Metals* **1990,** 39, (2), 153-175.

16. Wei, Y.; Hsueh, K. F., Thermal-Analysis Of Chemically Synthesized Polyaniline And Effects Of Thermal Aging On Conductivity. *Journal Of Polymer Science Part A-Polymer Chemistry* **1989,** 27, (13), 4351-4363.

17. Rodrigues, P. C.; de Souza, G. P.; Da Motta Neto, J. D.; Akcelrud, L., Thermal treatment and dynamic mechanical thermal properties of polyaniline. *Polymer* **2002,** 43, (20), 5493.

18. Monkman, P.; Aminabhavi, T. M., *Introduction to Macromolecular Science*. Wiley: New York, 2002.

19. Feng, J.; MacDiarmid, A. G.; Epstein, A. J., Conformation of polyaniline: Effect of mechanical shaking and spin casting. *Synthetic Metals* **1997,** 84, (1-3), 131.

20. Kobayashi, A.; Ishikawa, H.; Amano, K.; Satoh, M.; Hasegawa, E., Electrical-Conductivity Of Annealed Polyaniline. *Journal Of Applied Physics* **1993,** 74, (1), 296-299.

21. Dodabalapur, A.; Katz, H. E.; Torsi, L.; Haddon, R. C., Organic Heterostructure Field-Effect Transistors. *Science* **1995,** 269, (5230), 1560-1562.

22. Woollam, J. A., *Guide to Using Wvase32*. JAWoollam Co. Inc: Lincoln, 1999; p 12-45.

23. Kim, S.; Chung, I. J., Annealing effect on the electrochemical property of polyaniline complexed with various acids. *Synthetic Metals* **1998,** 97, (2), 127-133.

24. Kuo, C. T.; Weng, S. Z.; Huang, R. L., Field-effect transistor with polyaniline and poly(2-alkylaniline) thin film as semiconductor. *Synthetic Metals* **1997,** 88, (2), 101-107.

25. Paterno, L. G.; Mattoso, L. H. C., Influence of different dopants on the adsorption, morphology, and properties of self-assembled films of poly(o-ethoxyaniline). *Journal of Applied Polymer Science* **2002,** 83, (6), 1309-1316.

26. Chua, L. L.; Zaumseil, J.; Chang, J. F.; Ou, E. C. W.; Ho, P. K. H.; Sirringhaus, H.; Friend, R. H., General observation of n-type field-effect behaviour in organic semiconductors. *Nature* **2005,** 434, (7030), 194-199.

27. J. Veres; Ogier, S. D.; Leeming, S. W.; Cupertino, D. C.; Khaffaf, S. M., Low-<I>k</I> Insulators as the Choice of Dielectrics in Organic Field-Effect Transistors. *Advanced Functional Materials* **2003,** 13, (3), 199-204.

28. Veres, J.; Ogier, S.; Lloyd, G.; de Leeuw, D., Gate insulators in organic field-effect transistors. *Chemistry Of Materials* **2004,** 16, (23), 4543-4555.

29. Dionisio, M.; Fernandes, A. C.; Mano, J. F.; Correia, N. T.; Sousa, R. C., Relaxation studies in PEO/PMMA blends. *Macromolecules* **2000,** 33, (3), 1002-1011.

30. Granholm, P.; Paloheimo, J.; Stubb, H., Charge transport in thin films of polyaniline: Variable-range hopping in a parabolic quasi-gap. *Physica Status Solidi B-Basic Research* **1998,** 205, (1), 315-318.

CHAPTER 6 - SUMMARY and FUTURE DIRECTIONS

1.1. Summary of Results

In this study, the optical and electronic properties of an organic polymer, Poly(o-methoxyaniline) were characterized and its use to fabricate an OTFT have been investigated. A custom ellipsometer was assembled and software was written in LabVIEW™ to automate the data collection process. Likewise, a custom probe station was assembled for electronic properties measurement.

Chapter 2 describes the mechanism of charge transport in organic semiconductors. The organic semiconductors can be small monomeric molecules such as pentacene and anthracene, or large macromolecules such as polyacetylene or poly(o-methoxyanline). The concepts of resonance and conjugation in delocalization of charge and charge transport were emphasized. The resonance effect results in more stable molecules and is exemplified by comparing the hydrogenation of cyclohexene and benzene to form cyclohexane. With exceptions to few organic semiconductors such as pentacene at low temperatures, the band-like transport of charges which results in high mobility is rarely seen in amorphous organic semiconductors. More likely mechanisms of charge transport are the hopping and multiple

trapping and release. A generic transfer and turn-on characteristic plots obtained during the electrical measurement of an OTFT was presented where the slope of the turn-on characteristics was used to calculate the field effect mobility of OTFT.

In terms of OTFT architecture, two popular configurations the top contact and the bottom contact configurations were considered. The bottom contact design was convenient to fabricate and also demonstrated higher levels of current between the source and the drain (I_{SD}) as this design minimized the distance traveled by the charge carriers between the S and D. A simple design and construction of a custom probe station and software automation for data collection was also presented.

In Chapter 3, the ellipsometric technique was discussed along with the fabrication of a custom vacuum chamber with *in-situ* rotating angle ellipsometer. The data collection for the ellipsometer was computer interfaced and automated using LabVIEW™ software.

Utilizing the ellipsometer built as described in Chapter 3, the optical properties of POMA films on Si and SiO_2 substrates were investigated in Chapter 4. An optical model of POMA was developed that was necessary interpret the ellipsometric measurements in terms of film optical properties and thickness. Furthermore, the optical properties also helped gain preliminary insight into the electronic properties of POMA. In addition to the ellipsometer, various complimentary techniques such as UV-Vis spectroscopy and AFM were used to improve the ellipsometric model and reduce correlation between the parameters being varied during the regression analysis.

Starting from a simple assumption of a Cauchy model, the optical model was developed in complexity to a Lorentz oscillator model to incorporate the absorption peaks

observed in the UV-Vis spectra. Further improvements were made in the optical model by understanding the uniaxial anisotropic properties of POMA. While no in-plane anisotropy was observed a small out of plane anisotropy was visible. ($n_{\|}$, $k_{\|}$) and ($n_{\perp}$, $k_{\perp}$) were obtained using this optical model. The roughness information obtained from AFM was incorporated into a BEMA model which improved the fit of data to the model.

With an understanding of the optical properties, POMA OTFT's were prepared using different gate dielectrics—SiO_2, PE, and PVDF-TrFE—each having a different static dielectric constant—K = 3.9, 2.3, and 7.5 respectively. It was found that the dominant carrier transport was via holes, which resulted in P-Channel OTFT's. Annealing studies revealed rapid destruction of POMA above 150 ^{o}C and annealing at lower temperatures increased the film density and improved the mobility by a half order on magnitude. Doping with HCl also improved the mobility. The combination of annealing and doping results strongly suggest a hopping mechanism for conduction in POMA. Low dielectric constant non-polar dielectrics also improved the POMA OTFT mobility by a half order of magnitude. These findings are described in Chapter 5.

1.2. Future Directions

OTFT has shown promise in the filed of electronics where light weight, large area and flexible electronics are desirable. In this study, a gradual shift from SiO_2 dielectric to an organic dielectric has been made and Si was primarily used as a substrate. In future work, POMA films can be cast into flexible plastic substrates to produce all organic OTFT.

The optical properties of the spin cast films on POMA showed slight variation with the change in preparation condition and the underlying substrate. Therefore, a detailed study on optical properties is required when changing preparation conditions as well as the substrates.

Annealing leads to densification of the polymer film as indicated by the increase in refractive index. Therefore, optical anisotropy investigation should be carried out to see definitive evidence of preferred molecular alignment.

Detailed study in the effect of morphology of the dielectric and the semiconductor layer on mobility needs further scrutiny. The interface between the gold electrode contacts and POMA, charge injection into the semiconductor from the electrodes are essential in gaining a better understanding of OTFT performance. These details along with study in OTFT fabricated with piezoelectric and ferroelectric PVDF-TrFE dielectric layer will be the future steps of this study.

The initial results from the use of PVDF-TrFE as a gate dielectric were discouraging. However, there are a few ways to circumvent this problem. One possible way would be use PVDF-TrFE as a gate dielectric with an additional non-polar buffer layer such as PE between the gate and the dielectric. Veres *et al.* have found some success in improving the device performance by inserting a non-polar buffer layer between a polar dielectric and the POMA film.[1]

References

1. Veres, J.; Ogier, S.; Lloyd, G.; de Leeuw, D., Gate insulators in organic field-effect transistors. *Chemistry Of Materials* **2004,** 16, (23), 4543-4555.